THERMODYNAMIC APPROACH TO COMPUTATIONAL MODELING OF CHEMICALLY

STABILIZED SOILS

A Dissertation

by

PAVAN AKULA

Texas A&M University

DOCTOR OF PHILOSOPHY

Chair of Committee,   Dallas N. Little
Committee Members,   Paul Schwab
                     Anand J. Puppala
                     Robert L. Lytton
                     Charles Aubeny
Head of Department,   Robin Autenrieth

May   2020

Major Subject: Civil Engineering

ABSTRACT

Civil engineers have extensively used chemical stabilizers to change the physical, chemical and engineering properties of clayey soils for infrastructure development. Various types of chemical stabilizers have been developed to treat clayey soils. Depending on the chemical composition of the stabilizer, they are divided into two categories (1) Non-calcium based stabilizers such as hydrogen ion stabilizer (HIS) (2) Calcium based stabilizers such as lime, cement, fly ash, etc. The application of thermodynamic models to simulate the reaction between the stabilizer and soil minerals can help to understand the stabilization mechanism. In addition, the models can predict the formation of reaction products including deleterious products such as ettringite. This dissertation proposes the application of thermodynamic models to simulate the stabilization reaction between the soil minerals and the chemical stabilizer.

The dissertation is divided into three parts that investigates application of thermodynamic models for chemically stabilized soils. The first part shows the application of two thermodynamic equilibrium models (Visual MINTEQ and Geochemist's Workbench) to simulate the reaction between the shrink-swell prone clay mineral smectite and HIS. In addition, the model predicted partial dissolution of smectite and release of Al^{3+} ions from the octahedral layer. The modeling results helped to establish a stabilization mechanism, which is described as a reduction in the shrink-swell potential by adsorption of Al^{3+} ions on the surface of smectite. X-Ray diffraction (XRD), Fourier-transform infrared spectroscopy (FTIR) and cyclic swell tests were used to validate the results.

The second part presents a case study where fluidized bed ash (calcium based stabilizer) was used to stabilize a subgrade soil causing structural distress due to excessive ettringite formation. Thermodynamic modeling code GEMS-PSI was used to evaluate the occurrence of ettringite and, more specifically, to quantify the extent of ettringite formation. The model is shown to be 91% reliable in its ability to predict ettringite (qualitatively). The quantitative evaluations of the mass percentage of ettringite formation are shown to have a mean error of 12.4% with a standard deviation (SD) of 12.8%. The results from thermodynamic model were calibrated to account for the

assumptions that reduced the mean error to 0.12% (SD 4.3%).

The third part investigates the application of thermodynamic models to predict ettringite synthesized from Ca-Al-SO_4 suspensions. The objective of the study was to predict ettringite without calibration. This was achieved using material characterization methods such as XRD, differential thermogravimetric analysis (DTA), and scanning electron microscopy. Five suspensions with different stoichiometric ratios of $Ca(OH_2)$ to $Al_2(SO_4)_3 \cdot 18\,H_2O$ were used to thermodynamically and experimentally evaluate ettringite formation. Qualitatively, the model predicted ettringite as a stable phase for 3 out of 5 samples, which was also experimentally verified. Quantitatively, the models mean prediction error was close to 4%. The results indicate the application of thermodynamic model to predict ettringite formation.

DEDICATION

To all those who strive for the betterment of humanity through science and engineering.

ACKNOWLEDGMENTS

I will forever be thankful to my PhD advisor, Professor Dallas Little for supporting me during all these years. He is the funniest and one of the smartest people I know. I hope that I can one day be as smart as him. Another committee member that I would like to thank is Professor Paul Schwab. He was always available in times of need and provided valuable feedback. I am very grateful to Professor James Mitchell for all the insightful discussions and advise. I am also indebted to Prof. Puppala for his mentorship. I also have to thank my PhD committee member Professors Robert Lytton, and Charles Aubeny for their career advice and suggestions.

A good support system is essential in surviving graduate school. I was lucky to have my current and past lab members Narain Hariharan, Javier Grajales Saavedra, Atish Nadkarni, Lorena Garcia, and Jun Zhang who helped me to come up with new research ideas. I also have to thank my colleagues Pravin Saraswatula, Poura Arabali, and Fawaz Kaseer. As an international student, being away from home was really tough. I am forever indebted to Ms. Barbara Hein for treating me like family and spoiling me with all her delicious cakes. I appreciate the continuous support from Ms. Laura Byrd.

I thank my badminton friends Aswin, Vivek, Arun, Bhaskar, Dharish, Gary, Niley, and Joyce for keeping me sane. I am really thankful to my roommates Dhanvi, Rajeev, Sayak, Naveen, Abhijith, Vignesh, and Ashok for being a good friend and helping me in times of need.

I especially thank my parents and my in-laws for having faith in me, being supportive and reminding me to have fun. I thank my pet Oreo who has been a very good listener and critique of my ideas. Words of appreciation are not enough to thank my wife Sandhya Saisubramanian, who always motivates me and brings out the best in me. The last few years have not been easy for both of us. Thank you for sticking with me, even when I was being irritable. I believe that this has strengthened our relationship.

TABLE OF CONTENTS

Page

LIST OF FIGURES

xi

LIST OF TABLES

1. INTRODUCTION

1.1 Background

The soundness of the underlying soil determines the long term performance of any infrastructure. More often than not, infrastructure development is being carried out on challenging soil conditions. The mineralogy and physicochemical behavior of these soils makes it challenging to use conventional methods to solve this problem. Presence of certain expansive clay minerals such as smectite pose a significant threat to the durability of any structure. In the presence of moisture, smectite swells up to 300% of its initial volume [1]. During dry seasons, smectite shrinks by releasing moisture. This shrink-swell characteristic causes significant damage (around 9 billion US dollars annually) [2]. For example, pavements on expansive soils register the poorest performance. When the soil expands, it creates an uplifting force on the pavement, causing damage such as cracking and differential vertical movement. This volume instability significantly reduces the performance life of the pavement. In the US, significant amounts of shrink-swell clays are found in Texas, Colorado, and California. Over the years, techniques used to stabilized these soils include thermal, electrical, mechanical, and, chemical means to reduce the shrink-swell behavior and also to improve the strength and stiffness properties. Mechanical compaction involves densification of the soil by application of mechanical energy. It removes air from the soil without a significant change in moisture content. It is used for cohesive and cohesionless soils but the efficacy of the technique reduces if the soil is subjected to varying moisture levels. Thermal and electrical stabilization are not popular due to the high costs associated with them. Chemical modification and stabilization of the soil is a more effective and durable method for stabilizing cohesive soils.

Chemical stabilizers can be of different types. Depending on the chemical composition, they can be broadly classified into two categories (1) calcium-based stabilizers (pozzolanic materials) such as lime, cement, and fly-ash (2) non-calcium-based stabilizers such as hydrogen ions stabilizers (HIS).

Calcium-based stabilizers have been used in chemical soil stabilization of soft clays due to their effectiveness in improving strength and stiffness [3]. Clay itself is a pozzolan. In the presence of moisture, a strength enhancing pozzolanic reaction is triggered by combining a pozzolanic material like ash, lime (calcium oxide) with soil. The high pH environment provided when lime dissolves in water releases pozzolans (Si and Al) from the clay to react with calcium from lime and water to form calcium-silicate-hydrates (CSH) and calcium-aluminate-hydrates (CAH). In addition, soluble sulfates can also react with the dissolved Ca and Al in the presence of water to form ettringite.

Ettringite $(Ca_6Al_2(SO_4)_3(OH)_{12} \cdot 26\text{-}32\,H_2O)$, a naturally occurring mineral can be found in hydrated cements and clayey soils stabilized using a pozzolanic material [4, 5]. It is an important hydration product contributing to early strength in low CO_2 calcium-sulfo-alumiate (CSA) cements [6]. In soils stabilized with a calcium based stabilizer forming too much ettringite post compaction can cause substantial distress and affect the durability of the material. This phenomenon of excess ettringite formation causing damage is referred to in general terms as sulfate attack. Little [7] and Puppala [8] have studied the distress mechanism of ettringite induced heave in chemically stabilized soils with high sulfate content.

Whether or not ettringite will form in lime stabilized soils is dependent on the quantity of water soluble sulfates present in the native soils to be treated [9]. Empirical analysis indicated 3000 ppm as the upper threshold level of soluble sulfate. However, this empirical assessment does not always hold valid as in some cases significant ettringite has been detected in soils with less than 1,000 ppm water soluble sulfates and in other cases no significant ettringite formation was detected in soils with over 10,000 ppm water soluble sulfate [5, 10, 11]. Several other factors such as the overall mineralogical composition of the soil and the availability of proper stoichiometric quantities of all constituents, especially water, have proven to be a key to the formation of ettringite [12, 8]. Studies have investigated the formation of ettringite using numerical modeling [13, 14] and molecular dynamics [15, 16].

For non-calcium based stabilizers like hydrogen ion stabilizer (HIS), which is a liquid ionic sta-bilizer, various reaction mechanisms have been proposed including encapsulation of clay minerals,

2

dissolution of clay minerals, removal of interlayer cation, and moisture entrapment. However, they lack strong experimental and modeling results to validate the claim(s). This has led to the lack of acceptance of such stabilizers despite the potential advantages. The lack of experimental evidence is due to poorly documented testimonials. In addition, the information provided by the manufacturer is inadequate. When hydrogen-ion based additives are used, they react chemically with expansive clay minerals like smectite releasing the Al^{3+} ions from the octahedral sheets. The released Al^{3+} ions are adsorbed on the clay surface due to the net negative surface charge of smectite [17]. This cation exchange reduces the swell characteristics of smectite. At higher concentrations of HIS, tetrahedral sheets of smectite are also partially or fully destroyed, and the breakage of SiO_2 from the tetrahedral sheet causes further structural changes [18].

1.2 Definition of problems/questions and Objectives

1.2.1 Thermodynamic modeling the effect of HIS on smectite

The effect of ionic stabilizer such as HIS on improving the engineering properties of expansive soils containing smectite is well documented [19, 20, 21, 22, 23, 24]. The treated soils have shown significant improvement in engineering properties. There is very limited literature on the stabilization mechanism. Computational chemistry using thermodynamic models have been gaining importance in the area of cement hydration modeling. The models predict cement hydration products at equilibrium. Adapting the models, to simulate the interaction between expansive soil minerals and HIS will be beneficial in understanding the stabilization mechanism. In addition, developing phase stability diagrams with the modeling results can help to determine the concentration (dosage) of HIS required to achieve significant improvement in engineering properties.

1.2.2 Predicting ettringite with thermodynamic modeling

Sulfate induced heave due to ettringite formation is a critical problem when lime or pozzolanic material is used to stabilize sulfate rich soils. Predicting ettringite formation with thermodynamic models can alleviate at least some of the risk but such model require extensive material characterization to reliably predict ettringite. For field applications, extensive characterization data may

3

not be available. Therefore, a model was setup to test two cases: (1) A case study with limited characterization data (Section 1.2.2.1) and (2) A laboratory study with sufficient characterization data (Section 1.2.2.2).

1.2.2.1 *Soil stabilized with a high sulfate ash: A case study*

Significant research has been carried out to experimentally study the formation ettringite in soils stabilized with a calcium-based stabilizers. It is generally accepted that soluble sulfates in soil play a significant role in the formation of ettringite. In most cases, it is not feasible to reduce the soluble sulfates in the soils. In such cases, non-calcium based stabilizers are considered. It would be beneficial to develop a tool that can help to predict the quantity of ettringite in a stabilized soil. Investigating the application of thermodynamic modeling to predict ettringite formation both qualitatively and quantitatively will play significant role in material selection. Furthermore, validating such a model with a case study where ettringite induced heave was determined to cause structural distress is a necessary component toward application.

1.2.2.2 *Ettringite synthesized from Ca-Al-SO$_4$ solutions*

The case study in section 1.2.2.1 indicated that additional calibration of the thermodynamic model was necessary to improve the accuracy of ettringite prediction. The calibration required extra data points covering a wider range of recorded sulfate values. This may not be a pragmatic solution. In addition, the study indicated that sufficient mineralogical data (obtained from experimental characterization) can improve the prediction accuracy. Therefore, it was necessary to investigate the reliability of the thermodynamic model in predicting ettringite when sufficient mineralogical data is available.

1.2.3 Objectives

This research is aimed towards a better understanding on the application of thermodynamic models for chemically stabilized soils. The objectives of the research are as follows:

1. Use thermodynamic models to understand the stabilization mechanism of smectite treated with a hydrogen ion stabilizer.

2. Investigate the application of thermodynamic modeling as a forensic tool to predict ettringite formation in a shopping complex where the base soil was treated with a high sulfate ash.

3. Explore the application of thermodynamic modeling to predict precipitation of solid phases including ettringite in Ca-Al-SO$_4$ solutions.

1.3 Dissertation outline

This dissertation is a synthesis of three different research tasks on the application of thermodynamic modeling for chemically stabilized soils. Two papers were published in referred journals and the third paper is under review. The dissertation is organized into six chapters. Chapter 1 introduces the topic and provides the background information. In addition, a description of the problem statement and the objectives of the three studies are described. A literature review of expansive clay mineralogy, chemical soil stabilization, and ettringite growth is presented in Chapter 2. Chapter 4 is a reprint of the paper "Thermodynamic evaluation of smectite treated with Hydrogen Ion Stabilizer" whose final version was published in the ASCE: Journal of Materials in Civil Engineering. The authors of this are paper Pavan Akula, Dallas Little and Paul Schwab. Chapter 4 is a reprint of the paper entitled "Coupled thermodynamic and experimental approach to evaluate ettringite formation in a soil stabilized with fluidized bed ash by-product: A case study" published in the Journal of Transportation Geotechnics. Chapter 5 is a paper that demonstrates the application of thermodynamic modeling in predicting ettringite formation. The paper was submitted to the Journal of Construction and Building Materials and is currently under review. Finally, Chapter 6 presents the conclusions drawn from the research and recommendations for future related research.

2. THERMODYNAMIC MODELING

The geochemistry of chemically stabilized soils play a critical role in the behavior of the materials. Their natural chemical states, dissolution and precipitation will provide additional information on equilibrium thermodynamics and phase stability. In a simple geochemical system, this can be evaluated using hand calculations [25]. As we encounter more complex problems, we rely on thermodynamic models to find the solution. Such complex models have been used widely in the field of soil science and soil mineralogy to understand sediment and hydrothermal alteration, ore deposits, and to determine which contaminants will leach from mine wastes [26]. They can be adapted to model civil engineering problems such as to investigate the stabilization mechanism of expansive clays treated with non-calcium based stabilizer (Hydrogen ion stabilizer) and formation of ettringite due to sulfate attack. It is a powerful tool that utilizes the concept of free energy minimization to predict the reaction products at equilibrium. They can simulate thousands of reactions, some of which yield products that provide reactants to other reactions. Identifying the reactions that are important, and the reaction path followed by these reactions will provide us a deeper understanding on the factors that contribute to the formation of products at equilibrium.

Thermodynamic models are primarily based on two methods. One method uses the parameter Gibbs' free energy (G) to solve the equilibrium problem by minimizing the free energy of the system. The second method uses equilibrium constants (Law-of-Mass-Action) which are mathematical expressions of the minimum value of the Gibbs free energy reaction [27]. Each model has its own advantages and will converge to the point of minimum free energy.

2.1 Law-of-Mass-Action (LMA)

The LMA approach is based on equilibrium constants (K). They are calculated at the point of equilibrium or minimum Gibb's free energy. Thermodynamic modeling programs such as Visual MINTEQ, Geochemist's Workbench, and PHREEQC are based on this approach. The chemical species in this approach are built on components that are the fundamental building blocks of the

model. For example, Ca^{2+} must be the component form for calcium. The thermodynamic database, written in terms of these components, is searched automatically to retrieve only those species relevant to a specific problem. A database contains thermodynamic data such as the equilibrium constants (K) of various phases, and enthalpy of formation and reaction. The value of the equilibrium constant is dependent on temperature and pressure. Therefore, a database can also contain the pressure and temperature at which the thermodynamic data were recorded.

A chemical system consisting of n independent components can combine to form m species. Mathematically this can be represented as

$$K_i = S_i \prod_{j=1}^{n} X_j^{-a_{ij}} \tag{2.1}$$

where , K_i is the solubility constant of the species i, S_i is the activity of the species i, X_j is the activity of component j, and a_{ij} is the stoichiometric coefficient of component j in species i. Rearranging to express concentration C_i in terms of activities, we get

$$C_i = \frac{S_i}{\gamma_i} \prod_{j=1}^{n} X_j^{-a_{ij}} \tag{2.2}$$

where, γ_i is the activity coefficient. Equation 2.2 represented in terms of mass balance becomes

$$Y_j = \sum_{i=1}^{n} a_{ij} C_i - T_j \tag{2.3}$$

where, Y_j is the difference between the calculated concentration and the total concentration (input parameter).

To maintain mass balance, the calculated concentration of a component must be equal to the total concentration. The mathematical solution is a series of component activities from which the concentration can be calculated using Equation 2.2. In practice, it is only necessary to find X such that Y is reduced to an acceptable value (tolerance value). Solvers based on the Newton Rapson approach are used to calculate X from a initial approximation. Parameters C and Y can then be

calculated. If the values of Y exceeds the acceptable value, a new value of X is used. This iterative procedure continues until all the values of Y fall within the acceptable range.

Visual MINTEQ uses a Jacobian matrix with the following formula to calculate a new X_i at each iteration (Equation 2.4). The elements of the Jacobian matrix represents partial derivatives of each component mass balance difference Y_j with respect to every other component activity X_k

$$u_{j,k} = \frac{\delta Y_j}{\delta X_k} = \sum_{i=1}^{n} a_{ij} \frac{\delta C_i}{\delta X_k} \qquad (2.4)$$

2.2 Gibbs' Energy Minimization (GEM)

The GEMS model specifies the total amount of chemical species, elements and a charge balance. This approach is based on mass balance of the entire system. The elements and electric charges are called as independent components (IC's $\in N$) and the species are called as dependent components (DC's $\in L$). In addition, GEMS explicitly defines thermodynamic phases (ϕ) that can contain one or more dependent component. For example, montmorillonite with Na^+ and Ca^{2+} in the interlayer can be defined under the same thermodynamic phase. Unlike the LMA based approach, the GEM method calculates the activities and concentration of dependent components separately by considering appropriate reference states and activity coefficients. The GEM interior point algorithm (IPM) calculates the speciation vector x that contains the molar quantity of DC. In addition, it also calculates a vector u containing the chemical potential of independent components.

The goal of the GEM approach is to find a set of dependent components that satisfy the mass balance ($Ax = b$) and Gibb's energy minimization criteria (G) [28]. It can be represented as follows:

$$G(x) \Rightarrow min, \text{subject to } Ax = b$$

where x be a set of dependent components (DC), where $x = \{x_j, j \in L\}$, at $G(x) = min$
where $A = \{a_{ij}, i \in N, j \in L\}$ is a matrix that contains the stoichiometric coefficients of $i - th$ IC in the $j - th$ DC, $b = \{b_i, i \in N\}$ is the input parameter that contains the total mole amounts

of IC.

Therefore, the Gibbs' free energy of the whole system can be represented as

$$G(x) = \sum_k \sum_j x_j v_j, j \in L_k, k \in \phi \tag{2.5}$$

In Equation 2.5, L_k is a subset of DC in the $k - th$ phase and v_j is the chemical potential of the $j - th$ DC

$$v_j = \frac{G_{j,T}^o}{RT} + lnC_j + ln\gamma_j + C_F + constant, j \in L_k \tag{2.6}$$

where $G_{j,T}^o$ is the standard molar Gibbs' free energy taken from the thermodynamic database, R = 8.314 $J.K^{-1}.mol^{-1}$ and T is the temperature in Kelvin. C_j is the concentration, γ_j is the activity coefficient of the $j - th$ DC, C_F is the Coulombic parameter used for charged surface complexes.

As indicated earlier, the IPM algorithm calculates the primal vector x and dual vector u. This is carried out by checking the Karpov-Kuhn-Tucker (KKT) conditions (Equation 2.7)

$$v_j - \sum_i a_{ij} u_i \geq 0, i \in N \tag{2.7}$$

where v_j is calculated from the equilibrium mole amount x_j and standard molar Gibbs' free energy G_j^0 (Equation 2.6)

For any species in any phase at equilibrium, Equation 2.6 and 2.7 can be combined to form

$$\sum_i a_{ij} u_i = \frac{G_{j,T}^o}{RT} + lnC_j + ln\gamma_j + C_F + constant \tag{2.8}$$

Equation 2.8 is used by the GEM IPM algorithm to calculate the following

1. Activities of solid, aqueous and gaseous species.

2. Saturation indices of species/ phases.

3. Activity function such pH, pe and Eh.

3. LITERATURE REVIEW

3.1 Introduction

This chapter presents the background and literature review. A discussion is presented on the structure and characterization methods used to detect expansive and non-expansive clay minerals. In addition, the use of chemical soil stabilizers including conventional stabilizer such as hydrated lime, fly ash and non-conventional stabilizers such as hydrogen ion stabilizer is explained. Ettringite induced heave is described by highlighting the mineralogical structure, precipitation, and growth mechanism of ettringite. Finally, a brief review of past studies using thermodynamic models is also presented.

3.2 Classification of soil minerals

Classes of minerals often are based on their chemical composition, including (1) native elements, (2) sulfides, (3) sulfosalts, (4) oxides and hydroxides, (5) carbonates, (6) halides, (7) nitrates, (8) borates, (9) phosphates, (10) sulfates, (11) tungstates, and (12) silicates [29]. Silicate minerals have a pronounced effect on the soil chemistry and reactivity. Therefore, they play a significant role chemical soil stabilization. Clays fall under the silicates groups. Depending on the crystal structure and chemical composition, the silicates group is subdivide into tectosilicates (framework silicates), phyllosilicates (sheet silicates) and other silicates Figure 4.1.

3.2.1 Clay minerals

Clay minerals are predominantly layered type aluminosilicates and fall under the phyllosilicates group. The layered structure is due to the presence of silica tetrahedral and alumina octahedral sheets. Depending on the position of the layer, they are further subdivided into 1:1 or 2:1 aluminosilicates. Kaolinite, a non-expansive clay mineral falls under the 1:1 group with one tetrahedral and one octahedral layer. Smectite, an expansive clay mineral falls under the 2:1 group with two tetrahedral and one octahedral layer.
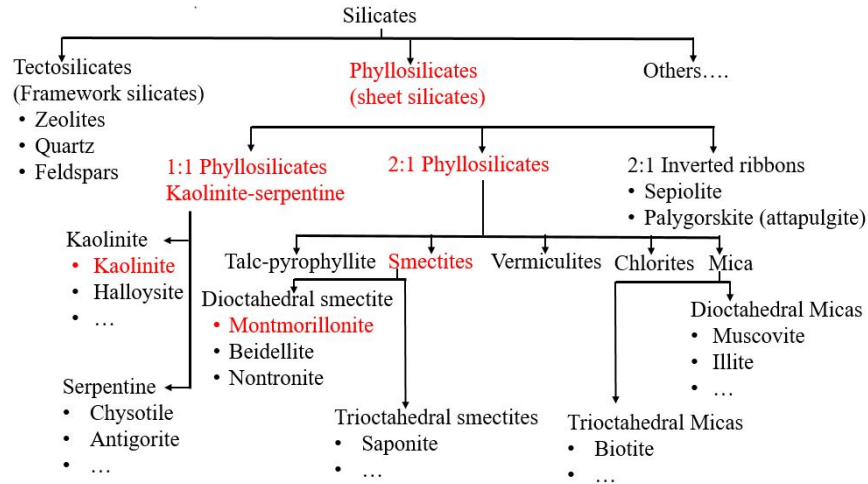
Figure 3.1: Classification of silicates group of soil minerals [30]. "Reprinted with permission from Spring Nature Copyright 2016"

At a group level, clays with a 1:1 structure are identified as kaolinite. This 1:1 phyllosilicate mineral is relatively pure with little to no isomorphic substitution. The lack of isomorphic substitution generates negligible surface charge leading to reduced shrink-swell potential. For examples, clay minerals under the kaolinite group do not swell in the presence of water. The typical structure (1/2 unit cell) of a kaolinite ($Al_2Si_2O_5(OH)_4$) is shown in Figure 3.2. It is composed of octahedral sheet with Al^{3+} as the coordinating cation and tetrahedral sheet with silica as the coordinating cation. The layers of kaolinite comprising the tetrahedral and octahedral sheets are held together by hydrogen bonding are not easily separated. The surface area of kaolinite ranges from 10 to 20 m^2g^{-1} with litte to no surface charge.

The 2:1 phyllosilicate minerals vary considerable in the physico-chemical behavior. Smectite is a predominant 2:1 phyllosilicate mineral, which is also referred as a shrink-swell clay [32]. This group of minerals has a net surface charge between 0.2 and 0.6 per 1/2 unit cell. The layer charge originates from the isomorphic substitution. In montmorillonite, (a smectite group mineral), a layer charge of 0.4 arises from the substitution of 0.4 Mg^{2+} atoms for Al^{3+} atoms in the octahedral layer (isomorphic substitution). Figure 3.3 shows structure of montmorillonite $Na_{0.4}(Al_{1.6}Mg_{0.4})Si_4O_{10}(OH)_2$. The layer charge of montmorillonite is neutralized by a weakly
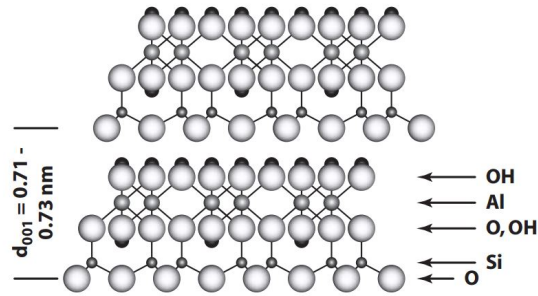
Figure 3.2: Structure of kaolinite ($Al_2Si_2O_5(OH)_4$)[31]. "Reprinted with permission from Taylor and Francis Group LLC (Books) US".

bonded Na^+ atom in the interlayer. In the presence of moisture, exchangeable water molecules are also weakly bonded on the surface (Figure 3.3), which causes the characteristic swell.
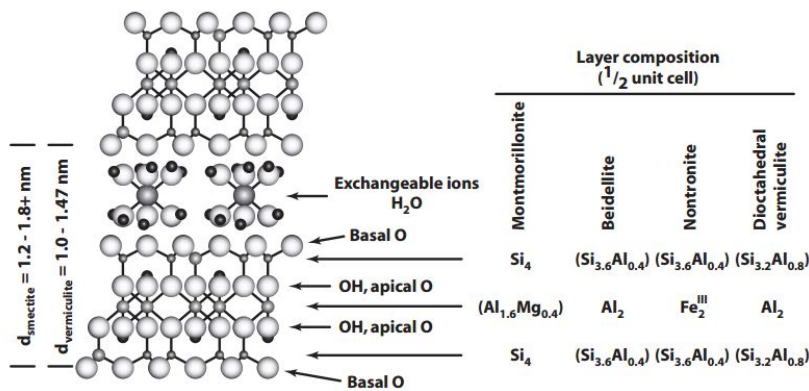
Figure 3.3: Expanded structure of montmorillonite with H_2O in the interlayer [31]. "Reprinted with permission from Taylor and Francis Group LLC (Books) US".

3.2.2   Use of chemical stabilizers on expansive clay minerals

Expansive soils are distributed across the U.S. and are found extensively in Texas (Figure 3.4). Stabilization of clays is important because of the damage resulting from moisture induced heave. Initially, engineers used trial-and-error approaches to solve this problem. They found that mechanical stabilization requires alteration of physicochemical properties for permanent stabilization.
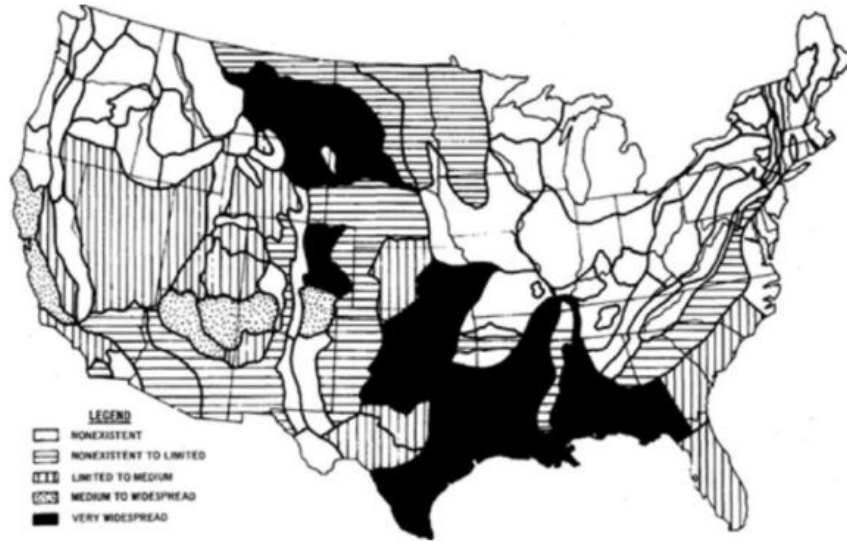
Figure 3.4: Distribution of expansive clays in the US [33]. "Reprinted with permission from Transportation Research Board"

Soil scientists and mineralogists [34, 35] paved the way for the study of chemical stabilizers on expansive clay minerals. Over the years, several types of chemical stabilizers have been effectively used to treat expansive soils. They can be broadly classified into traditional stabilizers including lime, cement, fly ash, and ground granulated blast furnace slag and non-traditional stabilizers including liquid ionic stabilizers, and hydrogen ions stabilizers. The objective of a chemical stabilizer is to modify and stabilize the soil, and thereby improve engineering properties of the soil. For example, lime treated expansive clays show a reduction in swell potential and an increase in unconfined compressive strength. Several studies have demonstrated the effectiveness of non-traditional chemical stabilization of clayey soils including HIS [36, 37, 38, 39, 40, 41], polymers [42], geo-polymers, potassium rich systems [43] and enzymes [44, 45, 46].

3.2.2.1 Pozzolanic stabilizers

Calcium based additives like fly ash, lime, cement, and cement kiln dust can be used to improve the engineering properties like strength and stability of soil. The additives are traditionally referred to as pozzolanic stabilizers. Pozzolanic stabilizers fall under the traditional stabilizer category as

13

they are widely used and studied for stabilization of base soils in pavements. Lime has been extensively used to treat highway and foundation subgrade soils (Figure 3.5) [2]. Lime treatment enhances the workability, engineering properties and reduces the shrink-swell behavior [47, 48, 49, 50].

Figure 3.5: State use of lime in highway pavement construction. "Reprinted from [51, 52]"

Typically, when lime or similar pozzolanic stabilizers are added to the soil, the chemical reaction starts almost immediately. When lime (CaO) is added to soil with moisture, it hydrates and releases heat which dries the soil (Equation 3.1). In addition, the moisture present in the soil is also used to hydrate lime which further dries the soil.

$$CaO + H_2O \longrightarrow Ca(OH)_2 + Heat \tag{3.1}$$

$$Ca(OH)_2 \longrightarrow Ca^{2+} + 2\,OH^- \tag{3.2}$$

This is followed by modification of the clay mineral that takes place when the Ca^{2+} ions from hydrated lime (Equation 3.2) migrate to the net negative surface that reduces the water affinity of

clays (Figure 3.6). The reaction reduces the plasticity index of the soil as it becomes granular. This process is referred to as "flocculation and agglomeration" and it happens in the first few hours.
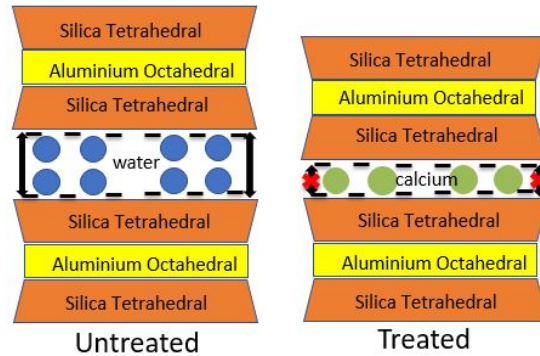
Figure 3.6: Stabilization mechanism of lime treated clays

When adequate quantity of lime is added (pH >10.5), the increase in pH favors dissolution clay minerals. The dissolution or breakage releases free alumina and silica that reacts with Ca^{2+} from lime to form calcium-silicate-hydrates (CSH) and calcium-aluminate-hydrates (CAH) in the presence of moisture. CSH and CAH are pozzolanic products that holds the soil matrix together contributing to the increased strength. A comparison between lime and other pozzolanic stabilizers is presented in Table 3.1.

3.2.2.2 *Non-pozzolanic stabilizers*

Common non-pozzolanic stabilizers include liquid ionic stabilizers such as HIS. They can be alkaline or acidic in nature. In most cases, the stabilizers are sold as concentrated solutions and are diluted before injecting into the soil. The significant reduction in cost and an appreciable improvement in engineering properties make them a good alternative chemical stabilizer [53, 54]. Scholen [55] indicated the ionic stabilizer initiates cation exchange with the expansive clay minerals that promotes flocculation. Tingle [56] also indicated that the ionic stabilizer altered the concentration of the pore fluid, resulting in ion exchange that may cause flocculation of the clay minerals. Wang

Table 3.1: Comparison of popular pozzolanic stabilizers

Stabilizer	Method	Effects	Limitations
Lime	Drying and modification of the clay particles. The drying process reduces the water holding capacity and the modification process produces pozzolanic products like calcium-silicate-hydrates (CSH) and calcium-aluminate-hydrates (CAH).	Improvement to workability and an increase in strength.	Presence of excessive soluble sulfates and organic content can cause deleterious effects.
Cement	Modification of the clay particles. The presence reactive calcium-silicates and calcium-aluminates in cement enables faster pozzolanic reaction to form CSH and CAH.	Rapid increase in strength is expected.	Presence of excessive soluble sulfates and organic content can cause deleterious effects.
Fly ash	Fly ash(s) with high CaO content can modify and stabilize the soil	Slow increase in strength due to the slow rate of hydration is expected. Presence of amorphous silica reduces the risk of ettringite induced heave.	Availability can be limited and the cost of transportation can be high.

[20] observed a reduction in the total shrink-swell percentage and an improvement in the compressive strength. On the contrary, Rauch [57] did not observe any consistent or significant change in the strength of the treated soil. Akula [58] used thermodynamic modeling to study the effect of ionic stabilizers on smectite. The results indicated that the ionic stabilizer reduced the swell potential by partial dissolution of smectite.

3.3 Sulfate attack: Ettringite

Since the mid-1980s more attention has been given to sulfate induced heave in the U.S. In particular, structural distress due to heave was found in sulfate rich soils treated with calcium based materials such as lime, fly-ash and, cement [59, 60, 61, 62, 63]. Ettringite was found in the distressed areas and the heave was attributed to the expansive properties of ettringite. Sulfate attack

gained importance when Mitchell [59] reported sulfate induced heave due to ettringite formation in a case study located in Nevada. Sources of sulfate pockets can be present (Figure 3.7a) that could cause localized heave at several locations within the same project (Figure 3.7b).

<center>(a)   (b)</center>
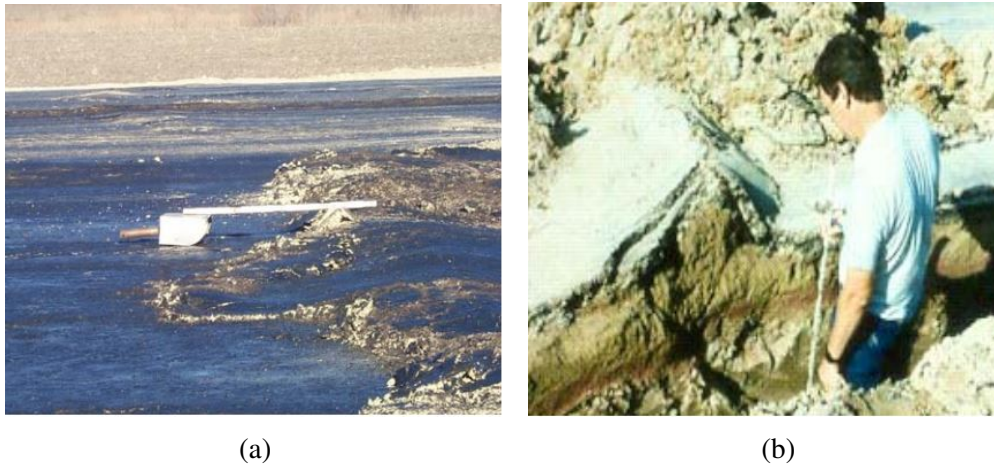
Figure 3.7: Sulfate pockets along U.S. 67 (a); Localized heave (b) gypsum layer. "Reprinted from [7, 64]"

Lime is predominantly used in Texas to stabilize expansive clays but there are also several counties in Texas (Figure 3.8) where significant levels of soluble sulfates have been recored. Therefore, it is important to address this problem.

3.3.1 Current practices

Current practices related to mitigating the risk of sulfate attack for stabilizing moderately to highly expansive soils (PI > 15) are by reducing the amount of soluble sulfates. Sulfate contents are generally expresses as ppm (part per million) or mg/kg (1ppm = 1mg/kg). The concentration of soluble sulfates is calculated in accordance to TEX-145E [65], and AASHTO-T290 [66]. Based on field observations of soluble sulfate concentrations, engineers have identified regions where significant ettringite growth is possible and also proposed recommendations for stabilizing expansive soils with soluble sulfates (Figure 3.9) . To alleviate the risk of sulfate attack, the use lime or any calcium based stabilizer is not recommended for soils with soluble sulfates greater than 8000 ppm.

<center>17</center>
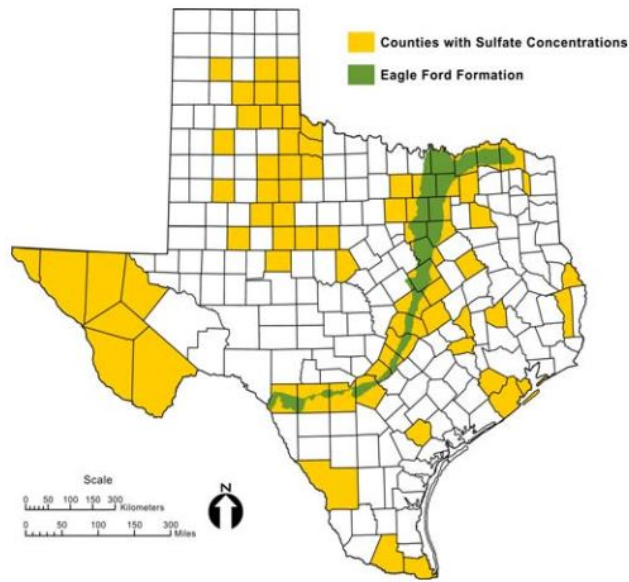
Figure 3.8: Texas counties with the sulfate concentration greater than 100 ppm. "Reprinted from [64]"

The Texas Department of Transportation (Tx-DOT) recommends a 2000 ppm of soluble sulfate as a threshold value for acceptable risk. Petry and Little [7] also proposed a similar threshold value. Mitchell [10] and Puppala [67] observed significant expansion in stabilized soils with 1000 to 2000 ppm of soluble sulfates. These observations indicate that the reactivity of soil minerals [7, 10] can play significant role in predicting sulfate attack.

3.3.2 Ettringite formation and stability

Ettringite is a calcium-alumino-sulfate-mineral that forms under alkanine condition (pH > 9.7) in soils with high sulfate activity [7, 68, 69]. It has a chemical formula $Ca_6Al_2(SO_4)_3(OH)_{12} \cdot 26\,H_2O$. Equation 3.3 shows the chemistry of ettringite formation.

$$6\,Ca^{2+} + 2\,Al^{3+} + 3\,SO_4{}^{2-} + 38\,H_2O \longrightarrow Ca_6Al_2(SO_4)_3(OH)_{12} \cdot 26\,H_2O + 12\,H^+ \qquad (3.3)$$
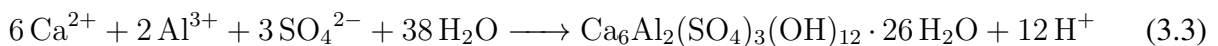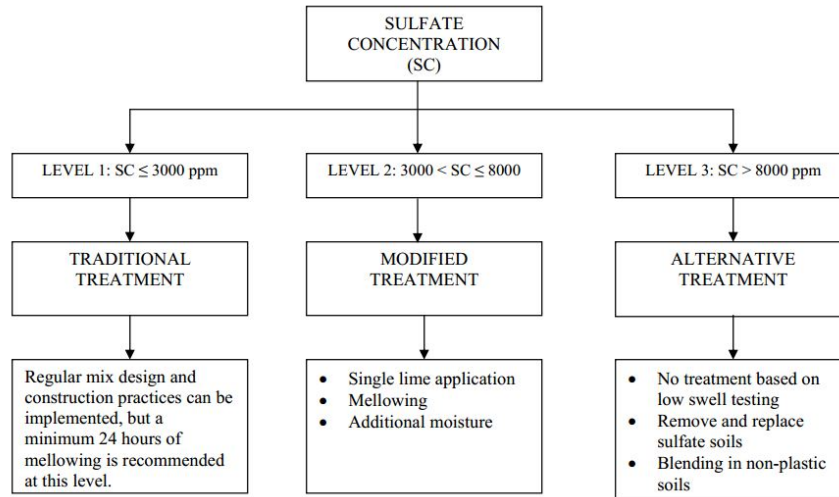
Figure 3.9: Recommended treatment decision tree based on soluble sulfate levels. "Reprinted from [64]"

For 1 mole of ettringite to form, 6 moles of Ca^{2+}, 2 moles of Al^{3+}, 12 moles of OH^- and 26 mole of water is required. In soils with high soluble sulfates, when lime or similar pozzolanic materials are added to clayey soils, the pH raises and causes partial dissolution of alumina (Al^{3+}) and silica from oxyhydroxides and phyllosilicates minerals. During this process, the Ca^{2+} from lime can react with the dissolved Al^{3+} and SO_4^{2-} ions in the presence of water to form ettringite [60, 5, 7, 10]. The stability of ettringite is defined by the activities of Ca^{2+}, Al^{3+}, SO_4^{2-} and pH. A pH of 10.7 or higher is required for ettringite to be stable. A lower pH causes incongruent dissolution of ettringite to basaluminate, gypsum and, gibbsite (Figure 3.10) [70]. Experimentally, measuring the pH is a pragmatic solution to determine ettringite stability. Water is a key compoenent for ettringite formation as it is composed of 26 moles of H_2O. Water for ettringite development can be supplied by capillary rise, diffusion, precipitation or water of construction.

3.3.3 Mineralogical structure of ettringite

Ettringite has a characteristic thin needle like structure with crystal size ranging between $2\ \mu m$ and $200 \mu m$. It is also a naturally occurring mineral but is of importance as a hydration product [71]. It has a column and channel like structure. The columns are composed of Ca^{2+} and Al^{3+} polyhedra,

19
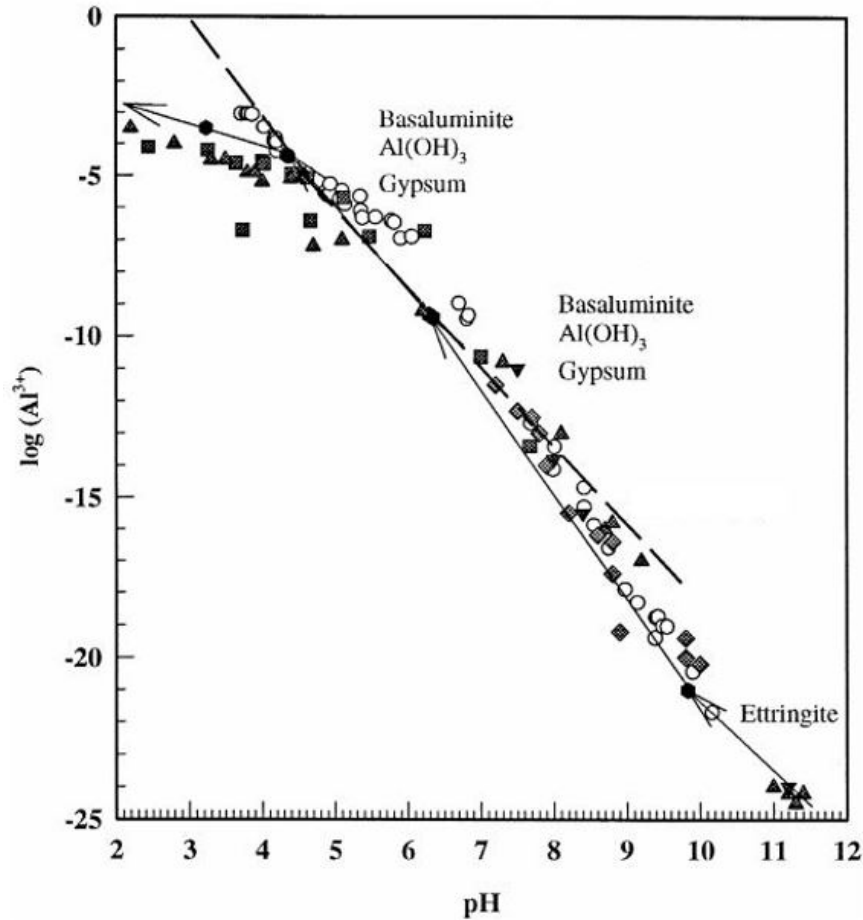
Figure 3.10: Effect of pH on ettringite [70]. "Reprinted with permission from Elsevier".

which coordinate with H_2O (Ca only), and OH (Ca^{2+} and Al^{3+}) (Figure 3.11)[72]. The outer channel has SO_4^{2-} ions that form hydrogen bonds with the calcium-coordinated water molecules. The water molecules are found at four different locations (1) the inner column channel, (2) the two apices, (3) the two apices of calcium polyhedra and, (4) at the hydroxyl ions binding Ca^{2+} and Al^{3+} ions.

3.3.4 Ettringite induced heave

When ettringite grows, it forms a branched structure as seen in Figure 3.12. The branched structure can form in two potential areas of the stabilized soils (1) in the pore space and (2) at the interface of two soil minerals. Theoretically, limited ettringite growth in the pore space can
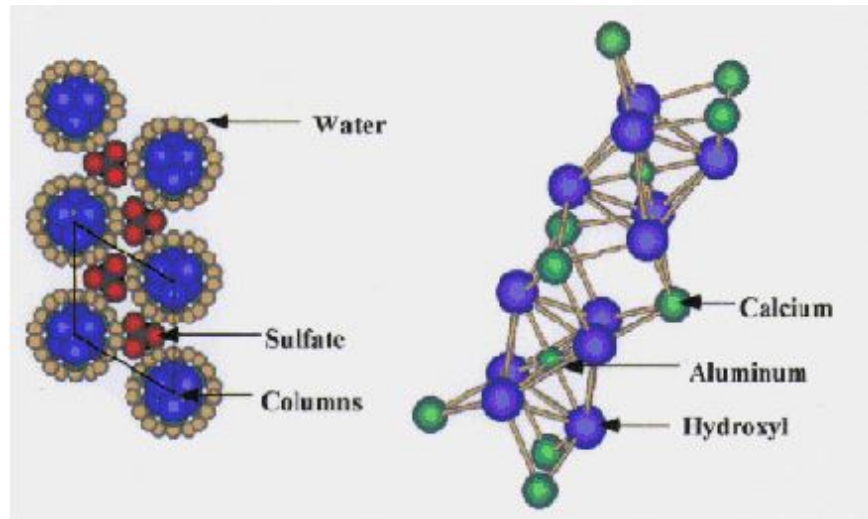
Figure 3.11: Structure of ettringite [72]. "Reprinted with permission from Elsevier".

help to increase the density and therefore improve strength but continued growth in the pore space beyond the pore volume will have deleterious effects. Growth of ettringite on the interface can cause substantial heave and distress reducing the structural integrity of the material.

In soils, the kinetics of precipitation and growth is dependent on the particle size, dissolution of soil minerals and pH. The solubility of well structured soil minerals like smectite and kaolinite is significantly lower compared with cement phases like tricalcium-aluminate (C3A). Therefore, the kinetics of ettringite formation is significantly faster in cements as compared to stabilized soils. When sufficient SO_4^{2-}, Ca^{2+} and, H_2O are available, the dissolution rate of Al^{3+} from soil minerals can affect the rate of ettringite precipitation. Soil minerals with a slow dissolution rate can form ettringite after compaction. Excess ettringite formation can cause accumulation of stress and subsequent failure of the stabilized layer. Therefore, formation of ettringite may not be deleterious if the pore volume can accommodate the growth but excessive ettringite formation (greater than the pore volume) and growth on the interface can cause significant distress.
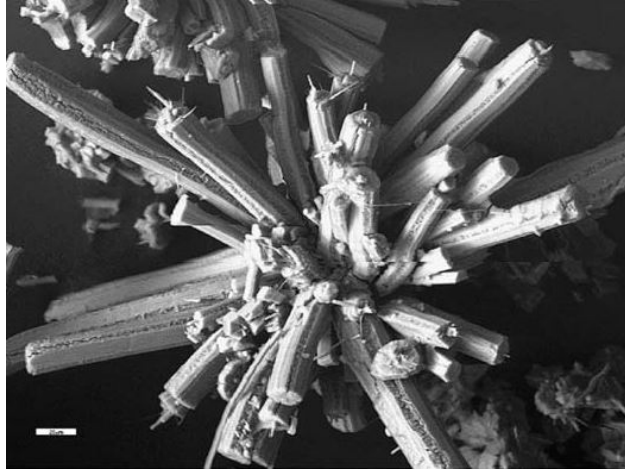
Figure 3.12: Scanning electron microscopy image of ettringite [73]. "Reprinted with permission from Elsevier".

Experimental investigation by Nair [74] compared percent soluble sulfates in soil with the percent ettringite and the percent volume change. As expected, Figure 3.13 shows a linear relationship between ettringite and volumetric change. Depending on where ettringite grows, a soil with 10% ettringite can experience close to 10% volume change (Figure 3.13).
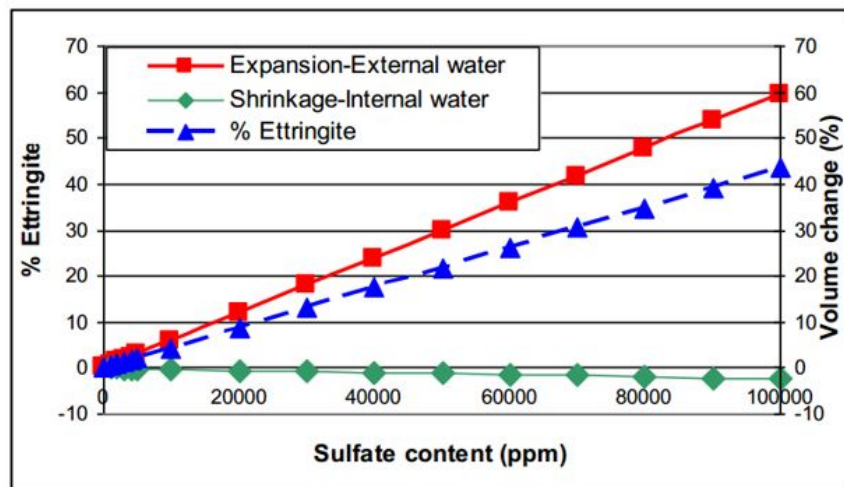
Figure 3.13: Volumetric change due to ettringite growth. "Reprinted from [74]"

3.3.5 Thermodynamic modeling of ettringite

Thermodynamic models including GEMS were developed to model hydration of cement [75], fly-ash [76, 77], and calcium-sulfoalimate (CSA) cements [6]. The model provided an added advantage of investigating the stability of metastable products. For example, ettringite is considered to be a metastable product during the initial stages (0-3 min) of cement hydration. GEM-Selektor was able to successfully predict metastable ettringite in such cases. Kinetics was incorporated into the model by using kinetic dissolution/ precipitation parameters from other studies. Parrot et. al. [78] extensively studied the kinetic dissolution of phases in portland cement which was incorporated later into the model [75]. In CSA cements, ettringite is an important hydration product that contributes to the strength and durability of the hydrated material. Winnefeld et. al. [6] showed the efficacy of using thermodynamic models to simulate hydration of CSA cements. Figure 3.14 shows a comparison between the experimental data (represented as markers) and the modeling results (represented as lines).
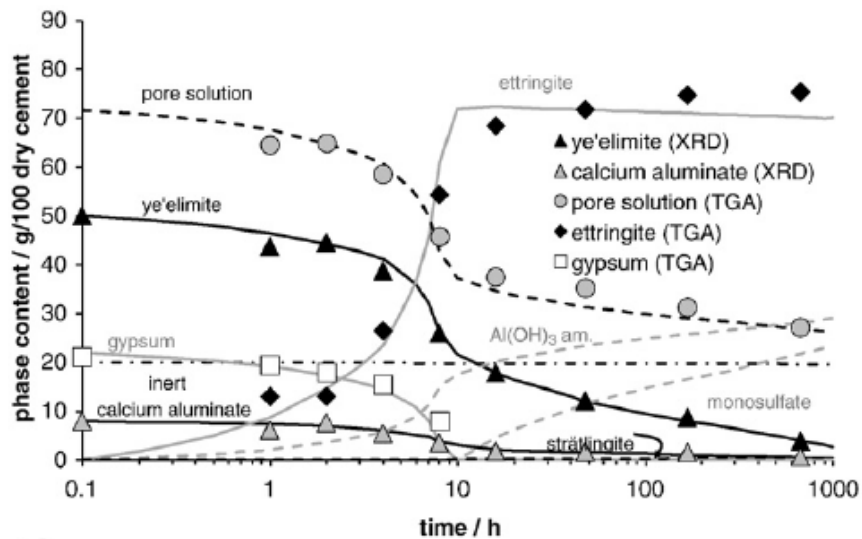
Figure 3.14: Modeled change in solid and pore solution quantity during hydration (experimental data represented as data points) [6]. "Reprinted with permission from Elsevier".

23

Kunagalli [79] studied the use of thermodynamic models to qualitatively predict ettringite for-mation in chemically stabilized soils. In the study, a law of mass action based model was used to investigate the thermodynamic favorability of ettringite. The developed phase diagrams in the study helped to investigate the stability of ettringite when a source of soluble silica was added. Fig-ure 3.15 shows that when soluble silica was added, ettringite was not thermodynamically favorable (equilibrium point: star marker).

| (a) | (b) |
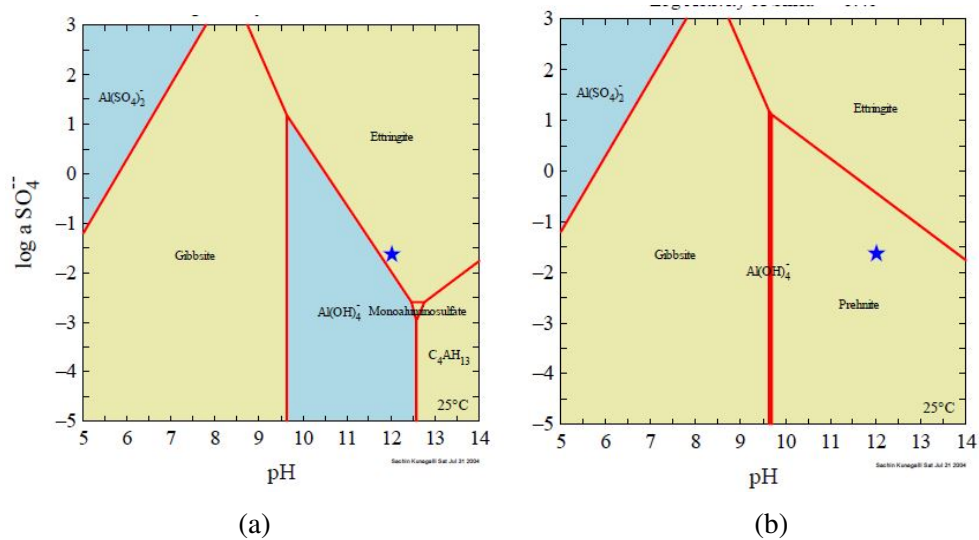
Figure 3.15: Phase stability diagrams for chemically stabilizer soils (a) without soluble silica; (b) with soluble silica [79]

3.4 Conclusion

Expansive clay minerals such as smectite are predominant in various parts of the U.S. Calcium based stabilizers and non-calcium based stabilizers are used to reduce the shrink-swell potential and to improve the engineering properties (e.g., strength, stiffness, permeability) of the soil. The use of calcium based stabilizers in a sulfate rich soils can cause sulfate induced heave due to ettringite formation. Current practice to alleviate the risk of sulfate attack involves limiting the soluble sulfate levels to less than 3000 ppm. This threshold sulfate levels are proven to work for most cases but some studies have also reported damage due to sulfate attack at lower soluble sulfate

24

values (100-1000 ppm). The possible reason was identified as the reactivity of the soil minerals. Thermodynamic models have been applied successfully to simulate hydration reactions in cement, fly-ash and calcium-sulfo-aluminate cements. In addition, developing a phase stability diagram to determine the thermodynamically favored phase can help to select stabilizers. For example, a phase stability diagram to determine the formation of ettringite can be help to select a stabilizer that has the least potential to form ettringite. For non-pozzolanic stabilizers, phase diagrams can be used an aid to postulate the stabilization mechanism. For example, the required concentration of a liquid ionic stabilizer such as hydrogen ion stabilizer and a hypothetical stabilization mechanism can be derived from a phase diagram. Therefore, thermodynamic models can be used in tandem with the engineering tests to improve the efficacy of chemically stabilized soil.

4. THERMODYNAMIC EVALUATION OF SMECTITE TREATED WITH HYDROGEN ION STABILIZER*

4.1 Introduction

Expansive clays are abundant in Texas [80]. The expansive nature is primarily due to the presence of minerals that shrink and swell, such as smectite. In the presence of moisture, smectite swells up to 300% of its initial volume [1]. During dry seasons, smectite shrinks by releasing moisture. This shrink-swell characteristic causes significant damage (around 9 billion US dollars annually) [2]. For example, pavements on expansive soils register the poorest performance. When the soil expands, it creates an uplifting force on the pavement, causing damage such as cracking and differential vertical movement. This volume instability significantly reduces the performance life of the pavement. Various methods have been developed to address this problem, including mechanical compaction and chemical stabilization with lime and/or Portland cement ([81], [82]). Acidification with strong inorganic acids has also been used, and these acids are classified as stabilizers ([83]) due to reduction in shrink-swell characteristics of smectite. Malek ([37]) studied the effect of acid stabilization on the geotechnical properties of montmorillonite and reported an increase in effective shear strength and angle of internal friction when environmental chemical soil stabilizer (ECSS-3000$^{\text{TM}}$, a hydrogen ion based stabilizer) was added to a 22% bentonite and 78% sand mixture. Sarkar ([39]) described a reduction in shrink-swell behavior and increase in stiffness of smectite soil treated with HIS. Acid modification of smectite has been studied frequently ([84], [85], [58] and [86]). Carrado and Komadel ([85]) proposed that adding acid to bentonite causes surface modifications and the release and exchange of Al^{3+}, Fe^{3+} and Mg^{2+} from the octahedral layer of smectite for H^+ ions. Tomic ([87]) demonstrated the reduction of physico-chemical activity of smectite with the addition of acid.

Several studies have demonstrated the effectiveness of chemical stabilization of clayey soils including the hydrogen ion-based additive ([36], [37], [38], [39], [40], [41]), polymers ([42]), geo-polymers, potassium rich systems ([43]) and enzymes ([44], [45], [46]). The literature concentrates on changes in engineering properties, but there is a deficit of information describing changes at a molecular level (e.g. release of Al^{3+} ions from smectite) that cause macroscopic changes (e.g. 1D swell test). When hydrogen-ion based (acid) additives are used, the Al^{3+} ions released from the octahedral sheets can be adsorbed on the clay colloids due to the net negative charge on the surface of smectite resulting from isomorphous substitution [17]. This cation exchange reduces the swell characteristic of smectite. At higher concentrations of acid treatment, tetrahedral sheets of smectite are partially or fully destroyed, and the breakage of SiO_2 from the tetrahedral sheet causes further structural changes [18]. This paper presents a unique perspective that links these mechanisms using a Gibb's free energy minimization model and provides a protocol that can also be used to simulate the interaction of chemical stabilizers (e.g. lime and/ or portland cement) with expansive soils. For example, in a lime stabilized soil system, a similar thermodynamic model can be used to simulate the stabilization reactions and determine the formation of end products such as ettringite, which can have a deleterious effect on the stabilized pavement or foundation layer due to excessive expansion.

Analytical methods such as X-Ray diffraction (XRD) and Fourier-transform infrared spectroscopy (FTIR) have been used extensively to study the swelling behavior of montmorillonite [88]. In particular, FTIR is useful in monitoring the smectite-HIS interaction [89]. A specific functional group of smectite such as Si-O and Al-Al-OH will absorb a specific wavelength of the electro-magnetic spectra. The absorbed or transmitted wavelengths are used to qualitatively assess changes in functional groups.

With advances in computational thermodynamics, the stabilization mechanism of smectite treated with a chemical stabilizer (e.g. HIS) can be simulated. In this paper, we calculated chemical and phase equilibrium using two Gibb's free energy minimization models, (1) Visual MINTEQ [90] to model the reaction between HIS and smectite; (2) Geochemist's Workbench [91] to con-

struct phase stability diagram and to determine the equilibrium points. This is an efficient, reliable and straightforward way to model chemical speciation. The objective of the research was not to prove the effect of acid stabilization but rather to demonstrate the efficacy of the application of thermodynamic-based modeling coupled with analytical testing methods including XRD and FTIR.

4.1.1 Thermodynamic modeling

Thermodynamic models are primarily based on two methods. One method uses optimization theories to solve the equilibrium problem by minimizing Gibb's free energy. The second method uses equilibrium constants, which are mathematical expressions of the minimum point in the Gibb's free energy reaction. Each approach has its own advantages and will converge to the point of minimum free energy [92]. Multi-phase systems can be modeled using Gibb's free energy with less complexity than by using equilibrium constants. The method based on Gibb's free energy has the advantage of using thermodynamic constants available in the literature for the constituents of concern in this work. These include enthalpy and entropy. The models (e.g GEM-Selektor [93]) use optimization theory to solve the equilibrium problem by "minimizing free energy directly" [94]. Equilibrium constant based models (e.g. Visual MINTEQ and Geochemist's Workbench) require only the value of the thermodynamic equilibrium constant $logK$. The models use the Newton-Raphson method to identify phases at equilibrium and does so with a very good precision. The complexity of the model increases in a multi-phase system and the information regarding the stable solids and aqueous species must be known in advance. The value of $logK$ is a mathematical expression of minimized free energy and so, both the models will converge to the same solution. The equilibrium constant ($logK$) approach indicates the final equilibrium of the entire system - solution species, gas species, redox equilibrium and solid phases.

The value of $logK$ for different phases (solids, gases, and liquids) is available in the Visual MINTEQ's database [90]. In addition to the thermodynamic parameter $logK$, the database contains the reactions of solid and aqueous phases.

The value of $logK$ from the database was used to calculate equilibrium activities and the sat-

uration index ($log(Q/K)$. The term Q, which is the ratio of the product (multiplication) of the activities of products to the product of the activities of reactants, was used to check the state of the reaction with respect to equilibrium at specific points. In addition to the equilibrium constant of smectite, additional phases such as $Al(OH)_3$(am), SiO_2(am), and aqueous species such as Al^{3+}, Mg^{2+}, Na^+ and H_4SiO_4(aq), were considered in the model. The equilibrium constants of all the phases used in the model are shown in Table 4.1.

Table 4.1: Equilibrium constants used in the geochemical model (Visual MINTEQ and Geo-chemist's Workbench)

Chemical Reaction (1)	log K (2)
$Smectite(Na_{0.6}Mg_{0.6}Al_{1.4}Si_4O_{10}(OH)_2)$ + $6H^+$ +$4H_2O$ ↔ $1.4Al^{3+} + 0.6Mg^{2+} + 0.6Na^+ + 4H_4SiO_4$	6.0
$SiO_2(am) + 2H_2O \leftrightarrow H_4SiO_4(aq)$	-2.7
$Al(OH)_3(am) + 3H^+ \leftrightarrow Al^{3+} + 3H_2O$	10.5

Geochemical models such as Visual MINTEQ and Geochemist's Workbench use the law of mass action to determine equilibrium products. The theory can be explained using the dissolution reaction of smectite:

$$Smectite + 6H^+ + 4H_2O \leftrightarrow 1.4Al^{3+} + 0.6Mg^{2+} + 0.6Na^+ + 4H_4SiO_4 \qquad (4.1)$$
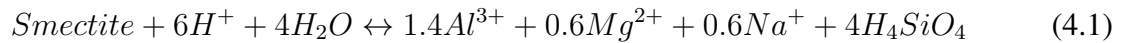
From Equation 4.1, the activity product of smectite is written as

$$Q = \frac{(Na^+)^{0.6}(Mg^{2+})^{0.6}(Al^{3+})^{1.4}(H_4SiO_4)^4}{(H^+)^6(H_2O)^4(Smectite)} \qquad (4.2)$$

where, Q is a reaction quotient and (Na^+), (Mg^{2+}), (Al^{3+}), (H_4SiO_4), (H^+), (H_2O) are the activities of smectite's phase components. Under equilibrium conditions, Q equals K. At non-equilibrium conditions, the activities of smectite's phase components are different than at equilibrium conditions. Activity is related to the concentration by the relationship.

$$(a) = \gamma[C] \tag{4.3}$$

where, $[C]$ is the concentration, γ is the single ion activity coefficient and (a) is the activity of the phase. The value of γ is dependent on the ionic strength, charge of the ions and diameter of the ions.

If concentrations of components of smectite are known, the value of Q can be calculated from Equation 4.2. The activities of components after the addition of HIS were calculated using Equation 4.3.

The direction of the reaction (dissolution or precipitation) and the saturation state of phases can be determined by comparing the value of K with the calculated value of Q. In Equation 4.2, addition of HIS would increase the concentration of H$^+$ ions. When $Q > K$, the solution is super-saturated with respect to the solid phase in question and contains sufficient concentrations of the soluble species to form smectite. Hence precipitation of smectite is favored under such conditions (insufficient concentration of H$^+$ ions to cause a chemical change). When $Q < K$, the solution is under-saturated and the complete dissolution of smectite is favored (sufficient concentration of H$^+$ ions to cause a chemical change). When $Q = K$, the reaction is considered to be at equilibrium where precipitation and dissolution occur at equal rates.

Dissolution of smectite is favored when it reacts with concentrated H$^+$ ions (acid based dissolution of smectite). During the dissolution process smectite dissociates into its individual ionic species Al^{3+}, Na$^+$, Mg^{2+}. This precipitation and dissolution reactions proceed until an equilibrium point is reached.

4.2 Materials

The source of clay in our study was commercially available smectite, Volclay90 from MTI Bio-Ag Inc [95]. The physical and chemical properties of Volclay 90 are shown in Table 4.2. The chemical stabilizer used to treat smectite increases the concentration of H^+ ions in the system and is primarily composed of sulfuric acid with traces of sulfonated naphthalene. The HIS was

provided by Environmental Soil Stabilization (ESSL LLC.). The HIS is a clear liquid with a viscosity approximately equal to that of water.

Table 4.2: Physical and Chemical Properties

Property (1)	Value (2)
Liquid Limit(%)	101.17
Plastic Limit(%)	18.02
Plasticity Index(%)	83.14
Optimum moisture content(%)	25
Bulk density (lb./cu.ft.)*	58-65
Passing Particle Size (μm)*	75
pH *	8-10.5
$SiO_2(\%)$	63.02
$Al_2O_3(\%)$	21.08
$MgO(\%)$	2.67
$Na_2O(\%)$	2.57
$Trace(\%)$	0.72

*Data provided by [95]

4.2.1 Sample Preparation

Smectite specimens were air dried for 48 hours and passed through 60 mesh size (0.250mm) sieve. Two sets of specimens were prepared at different concentrations. The first set comprised undiluted HIS added to 100 mg of smectite. The second set comprised 5% diluted (one part of HIS with 20 parts of water) HIS added to 100 mg of smectite. The treated samples were allowed to equilibrate for 48 hours prior to testing.

4.3 Methods

4.3.1 Modeling method

A two-step approach was used to simulate the reaction of smectite with HIS as shown in Figure 4.1. First, we determined the activities and concentration of solid and aqueous phases for untreated

and treated smectite. Smectite was added as a finite solid at 1.5 M (582 g/L) as the initial input to visual MINTEQ. Al(OH)$_3$(am) and SiO$_2$(am) were added as possible solid phases and the equilibrium constant for Na-montmorillonite (smectite) was manually added to the MINTEQ database. Undiluted HIS was found to be 30 M in H$^+$, while the 5% diluted material was 1.5 M in H$^+$, and the control sample contained no HIS. These concentrations were used as inputs for Visual MINTEQ modeling. The model calculated the changes in constituent concentrations in smectite, precipitation of possible solids, and concentrations and activities of all soluble species associated with the component species Al^{3+}, Mg^{2+}, and H$_4$SiO$_4$. The activities were then used in Geochemist's Workbench to develop the phase stability diagram.

4.3.2 Experimental Methods

The HIS treated smectite was characterized by XRD and FTIR. In addition, the shrink-swell characteristics were studied using one dimensional cyclic shrink-swell test.

4.3.2.1 X-Ray Diffraction (XRD)

A Bruker D2 automated system was used to obtain the diffractograms. Copper radiation $CuK\alpha = 1.541$Å at a current of $35kV$ was used as the X-Ray source. The XRD patterns were recorded over the range of $2° - 32°$ at a scanning rate of $2°/min$. The XRD pattern shown in Figure 4.2 demonstrates that Volclay is predominantly composed of smectite with quartz as the secondary mineral. The pattern also indicates no sign of amorphous phases in Volclay. Smectite is sensitive to moisture; the relative humidity of the smectite was controlled using saturated salt solutions following the method described in ASTM E104 ([96]). The smectite samples were equilibrated for 7 days in a humidity chamber prior to XRD testing. The effect of HIS on the d-spacing of smectite was evaluated at 30% and 95% relative humidity.

4.3.2.2 Fourier-Transform Infrared Spectroscopy (FTIR)

FTIR spectra were observed using a Thermo Nicolet 380 FTIR spectrometer. A diamond tipped ATR stage was used in the range 650-4000 cm^{-1}. Water has a wide absorbency wavelength 3500 cm^{-1} to 2500 cm^{-1}, which will affect the absorbance of other elements. The interference of
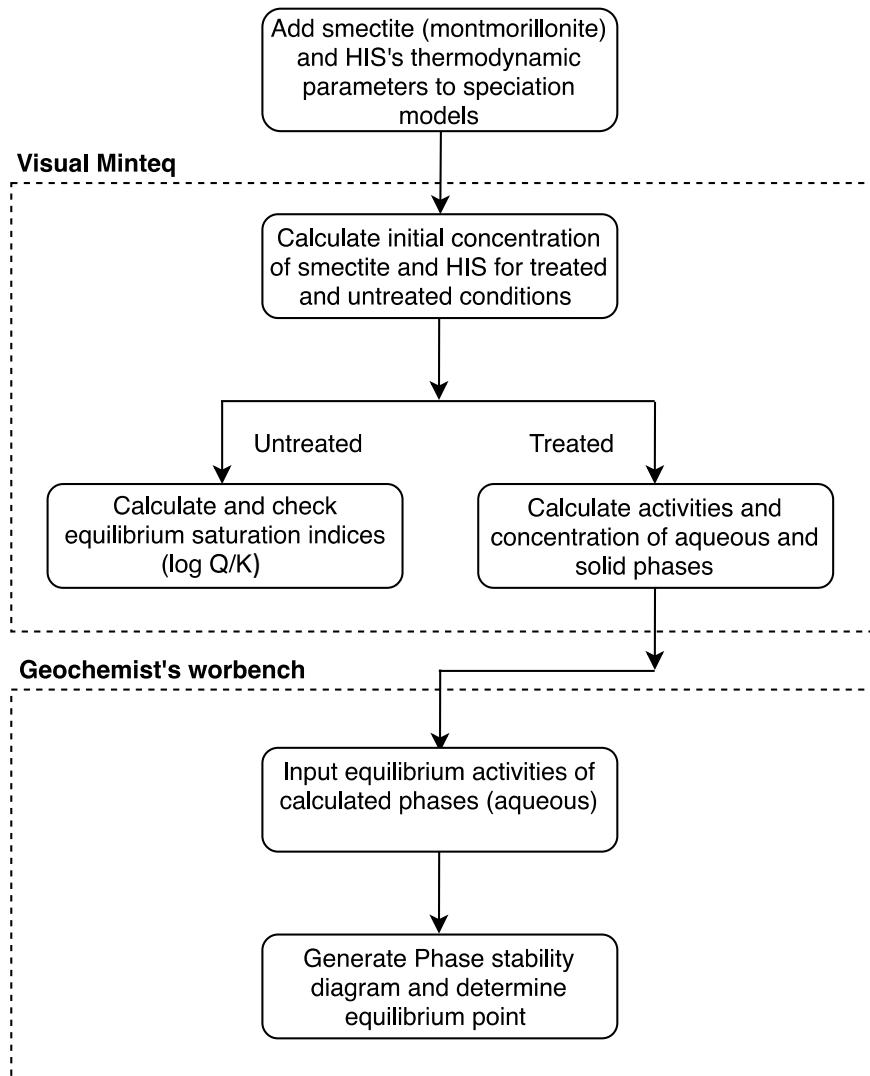
Figure 4.1: Flowchart for geochemical modeling using Gibb's technique "Reprinted with permission from ASCE: Journal of Materials in Civil Engineering".
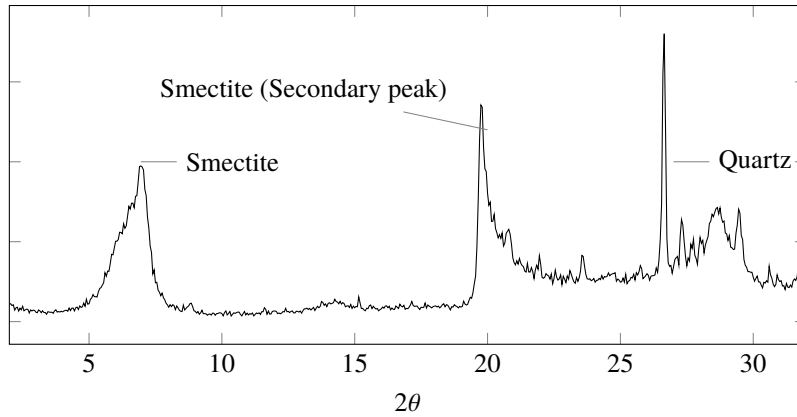
Figure 4.2: XRD pattern of smectite (volclay). "Reprinted with permission from ASCE: Journal of Materials in Civil Engineering".

absorbance bands from water molecules was minimized by drying the sample at $100°C$ overnight prior to FTIR analysis.

4.3.2.3 *One dimension cyclic swell test*

Untreated specimens were prepared by mixing 500 g of smectite with 125 ml of water (optimum moisture content calculated in accordance to [97]; Table 4.2). The treated specimens were prepared by mixing 500 g smectite with 125 ml of 5% diluted HIS. The treated and untreated specimens were cut to 76 mm (diameter) by 20 mm (high) as shown in Figure 4.3. A linear strain transducer from Humboldt (HM-2030.10) with an input of 10V was linked to data loggers (NI9237) to measure volumetric changes. The tip of the strain transducer was placed in a semicircular indent (Figure 4.3(b)) to reduce lateral movement of the transducer's tip and to improve accuracy in the measure of swell. The consolidometer was inundated with de-ionized water and swelling was measured for 120 hours. The top plate of the consolidometer was removed and the assemblage with the specimen was placed below a heat lamp at $90°C$ for 24 hours to induce shrinkage. Changes in volumetric data were recorded for three cycles of swell.
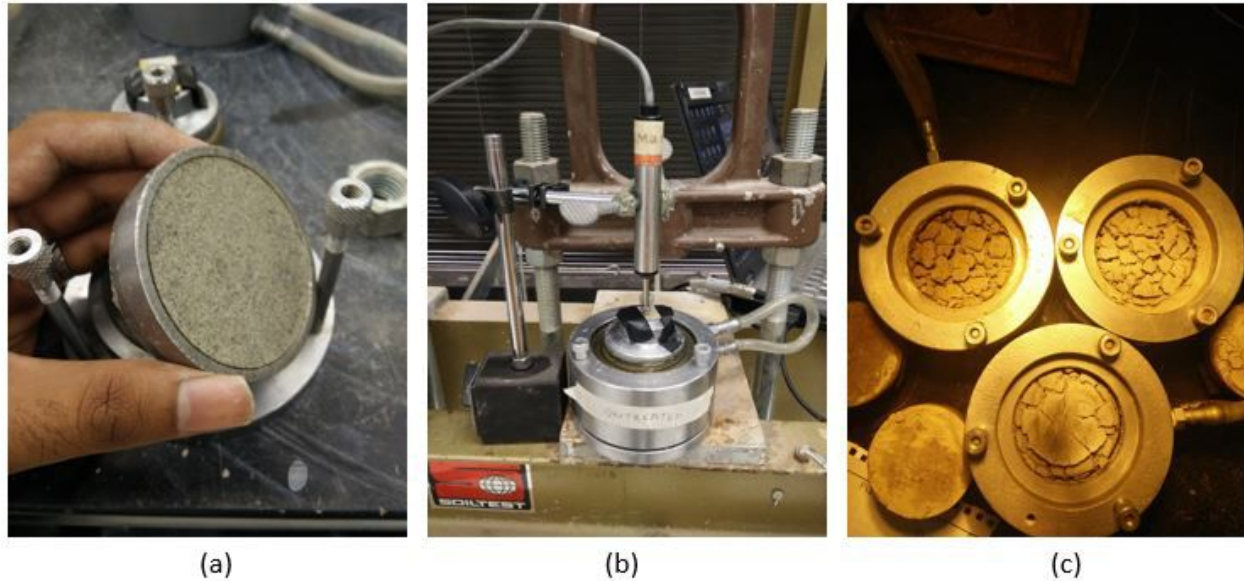
Figure 4.3: Figure 3(a): Compacted specimen, Figure 3(b): One dimensional swell test, Figure 3(c): Specimen after three cycle of wetting and drying. "Reprinted with permission from ASCE: Journal of Materials in Civil Engineering".

4.4 Results and Discussion

4.4.1 Thermodynamic Model

The first step in the process of thermodynamic modeling was to understand the crystalline structure of smectite. Smectite is comprised of two tetrahedral sheets bonded to one octahedral sheet (2:1 structure) between them. The tetrahedral sheets are primarily composed of Si-O bonds, and, because montmorillonite is dioctahedral, the octahedral layers contain alumina coordinated in an octahedral matrix to oxygen and hydroxyl (OH) groups. The negative charge occurs principally due to isomorphic substitution of Mg^{2+} for Al^{3+} in the octahedral layer. The negative charge is balanced by external adsorption of interlayer cations on interlamellar surfaces. Hydrated cations, such as Al^{3+}, Na^+, and Ca^{2+} are attracted to the negatively charged surface of smectite. The amount of water between the interlamellar layers depends upon relative humidity and the hydration enthalpy of the cations. As the quantity of water in the interlayer region increases, the mineral swells, giving smectite its characteristic shrink-swell behavior.

Addition of acidic stabilizers, such as HIS, promotes attack of octahedral sheets by H^+, releasing Al^{3+} and Mg^{2+} ions. Tomic [98] observed that 1.5 M sulfuric acid slightly decreased octahedral cations in smectites and slightly increased SiO_2 (mostly as amorphous silica). The release of Al^{3+} and Mg^{2+} from the octahedral sheet compromises the structural integrity of the crystal, and some amorphous silica is also released. At higher concentrations, the content of the octahedral cations in the mineral decreased radically, and the montmorillonite structure was significantly impacted.

Visual MINTEQ was used to predict changes in smectite composition as a function of HIS additions. Prior to the addition of HIS, smectite is the only solid phase present with little dissolution and slightly alkaline pH 8.5 (Tables 4.3 and 4.4). Activities of all cations and $H_4SiO_{4(aq)}$ are quite low: $10^{-4.25}$ M for $H_4SiO_{4(aq)}$, $10^{-15.73}$ M for Al^{3+}, and $10^{-5.0}$ for Mg^{2+} and Na^+.

With the addition of 5% HIS, the model predicts the release of octahedral and exchangeable cations and the precipitation of SiO_2(am) (Figure 4.4; Table 4.4). The high concentration of H^+ from the HIS changes the thermodynamic stability of smectite, and the concentration of components released from smectite (Al^{3+}, Mg^{2+}, and $H_4SiO_{4(aq)}$; Figure 4.4) become available for further reactions. At this 5% HIS concentration, 17% of the original smectite mass dissolved, compared to <0.1% in the untreated sample. With the precipitation of SiO_2(am) (1.01 mol/L, Figure 4), the activity of $H_4SiO_{4(aq)}$ increased to $10^{-2.78}$ M (Table 3). Concentrations of cations increased several orders of magnitude to $10^{-0.46}$ M for Al^{3+}, $10^{-0.81}$ M Mg^{2+}, $10^{-0.80}$ M Na^+, and pH 3.1. The high activities of Al^{3+} in the 5% HIS solution should lead to displacement of all other cations, including Mg^{2+}, from the interlayers resulting in binding of Al^{3+} on the remaining negatively charges sites. The large hydrated radius of Mg^{2+} and the known strong bonds between smectite interlayers and polymeric hydroxy-Al species suggest that the interlayer Al-hydoxy species should predominate [99] and potentially counteract the shrink-swell tendencies of smectite.

With the addition of concentrated HIS to the smectite system, Visual MINTEQ predicts complete dissolution of smectite with 6.0 M SiO_2(am)as the only solid phase. Cationic activities become very high: $10^{0.23}$ M Na^+, $10^{2.77}$ M for Al^{3+}, $10^{1.04}$ M Mg^{2+}, and pH -1.6. It should be noted that although the thermodynamic activity of Al^{3+} is in the hundreds, the concentration of the Al^{3+}
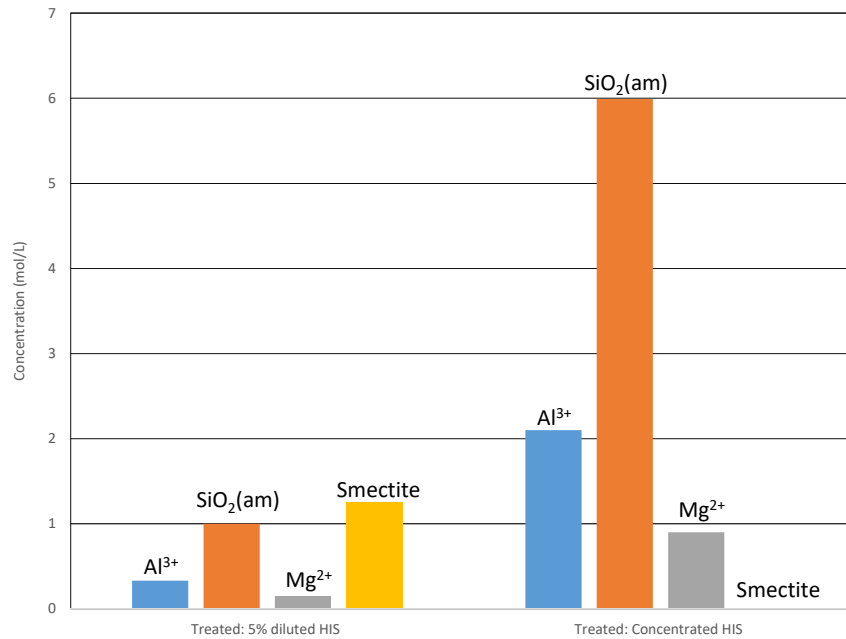
Figure 4.4: Effect of HIS on the concentration of Al^{3+}, $SiO_2(am)$, Mg^{2+} and Smectite. "Reprinted with permission from ASCE: Journal of Materials in Civil Engineering".

is a more reasonable $10^{0.32}$. The activity coefficient for the trivalent cation is very small due to the high ionic strength of the HIS solution, resulting in a very high Al^{3+} activity when calculated from the concentration. These results are in general agreement with the observations of Tomic [98].

To illustrate the solid phases transitions in response to HIS additions, phase diagrams were constructed (Figure 4.5-4.7) using Geochemist's Workbench. Activities of the solution species from Table 4.3 were used as input as well as the speciation potential of solid phases, and Geochemist's Workbench constructed the diagrams. The phase stability diagram for the untreated case is seen Figure 4.5. Phase diagrams for 5% diluted HIS and concentrated HIS treatments are shown in Figure 4.6 and Figure 4.7, respectively. In the untreated case, the locus of the equilibrium point A

Table 4.3: Calculated activities of phase components of treated and untreated smectite

Component (1)	log(activity)		
	Untreated (2)	5% diluted HIS (3)	Concentrated HIS (4)
Al^{3+}	-15.73	-0.46	2.74
$H_4SiO_4(aq)$	-4.25	-2.76	-3.38
Mg^{2+}	-5.07	-0.81	1.04
Na^+	-5.06	-0.81	0.22

Table 4.4: Calculated equilibrium concentration for untreated and HIS treated smectite

Phase (1)	Untreated (mol/L) (2)	5% diluted HIS (mol/L) (3)	Concentrated HIS (mol/L) (4)
$Smectite$	1.50	1.25	0.00
$Al(OH)_3(am)$	0.00	0.00	0.00
$SiO_2(am)$	0.00	1.01	6.00

is in the region of smectite. This indicates that smectite is stable in the untreated case. In the 5% diluted HIS treatment, the locus of the point, B is at the phase boundary of smectite, SiO_2(am), Al^{3+}, and H_4SiO_4(aq) indicating stability of the phases. The stability of smectite was validated by the X-Ray diffractogram peaks and the release of SiO_2(am) and Al^{3+} were observed in FTIR (discussed in following sections). The modeling also showed release of Al^{3+} and SiO_2(am) by the partial dissolution of smectite. This indicates that Al^{3+} will be released from the octahedral sheets and has the potential to react with net negative surface charges thereby reducing the shrink-swell characteristics of the clay. Figure 4.7 shows that the locus of the equilibrium point C is in the region of Al^{3+} and H_4SiO_4(aq) for the concentrated HIS treatment. This shows complete dissolution of smectite and subsequent release of Al^{3+} and H_4SiO_4(aq) from the octahedral and tetrahedral layers, respectively. This is validated by the X-Ray diffractogram (Figure 4.9 and Figure 4.10). Tomic [98] treated bentonite with a range of sulfuric concentrations at 60^oC for 2 hours to determine the impact of acid activation on a range of properties. As with this project, Tomic found that partial dissolution of smectite with the release of Al^{3+} and SiO_2(am) was observed up to 3 M acid with the high cation exchange capacity (CEC) remaining intact. Higher concentrations (up to 6 M sulfuric
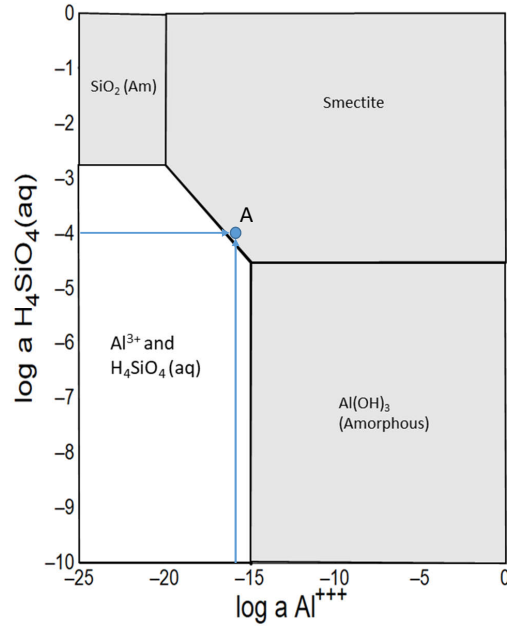
Figure 4.5: Phase diagram for untreated smectite, drawn with the following conditions: $T=25^0C$, P=1atm, pH = 8.5, Na$^+$ activity $10^{-5.06}$, Mg^{2+} activity $10^{-5.07}$. "Reprinted with permission from ASCE: Journal of Materials in Civil Engineering".

acid) decreased the CEC, increased SiO_2(am) content, and degraded the structure of the smectite. Steudel [100] made similar observations using different clays, acids, and digestion temperatures.

Hydroxy interlayer compounds such as $Al(OH)_3$(am) can form in an interlayer among repeating smectite unit cells. Table 4.4 lists the equilibrium concentrations for untreated and treated smectite including $Al(OH)_3$(am). In the 5% diluted HIS treated and concentrated HIS treated treatments, precipitation of $Al(OH)_3$(am) is not favored thermodynamically. The transformation process and its effect on swell characteristics was not investigated.

Figure 4.8 shows the increase in concentration of Al^{3+} and SiO_2(am) with increasing HIS con-
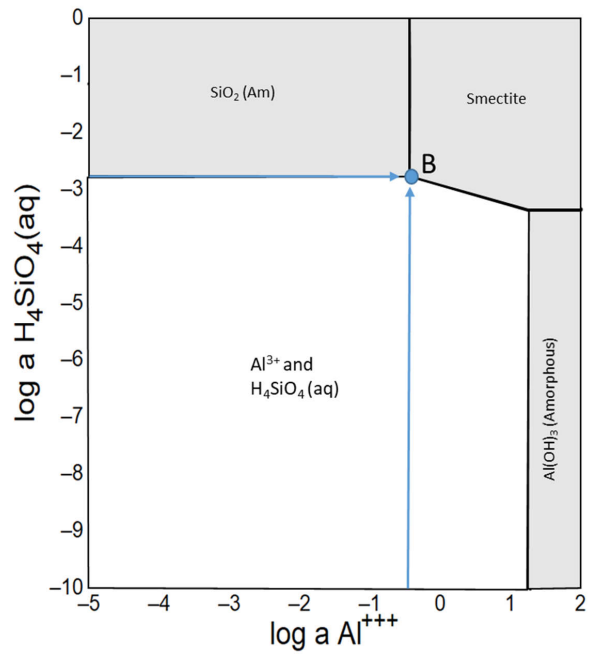
Figure 4.6: Phase diagram for smectite treated 5% HIS, drawn with the following conditions: T=25^0C, P=1 atm, pH = 3.1, Na^+ activity $10^{-0.8}$, Mg^{2+} activity $10^{-0.8}$. "Reprinted with permission from ASCE: Journal of Materials in Civil Engineering".
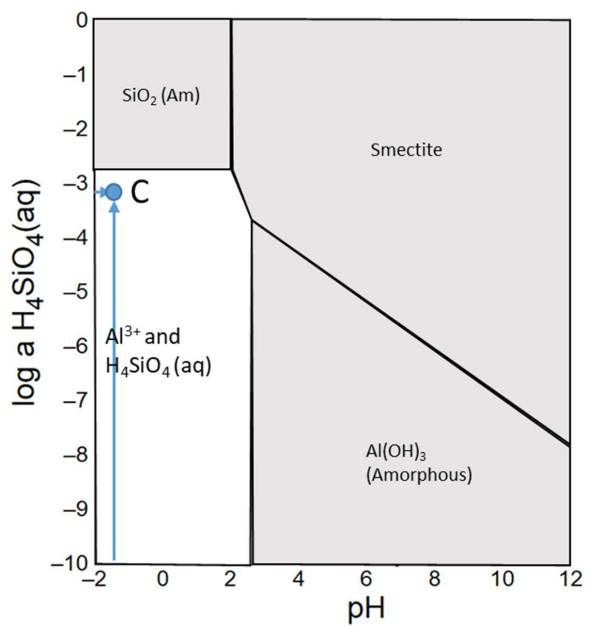
Figure 4.7: Phase diagram for smectite treated 5% HIS, drawn with the following conditions: T=25^0C, P=1atm, pH = -1.5, Na$^+$ activity $10^{0.2}$, Mg^{2+} activity $10^{1.0}$. "Reprinted with permission from ASCE: Journal of Materials in Civil Engineering".
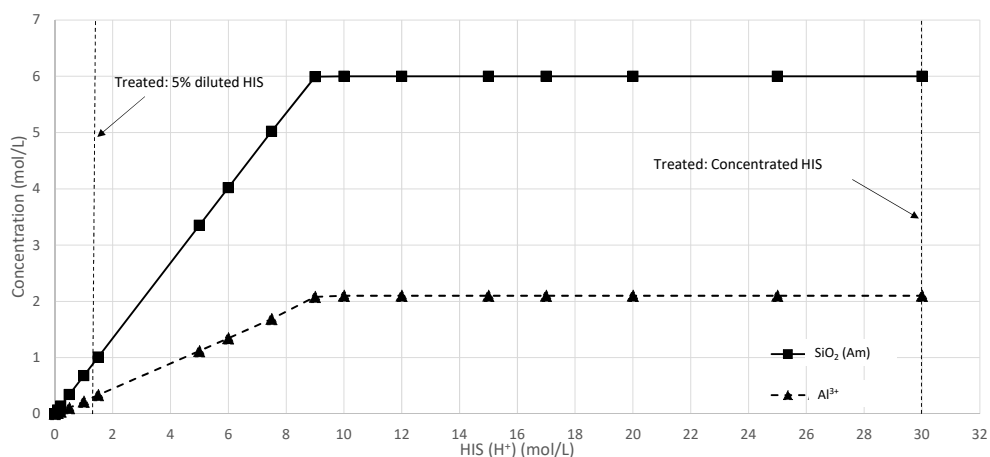
Figure 4.8: Calculated concentrations using Visual MINTEQ of soluble Al^{3+} and SiO_2(am) for treated smectite. "Reprinted with permission from ASCE: Journal of Materials in Civil Engineering".

centration. At 1.5 mol/L of HIS (5% diluted HIS), there is an increase in free SiO_2(am) and Al^{3+}. This indicates partial dissolution of smectite. The complete dissolution of smectite with the release of 6.0 mol/L of SiO_2(am) and 2.1 mol/L of Al^{3+} is predicted for HIS concentrations ranging from 10 to 30 mol/L. As previously stated, we hypothesize that at HIS concentrations up to 10 mol/L, the combined effect of the release of Al^{3+} ions from the octahedral layer (adsorption of Al^{3+} on the negative surface) and SiO_2(am) from the tetrahedral layer (structural distress affecting the net negative charge and surface area) reduces the shrink-swell behavior of smectite.

4.4.2 X-Ray Diffraction Analysis

The X-Ray diffractograms for untreated and treated smectite at 30% RH are shown in Figure 4.9 and, diffractograms at 95% RH are shown in Figure 4.10. Expansive clay minerals like smectite, show a change in peak angle (2θ) when the RH changes. As the smectite expands with increase in RH, the d-spacing increases and the 2θ value decreases. This behavior was used to identify smectite. The crystallography open database (COD) has a repository of X-Ray diffraction patterns for known minerals [101]. The COD data shows that quartz crystal will have a peak at $26.7°$ as seen in the XRD diffractogram (Figure 2).

At 30% RH a smectite peak is registered at 2θ $7.6°$, but at 95% RH, the smectite peaks occur at 2θ $5.6°$ and $6.6°$ for untreated and 5% diluted HIS treated smectite, respectively. Smectite treated with concentrated HIS did not display any significant peak due to the dissolution of smectite. Amorphous materials do not exhibit sharp peaks as they do not possess long range order, but exhibit broad humps like at 2θ $29°$ for treated smectite (Point (A) in Figure 4.9 and Figure 4.10), which corresponds to the presence of amorphous SiO_2 [102].

The control of relative humidity helped in the quantitative comparison of d-spacing between the treated and untreated smectite samples. At 30% RH, there is no significant difference in d-spacing between untreated and smectite treated with 5% diluted HIS. This is due to the presence of less water among the smectite crystals. At 95% RH, the d-spacing is smaller in the smectite treated with 5% HIS (13.3Å) compared to untreated sample (15.5Å), illustrating the reduction in swell potential for the treated smectite. In addition, significant distress due to structural changes in the clay lattice is recorded by the widening of the diffraction response in the vicinity of about 15.5Å. A new peak at $12.2°$ is registered for treated sample. This peak corresponds to gypsum ($CaSO_4 \cdot 2\,H_2O$), and it indicates interaction of HIS with smectite's interlayer Ca^{2+} cations. Therefore, the decrease in swelling at high RH, indicated by the reduced d-spacing, is the result of the structural changes induced by the 5% HIS and the interaction of HIS with the interlayer cations.
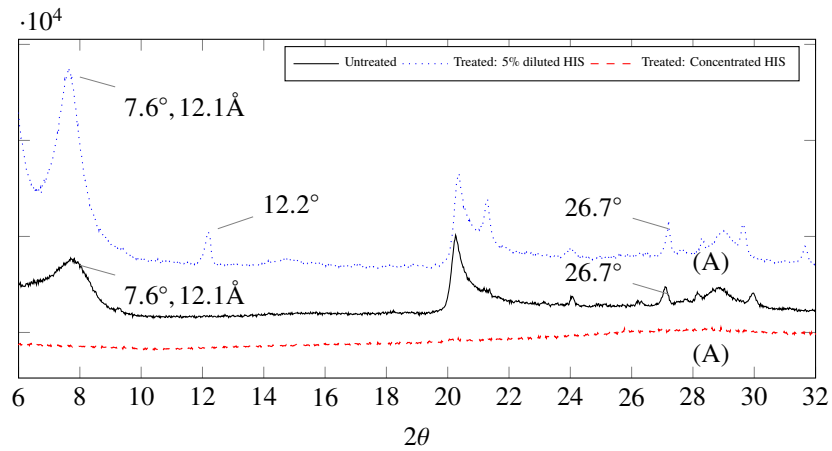
Figure 4.9: X-Ray Diffractogram of treated and untreated smectite at RH 30. "Reprinted with permission from ASCE: Journal of Materials in Civil Engineering".
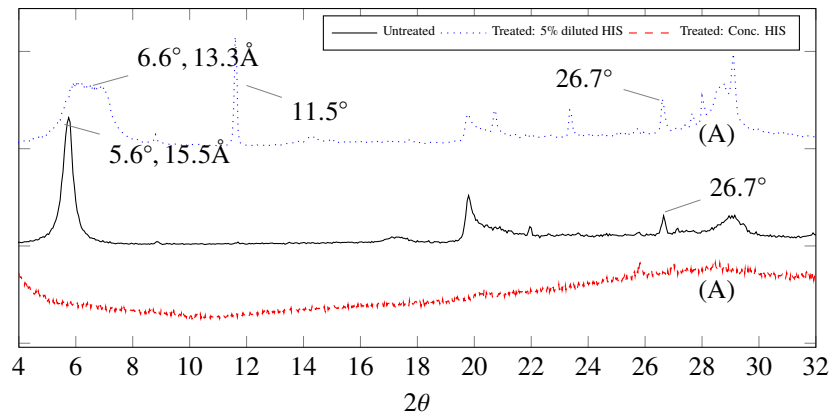
Figure 4.10: X-Ray Diffractogram of treated and untreated smectite at RH 95. "Reprinted with permission from ASCE: Journal of Materials in Civil Engineering".

4.4.3 FTIR Analysis

The FTIR transmission spectra of smectite treated with concentrated and 5% diluted HIS are shown in Figure 4.11. Table 4.5 assigns FTIR transmittance band positions to functional groups such as Al-Al-OH and Si-O present in the octahedral and tetrahedral sheets of smectite. The transmittance regions of primary interest in the FTIR spectra lie between 914-1116 cm^{-1} for effects related to Si in the tetrahedral layer and Al in the octahedral layer. Smectite treated with concentrated HIS produced two new bands at 1144 and 1094 cm^{-1} that correspond to Si-O vibrations from the amorphous silica and stretching of Si-O, respectively [103]. The reduction in intensity of transmittance indicates an increase in amorphous Si in both the treated samples. In addition, the shape and depth of the band at 1115-1117 cm^{-1} are less pronounced for the treated smectite when compared to the untreated samples. Treated smectite demonstrates deformation of OH linked to Al^{3+} [104]. The percent transmission at band 918 cm^{-1} is higher for the smectite treated with 5% diluted HIS when compared to untreated smectite. Additional bands at 3625 and 914 cm^{-1} correspond to smectite structural OH groups, which are primarily used to identify smectite [105]) and quartz. Thus FTIR spectra demonstrates that addition of HIS changes the tetrahedral Si and octahedral Al in smectite.
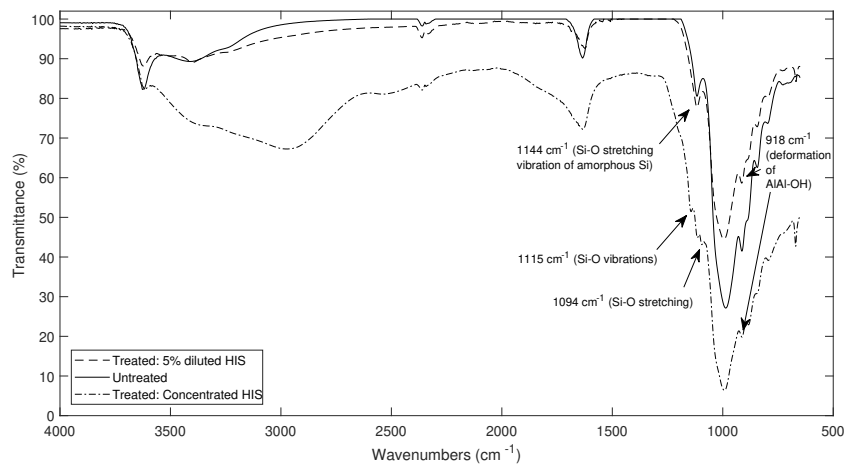
Figure 4.11: FTIR bands for treated and untreated smectite. "Reprinted with permission from ASCE: Journal of Materials in Civil Engineering".

Table 4.5: Assignments of absorption maxima in IR spectra of smectite

Band Position (cm^{-1})	Assignment
(1)	(2)
3622	Smectite OH group
1624	OH stretching of H_2O
1144	Si-O stretching vibrations of Amorphous Si
1115	Si-O stretching
1094	Si-O stretching
918	deformation of $Al - Al - OH$
838	Al-Mg-OH (Smectite)
994	Si-O (Quartz)

4.4.4 One dimensional cyclic swell test

The one-dimensional swell test measures the effect of HIS on volumetric stability. Figure 4.12 shows the variation of swell for untreated and treated (5% dilute HIS) smectite. Three cycles of swell were measured for the treated and untreated smectite. The drying induced shrinkage cracks increased the permeability of the smectite and subsequently caused increased swell in the presence of moisture. The second swell cycle recorded a maximum swell of 7.5 mm. The samples were dried for a period of 24 hours to achieve similar moisture contents between swell cycles. A swell reduction from 4.5 mm for untreated to 2.5 mm for treated smectite was recorded in the third swell cycle. This may be due to the further diffusion of HIS through the shrinkage cracks in smectite. Thus, three cycles of the swell test demonstrated less swell for the treated smectite when compared to the untreated smectite. Treated smectite recorded 37%, 16% and 46% reduced swell in the first, second and third swell cycle, respectively. The results are consistent with the hypothesis that the combined effect of released Al^{3+} (from the octahedral sheet) interacting with negative surface charge and structural change by the release of SiO_2 (from the tetrahedral sheet) in the smectite crystal result in a substantial reduction in volumetric instability.
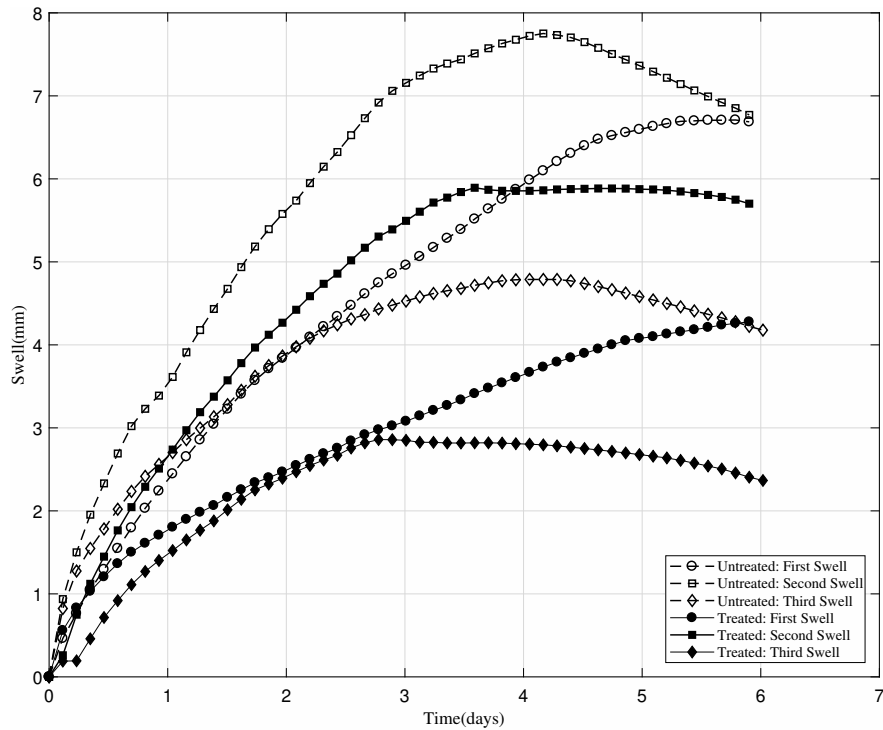
Figure 4.12: One dimensional cyclic swell test of 5% HIS treated and untreated smectite. "Reprinted with permission from ASCE: Journal of Materials in Civil Engineering".

4.5 Summary and Conclusion

We used a Gibb's free energy minimization thermodynamic model to simulate the stabilization mechanism for smectite treated with HIS and validated this experimentally. The thermodynamic model showed the release of Al^{3+} from the octahedral sheet and SiO_2 from the tetrahedral sheet for smectite treated with HIS. The release of Al^{3+} and SiO_2 increased with increasing concentration of HIS added to smectite. Prior to the addition of HIS, smectite was the only thermodynamically stable phase with little dissolution, but after addition of HIS the release of Al^{3+} and SiO_2 were thermodynamically favored due to the dissolution of smectite. The released Al^{3+} may satisfy the residual negative charge at the colloid surface as the ions are coulombically attracted to the clay surface; these adsorbed ions also significantly reduce the potential to sorb water. Solubilization of SiO_2 from the tetrahedral sheet caused additional structural change of the smectite, further influencing swell potential. The structural changes indicated by the model were validated using XRD

and FTIR, and volumetric stabilization was validated using cyclic swell testing. X-Ray diffractograms showed a reduction in d-spacing for the 5% HIS-treated smectite at 95% RH compared to untreated smectite. This is consistent with less swelling observed in physical swell tests. Widening of the smectite peak also was consistent with distress in smectite due to structural changes. The X-Ray diffractogram of the treated concentrated HIS (Figure 9 and 10) does not have a smectite peak. This indicates dissolution of the smectite as indicated by the model. FTIR data detected an increase in amorphous Al-Al-OH and Si-O for treated smectite. When concentrated HIS was added to smectite, a significant increase in amorphous Si-O was found. This should be associated with the increase in concentration of SiO_2(am) and Al^{3+} as calculated by the model (Figure 4). Sorption of Al^{3+} resulted in reduced swelling in the cyclic one dimensional swell test. The release of substantial Al^{3+} and SiO_2(am) requires very high concentrations of HIS (low pH), less than about 5% added water. Addition of large quantities of HIS may not be a pragmatic solution in the field but simulation of stabilization using thermodynamic models will enable us to understand the effect of chemical stabilization on the physico-chemical characteristics of expansive clay. It is possible that the "build-up" of H^+ ions due to the multiple treatments of moderate HIS concentrations may be an effective approach. This should be the next step in this research. In addition to the change in engineering properties, it is critical to understand the mineralogical changes. The study shows the possibility of using thermodynamic models to investigate stabilization mechanisms of chemical stabilizers (e.g. HIS). This approach can also be used to assess whether significant quantities of desired minerals will form and whether significant quantities of undesirable products will form, such as the expansive mineral, ettringite.

48

5. COUPLED THERMODYNAMIC AND EXPERIMENTAL APPROACH TO EVALUATE ETTRINGITE FORMATION IN A SOIL STABILIZED WITH FLUIDIZED BED ASH BY-PRODUCT: A CASE STUDY[*]

5.1 Introduction

Pozzolanic materials have been used extensively in chemical soil stabilization of soft clays due to their effectiveness in improving strength and stiffness [3, 106, 107, 108, 109]. Recent studies in chemical soil stabilization have also used geopolymers [110, 111, 112], phophogypsum [113] and eco-friendly binders [114] to improve the mechanical properties. Clay itself is a pozzolan. A strength enhancing, pozzolanic reaction is triggered by combining an alkaline earth material such as lime (calcium hydroxide) with the pozzolan-bearing soil. The high pH environment provided when lime dissolves in water releases pozzolans silica and alumina from the clay to react with calcium from lime and water to form calcium-silicate-hydrates (CSH), calcium-aluminate-hydrates (CAH) and, calcium aluminium silicate hydrates (CASH) [115]. However, some clays and virtually all non-clay soils do not provide sufficient pozzolans to produce required strength. In this case fly ash, a pozzolan or other forms of coal combustion by products (CCBPs), are often blended with lime to provide the required constituents. Portland cement, which releases a considerable amount of free lime upon hydration, can trigger pozzolanic reactions with clay, fly ash or other CCBPs.

Most CCBPs are primarily composed of SiO_2, CaO, and Al_2O_3. Secondary constituents can include sulfate SO_4^{2-} in the form of gypsum $CaSO_4 \cdot 2\,H_2O$ [116, 117]. The sulfate ions from gypsum can react with the Ca^{2+} ions from CaO and Al^{3+} ions from Al_2O_3 in the presence of water to form ettringite $(Ca_6Al_2(SO_4)_3(OH)12 \cdot 26\,H_2O)$. It can precipitate in an environment with high sulfate activity and pH [69]. In soils, ettringite can form when a calcium based stabilizer with high sulfate activity such as fluidized bed ash, is added [7, 118, 119, 71]. Ettringite in the form of micron-sized fibrous crystals can damage densely compacted, soils stabilized with lime and

CCBPs or cement though expansion [10, 71, 120, 121, 11]. A secondary mineral, thaumasite, may also precipitate through the isostructural transformation of ettringite. Thaumasite formation results in loss of strength and is usually preceded by the formation of ettringite [122].

Whether or not ettringite will form in lime-fly ash stabilized soils is normally estimated based on the quantity of water soluble sulfates present in the native soils to be treated [9]. However, this empirical assessment does not always hold valid as in some cases ettringite has been detected in soils with less than 1,000 ppm water soluble sulfates and in other cases no significant ettringite formation was detected in soils with over 10,000 ppm water soluble sulfate [5, 10, 11]. Several other factors such as the overall mineralogical composition of the soil and the availability of proper stoichiometric quantities of all constituents, especially water, have proven to be a key to the formation of ettringite [12, 8]. The formation of ettringite has been studied using numerical modeling [13, 14] and molecular dynamics Studies have investigated the formation of ettringite using numerical modeling and molecular dynamics [15, 16].

5.1.1 Thermodynamic modeling

Thermodynamic modeling provide a better understanding of the chemical interactions between solid and liquid phases of hydration [123, 124, 125, 126, 127]. These models are able to predict whether a reaction can take place and calculate the equilibrium composition. In this study, a thermodynamic model was constructed with the geochemical speciation code GEMS-PSI [128, 93, 129] populated by the thermodynamic databases PSI-Nagra and CEMDATA14 [130, 131, 132]. The accuracy of the prediction is dependent on characterization of the material. Therefore, hydration is modeled based on the compositional analysis from X-Ray Fluorescence (XRF) and X-Ray Diffraction (XRD). Analytical characterization methods including XRD and XRF provide sufficient information about the geochemistry of the material. The CaO and SO_3 oxide composition obtained using XRF was used to stoichiometrically calculate the quantity of gypsum in the sample (Refer to section 4.2 for additional information). The calculation assumes gypsum as the source of sulfate. The input for the thermodynamic model comprised the mineral gypsum and other oxides: Na_2O, K_2O, MgO, Fe_2O_3, SiO_2, and Al_2O_3. The available mineralogical data for the blended ma-

50

terial was limited to only ettringite. If the complete quantitative mineralogical data of the blended material was available, it would have improved the accuracy of our thermodynamic model. Therefore, the model proposed in this study can be used as a forensic tool to investigate the potential to form ettringite. The addition of minerals in the blended material would have introduced additional thermodynamic data such as solubility product ($logK_{sp}$) [133, 27] that would have constrained the solubility of minerals and increased the quantitative accuracy of the model. Al_2O_3 was used as the source of alumina in the model. In the actual soil, alumina could have been in the form of gibbsite, kaolinite or both. The $logK_{sp}$ values of gibbsite, kaolinite and Al_2O_3 are significantly different and therefore would affect the quantity of ettringite that can form at equilibrium. This would contribute to some deviation in the quantitative prediction of ettringite.

Phase diagrams are excellent tools to visualize stability of minerals such as ettringite. Little et. al. [5] demonstrated the use of phase stability diagrams to predict ettringite formation in lime treated soils with high soluble sulfate content. In this study, phase diagrams were constructed to investigate the effect of amorphous silica on ettringite precipitation. The equilibrium activities of phases from the thermodynamic model, GEMS, were used to develop the phase stability diagrams. Geochemist's Workbench was used as a tool in this paper to develop the phase stability diagrams. The stability diagrams showed that with an increase in amorphous silica there was a significant reduction in the stable area of ettringite.

5.2 Background

This case study comprises a shopping center that encompasses approximately 85 acres. The center consists of strip center storefronts and individual buildings. During the construction of the shopping center, fill material was placed to bring the site to grade. The fill material was blended with the fluidized bed ash ("ash") referred to as a hydrated aggregate base material. The depth of fill ranged from 2 to 6 feet. The proposed stabilization was to mix the in-situ soil with 6% ash to a depth of 6 feet. Two years after construction severe structural distress was observed at difference locations of the building as seen in Figure 5.1. The ash was contained very high (30-70%) quantity of gypsum (Table 5.1) indicating ettringite induced heave (sulfate attack) as a possible cause for

51

<center>(a)　　　　　　　　　　(b)</center>
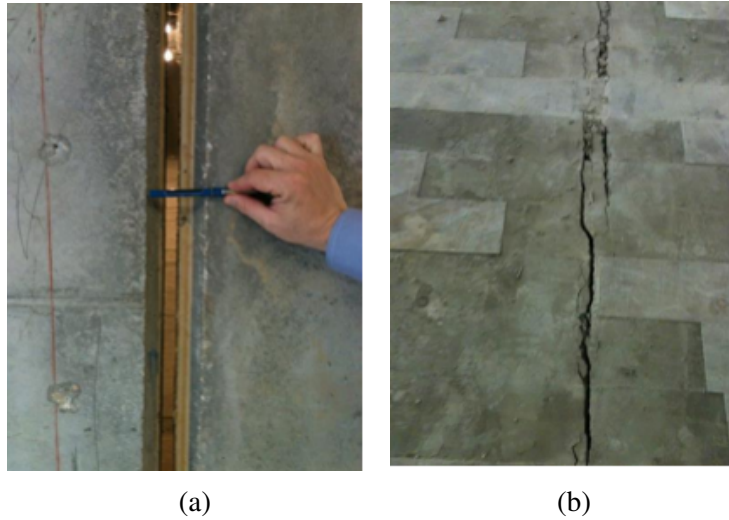
Figure 5.1: Observed Structural distress in the building (a) dislocation on wall (b) cracks on Floor. "Reprinted with permission from Elsevier".

<center>Table 5.1: Fluidized bed ash mineralogy analysis</center>

Common name	Chemical formula	Percent composition (%)
Gypsum	$CaSO_4 \cdot 2\,H_2O$	$43-70$
Hydrated lime	$Ca(OH)_2$	$20-30$
Calcite	$CaCO_3$	$4-22$
Magnesium Hydroxide	$Mg(OH)_2$	$1.7-2.5$
Quartz	SiO_2	< 2.5
Magnesium Oxide	MgO	< 1
Lime	CaO	< 1
Free moisture	H_2O	$5-10$

the distress. Therefore, blended samples containing fill and ash were collected from three sites (Site X, site Y and site Z) inside the center for physical and chemical characterization. Chemical testing including pH, XRF, XRD (semi quantitative ettringite and thaumasite detection) and water soluble sulfate test were performed on all samples. Physical tests included Atterberg limits and grain size distribution.

5.3   Methods

Samples were collected at locations where structural distress was observed. Characterization of the material through physical and chemical testing followed the methodology in Figure 5.2.
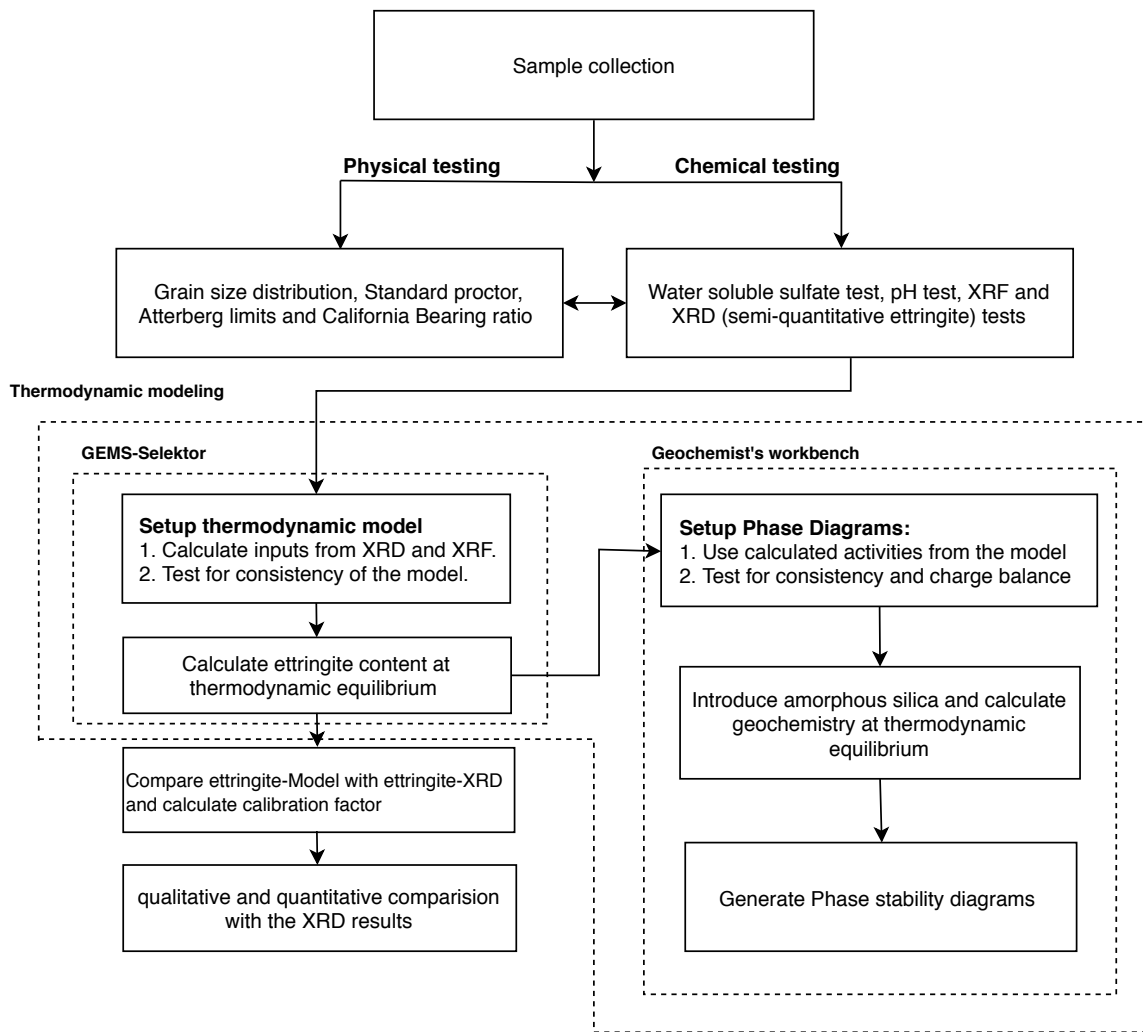
Figure 5.2: Methdology flowchart. "Reprinted with permission from Elsevier".

5.3.1   Physical and chemical testing

A total of 45 samples from 18 boreholes were obtained for physical and chemical analysis. Auger boring and field sampling were performed in accordance with ASTM D 1452-09 [134].

Physical testing included California Bearing Ratio [135], Atterberg limits [136], standard Proctor [137] and grain size distribution [138]. Chemical testing included pH tests, X-Ray Fluorescence (XRF) [139] and X-ray Diffraction (XRD) for a semi-quantitative determination of the presence of ettringite/thaumasite [140].

5.3.2   Thermodynamic modeling

The thermodynamic modeling program GEMS-PSI with the thermodynamic databases PSI-Nagra and CEMDATA14 was used to evaluate ettringite formation potential. Input data for the model included the oxide content from the XRF data and calculated mineralogical data. The stoichiometric oxide composition of CaO, SO_3, and H_2O in gypsum is 32.6%, 46.5% and 20.9%, respectively. Therefore, the CaO and SO_3 content can be used to back calculate the amount of gypsum present in the sample (assuming enough H_2O is present). For example, Sample ID B1/S1 has a CaO and SO_3 content of 18.8% and 18.9%, respectively. The 18.9% SO_3 (from XRF data) will stoichiometrically form 40.87% gypsum ($\frac{18.89}{46.5} * 100 = 40.87\%$). The CaO present in the calculated gypsum can then be deducted from the total CaO composition ($18.9 - (\frac{32.6}{100} * 40.87) = 5.71\%$). This CaO is referred to as "remaining CaO" (Table 5.2). Thus, gypsum, remaining CaO, MgO, SiO_2, Al_2O_3, Fe_2O_3, Na_2O, MgO and K_2O were used in the thermodynamic model. Gypsum calculated using this method was also consistent with the mineralogy of fly ash in Table 5.1 (The calculated gypsum does not exceed the maximum gypsum present in the fly ash). Semi-quantitative XRD analysis was only used for ettringite quantification and not to investigate the formation of other minerals. The CaO and SO_3 content from XRF were used to calculate the quantity of gypsum in the sample.

In addition to calculating the quantities of products at equilibrium, GEMS also calculates the activities of phases. Activity is related to the concentration by the relationship.

$$(a) = \gamma[C] \tag{5.1}$$

where, $[C]$ is the concentration, γ is the single ion activity coefficient and (a) is the activity of the phase. The value of γ is dependent on the ionic strength, charge of the ions and diameter of the ions. Geochemist's Workbench requires the activities of phases to construct the phase stability diagram. The calculated equilibrium activities from GEMS-PIS were used to construct the phase stability diagrams. In addition to ettringite, soil minerals kaolinite, montmorillonite and selected hydration products from database Thermoddem and CEMDATA14 were also considered in the phase stability diagram.

5.4 Model Calibration

The model calculated the quantity of ettringite at thermodynamic equilibrium but the blended material may not have reached equilibrium at the time of testing. Therefore, a calibration constant of 0.5, which is approximately the ratio described of Ettringite-XRD(%)/ Ettringite-Model(%), was introduced. For example when 20% ettringite was calculated by the model, the calibration factor reduced the calculated ettringite to 10% (20% x 0.5 = 10%). The calibration constant was applied to all samples.

Table 5.2: Summary of Thermodynamic modeling and chemical laboratory results

Site	Sample ID	pH	Soluble sulfate (ppm)	Ettringite - XRD (%)	Geochemical composition (%)									Thermodynamic modeling	
					SiO2*	Al2O3*	CaO	MgO*	Fe2O3*	SO3	Na2O*	K2O*	Gypsum*	Ettringite (%)	Qualitative Match
X	B1/S1	11	0	25.5	49.3	7.84	18.9	0.73	2.94	18.8	0.2	0.31	40.87	25.0	Yes
	B1/S2	10.6	1634	7.4	65.1	10.7	10.2	0.53	2.95	8.74	0.2	0.39	19.00	11.0	Yes
	B1/S4	9.9	0	<1	81.7	8.15	3.41	0.33	2.12	2.70	0	0.29	5.97	4.0	No
	B2/S1	11.3	12	19	52.2	7.85	20.5	0.61	3.03	14.3	0	0.35	31.09	24.0	Yes
	B2/S2	10.7	1691	14.7	64.9	11.4	9.96	0.53	3.24	8.28	0	0.38	18.00	11.0	Yes
	B2/S4	9.9	1575	8.7	75.6	7.65	6.88	0.44	2.11	5.72	0	0.3	12.43	5.5	Yes
	B3/S1	11.9	4725	20.4	48.5	7.99	20.6	0.74	2.87	17.7	0	0.32	38.48	15.0	Yes
	B3/S3	10	0	<1	76.9	8.76	4.86	0.25	2.97	4.62	0	0.34	10.04	2.0	No
	B3/S5	8.1	559	1	84.1	9.57	0.55	0.22	3.32	0.57	0	0.32	1.24	0.0	Yes
	B4/S1	10.8	1752	23.6	53.6	8.21	17.9	0.56	2.95	15.2	0	0.34	33.04	25.0	Yes
	B4/S3	10.8	8	15.3	59.1	9.88	13	0.52	2.96	13.0	0	0.35	15.00	16.0	Yes
	B4/S5	3.8	298	<1	88.3	8.14	0.12	0.26	1.38	0.16	0	0.3	0.00	0.0	Yes
	B5/S1	11.0	0	14.9	55.3	8.21	16.3	0.2	2.82	15.3	0	0.31	33.26	11.0	Yes
	B5/S5	8.1		<11	85.1	8.72	0.27	0.31	3.72	0.31	0	0.30	0.67	0.0	Yes
	B6/S1	10.3	1744	18.2	56.4	8.63	16.7	0.61	3.00	13.1	0	0.33	28.48	22.5	Yes
	B6/S2	10.0	1328	13.1	68.7	12.9	6.95	0.42	3.61	5.74	0	0.43	12.47	6.0	Yes
	B6/S4	8.9	1823	2.8	74.9	8.79	6.29	0.49	2.09	5.99	0	0.31	13.02	4.0	Yes
Y	B7/S3	10.7	1002	8.8	70.6	9.11	8.00	0.40	2.28	8.13	0	0.29	17.60	7.3	Yes
	B7/S5	9.8	1023	1.9	77.3	11.0	3.44	0.36	3.28	3.02	0	0.32	6.51	0.0	No
	B8/S1	10.6	1069	10.4	70.5	9.65	8.58	0.36	2.34	7.14	0	0.37	15.52	9.0	Yes
	B8/S3	10.8	989	22.2	65.7	10.2	10.2	0.42	2.82	9.08	0	0.34	19.70	11.5	Yes
	B8/S5	10.6	955	9.5	70.6	10.6	7.67	0.35	2.79	6.45	0	0.36	14.02	7.5	Yes
	B9/S1	10.8	1837	15	64	9.85	11.7	0.39	2.77	9.68	0	0.38	21.04	15.0	Yes
	B9/S3	10.7	915	8.6	68.7	11.2	8.44	0.45	2.56	7.23	0	0.71	15.71	9.0	Yes
	B9/S5	9.9	0	<1	73.2	18.7	1.88	0.38	2.51	1.30	0	0.33	2.82	9.0	Yes
	B10/S1	11.4	1297	17.1	54.3	7.40	19.5	0.41	2.92	13.6	0	0.31	29.56	27.0	Yes
	B10/S2	12.1	1339	17.2	53.1	7.62	19.4	0.36	2.28	15.6	0	0.35	33.91	25.0	Yes
	B10/S4	11	876	9.9	69.4	9.68	8.97	0.39	2.55	7.49	0	0.33	16.28	10.0	Yes
	B11/S1	10.8	1369	11.2	64.4	9.11	12.4	0.35	2.62	9.48	0	0.34	20.87	16.0	Yes
	B11/S2	11.2	692	22	66.2	9.45	11.0	0.28	2.64	8.69	0	0.29	18.89	16.0	Yes
	B11/S4	10.4	1670	4.8	76.5	10.70	3.88	0.42	3.94	3.23	0	0.29	7.02	0.0	No
	B12/S1	12.3	1236	17.7	48.4	7.36	23.5	0.43	2.35	16.3	0	0.32	35.43	28.0	Yes
	B12/S2	11.7	1413	20.2	56.5	8.14	16.9	0.38	2.30	14.0	0	0.29	30.43	22.5	Yes
	B12/S4	11.7		16.1	59.6	9.24	16.1		2.33	11.6	0		25.21	22.0	Yes
Z	B13/S2	10.7	874	12.7	60.2	17.9	9.48	0.23	3.99	6.87	0	0.33	14.93	4.5	Yes
	B13/S4	11.9	28	28.7	44.7	8.5	23.7	0.48	2.68	18.4	0	0.26	40.00	31.0	Yes
	B14/S1	8.9	1231	<11	68.3	10.6	1.08	0.21	4.23	0.14	0	0.32	0.30	0.0	Yes
	B14/S4	10.7	136	28.6	50.5	24.1	18.4	0.56	3.06	15.1	0	0.31	32.82	24.5	Yes
	B15/S1	9.6	199	<1	68.5	20.7	1.15	0.22	4.52	0.48	0	0.34	1.04	0.0	Yes
	B15/S3	11.7	2055	27.1	40.9	11.2	26.0	0.47	3.43	17.0	0	0.29	36.952	32.0	Yes
	B16/S1	8.9	0	<1	59.9	26.0	10.7	0.28	6.87	0.27	0	0.31	0.58	0.4	Yes
	B16/S3	11.7	317	32.4	45.7	22.0	21.9	0.40	4.2	15.0	0	0.31	32.602	29.0	Yes
	B17/S1	7.4	1302	<1	63.6		0.96	0.23	7.33	0.33	0	0.39	0.71	0.0	Yes
	B18/S1	9.1		<1	65.1		2.79	0.24	6.89	1.80	0	0.33	3.91	0.0	Yes
	B18/S4	11.2		20.3	57.9	9.24	15.5	0.42	2.38	13.0	0	0.30	28.26	20.5	Yes

*Thermodynamic model inputs

5.5   Results and Discussion

5.5.1   Physical properties

The summary of physical properties for the stabilized material at the three sites is shown in Table 5.3. The plasticity index (PI) values show that the stabilized material has a low swell potential [141]. This indicates that the recorded structural distress should be due to the formation of ettringite and not due to the expansion of clay minerals. Gradation indicates that sites Y and X are finer soils than most at site Z. The addition of ash can contribute to the increased fines content. The Unified Soil Classification System (USCS) shows that the stabilized material is categorized as clayey sand (SC), silty sand (SM), and SC-SM for sites X, Y, and Z, respectively. Site X data indicates a gradation that falls between silty and clayey sand (SC-SM). Typical CBR values for soil-lime mixtures are 15-45% [142]. The calculated values fall within this range. The optimum moisture content (OMC) also falls in the acceptable range (13-19%). Higher OMC at sites Y and Z must be due to the increase in the percentage of fines. The gradation, PI, CBR and OMC tests do not show any aberrant data.

Table 5.3: Summary of Physical Laboratory Results

| Location ID | USCS Symbol | Liquid Limit, LL(%) | Plastic Limit, PL (%) | Plasticity Index, PI (%) | Grain Size | | | CBR Value[1] | Compaction | |
					Gravel (%)	Sand (%)	Fines (%)		Max. Dry density (pcf)	Optimum Moisture Content (%)
X	SC	29	20	9	11.3	52.9	35.8	31.6	110.4	16.5
Y	SM	30	25	5	11.6	58.5	29.9	45	104.1	19.3
Z	SC-SM	26	21	5	9.3	75.4	15.3	30	116.2	13.0

[1] - The CBR value was measured on samples remolded at four different moisture contents and using standard Proctor compactive effort. The shown CBR vale is the maximum value at 0.1" deflection.

5.5.2 Analytical testing

XRF analysis of the samples provided the elemental oxide composition of the samples (Table 5.2). The average contents of SiO_2, Al_2O_3, CaO, and SO_3 for sites X, Y and Z are shown in Figure 5.3(a). Site X has the highest SiO_2 content followed by site Y and site Z. Ettringite $(Ca_6Al_2(SO_4)_3(OH)12 \cdot 26\,H_2O)$ is a hydration product that can precipitate in a chemical system containing Ca^{2+}, Al^{3+}, $SO_4{}^{2-}$ ions at high pH [69, 10, 68]. Thus the oxide composition of CaO, Al_2O_3, SO_3 from XRF played a critical role in the thermodynamic model. In addition, SiO_2 influenced the geochemistry of the system. Amorphous SiO_2 is highly reactive and can react with CaO, Al_2O_3 and H_2O to form solid solutions as the result of hydration (e.g., calcium silicate hydrate (CSH) and calcium alumina hydrate (CAH)). This can significantly reduce the concentration of Ca^{2+} and Al^{3+} ions available to form ettringite [143]. A similar trend is seen at site X with the highest SiO_2 content 67% and with the least mean ettringite content. Site Z with the least SiO_2 has the highest mean ettringite content. Additional contributing factors for increase in ettringite content at site Z may be due to the higher CaO and Al_2O_3 content. The mean content of CaO and SO_3 in all the sites fall in the range 10-13%.

Figure 5.3 (a) and 5.3(b) shows most samples contain high SiO_2 content followed by CaO, Al_2O_3, SO_3, respectively. Preliminary XRF results of the samples with and without ettringite formation are shown in Figure 5.3(b). Ettringite (detected with XRD) precipitated in samples with a mean CaO and SO_3 content of 10%. Samples with low CaO, SO_3 and high SiO_2 (Approximately 70%) content did not form ettringite. This may be due to effect of reactive amorphous SiO_2 and stoichiometric deficiency of Ca^{2+} and $SO_4{}^{2-}$ ions. It is evident from the geochemistry that the content of CaO, Al_2O_3, SO_3, SiO_2 and pH play a significant role. The relationship between soluble sulfate and ettringite formation is shown in Figure 5.4(a). Gypsum is a common source of sulfate present in fly ash with a solubility of 2.0–2.5 g/l at 25^0C in water. Gypsum solubilizes in water and releases Ca^{2+} and $SO_4{}^{2-}$ ions. Since the soluble sulfate values in Figure 5.4(a) are less than 3,000 mg/kg, further ettringite precipitation may be insignificant.
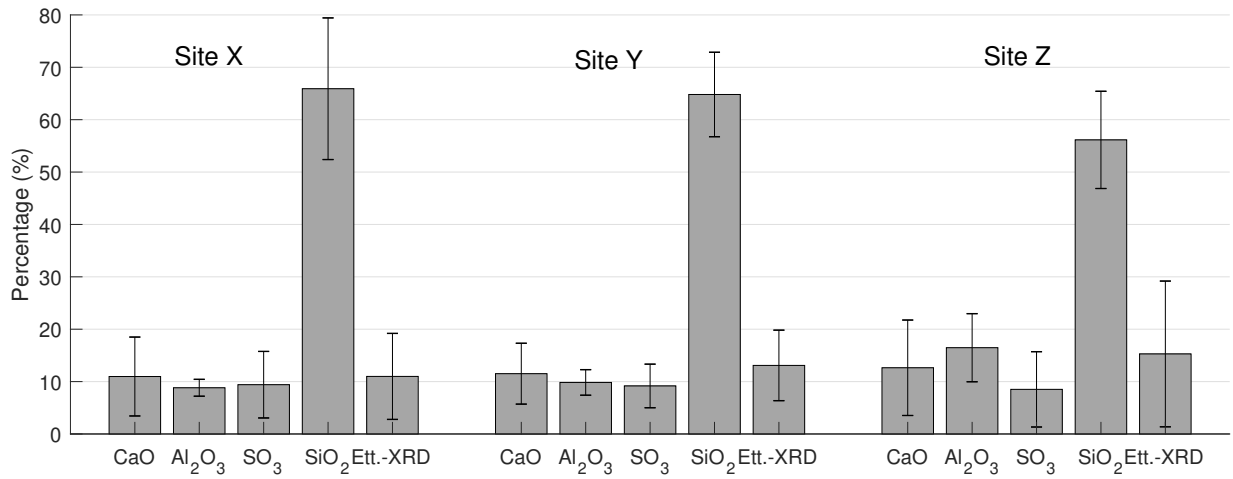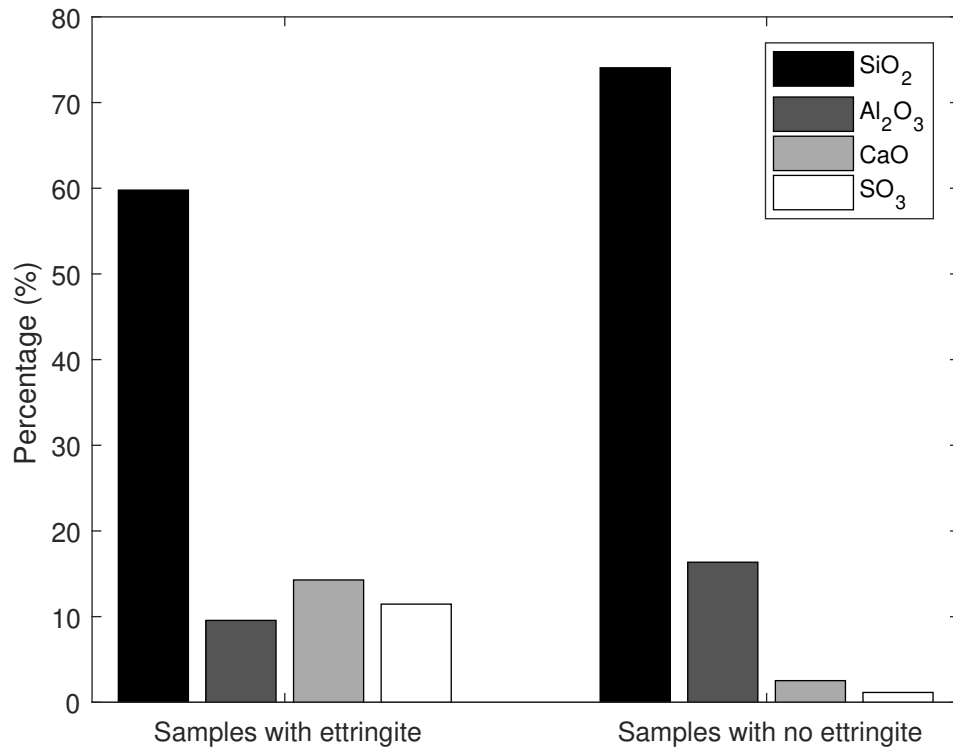
Figure 5.3: Quantitative analysis of CaO, Al$_2$O$_3$, SO$_3$ and SiO$_2$ in the blended material (a) Site X, Y and Z (b) Effect of presence of ettringite on the content of SiO$_2$, Al$_2$O$_3$, CaO and SO$_3$. "Reprinted with permission from Elsevier".

Ettringite requires a pH of between 10 to 12 to remain stable [70]. Figure 5.4(b) indicates a favorable pH range between 10 and 12 for ettringite growth and stability [144]. This shows that the pH of the system is favorable for ettringite formation but there may not be sufficient SO_4^{2-} ions to form significant ettringite.
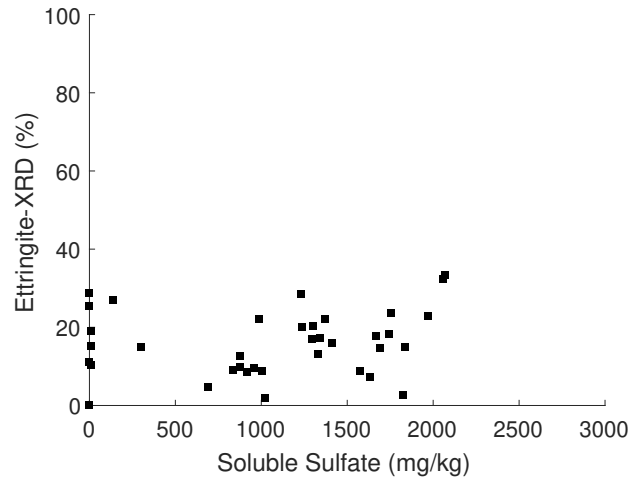
(a) Soluble Sulfate
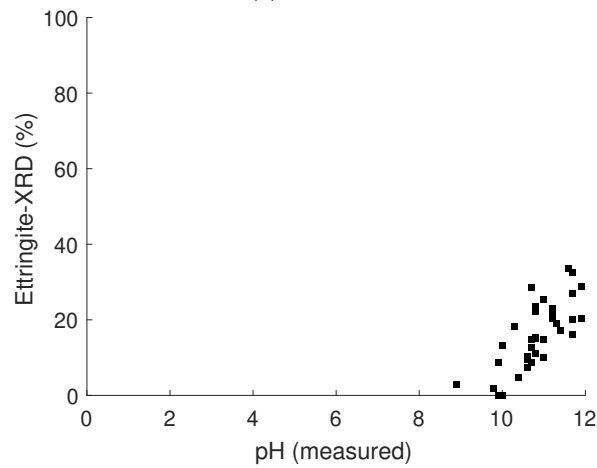
(b) pH (measured)

Figure 5.4: Effect of soluble sulfate and pH (measured). "Reprinted with permission from Elsevier".

Ternary diagram as shown in Figure 5.5(a) show the content of CaO, Al_2O_3, and SiO_2 present in the stabilized material. Point A shows that the selected sample has 11% CaO, 21% Al_2O_3 and 67% SO_3. Most of the samples contain approximately 11% Al_2O_3. The CaO and SiO_2 contents vary from 0-35% and 57-93%, respectively. The agglomeration of data points at the left bottom (SiO_2 rich and CaO deficit) region of the ternary diagram indicates consistent geochemical composition. A surface plot consisting of SO_3 and ettringite quantified by XRD was overlaid on the ternary diagram to study the effect of SO_3 on ettringite formation (Figure 5.5(b) and 5.5(c)), respectively. Concentrations of SO_3 are high in the region where CaO concentration is high. The SO_3 and CaO contents in this regions are also similar (Approximately 20% each).
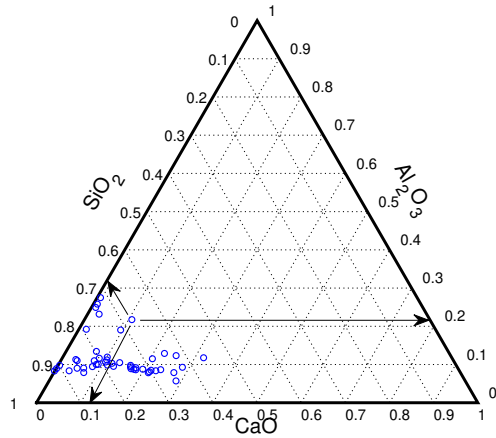
(a)
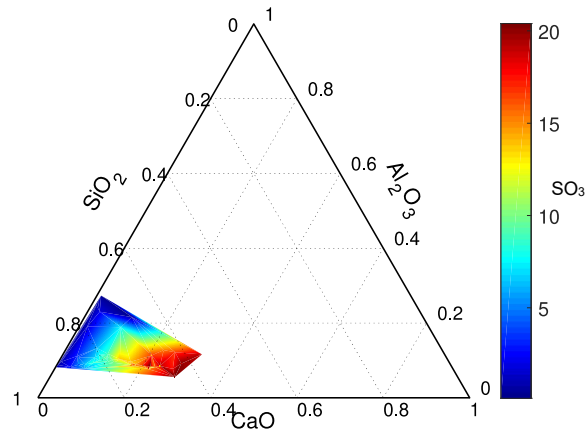
(b)
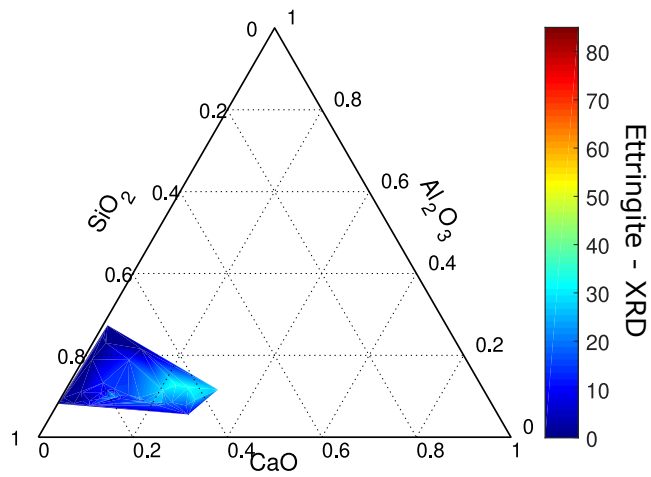
(c)

Figure 5.5: Composition of the stabilized material: Ternary diagram (a) CaO, Al_2O_3, and SiO_2 ternary diagram (b) Overlaid SO_3 (c) Overlaid ettringite-XRD. "Reprinted with permission from Elsevier".

5.5.3 Thermodynamic modeling

A thermodynamic model for the blended material was applied to evaluate the formation of ettringite in the final product. Figure 5.6(a) compares the amount of ettringite calculated using the thermodynamic model with ettringite-XRD (measured experimentally) for sites X, Y and Z, respectively. The calculated ettringite for the stabilized material ranged from 0% (no ettringite) to 62%. Quantitatively, XRD results for ettringite ranged from 0% (no ettringite) to 35%. Ettringite formation increased as CaO and SO_3 contents increased. Deviation in the modeling results varies from -4% (under prediction) to 38% (over prediction). The data points with deviation greater than 20% are regions with SO_3 and CaO contents greater than 15%. Several factors may have impacted accuracy in these regions. First, the thermodynamic model results were based on standard conditions, 25^oC and 1 atm pressure, in situ or field conditions were affected by seasonal changes in temperature and humidity. Kinetics and solubility of minerals will vary depending on environmental conditions (For example dissolution of gypsum is high at 25^oC and reduces with increase or decrease in temperature). Second, the presence of additional amorphous phases and organic phases for which data were not available could have affected the geochemistry. The thermodynamic model calculated the quantity of ettringite at equilibrium but the samples that showed deviation from ettringite-XRD-measured values, may not have reached equilibrium at the time of testing.
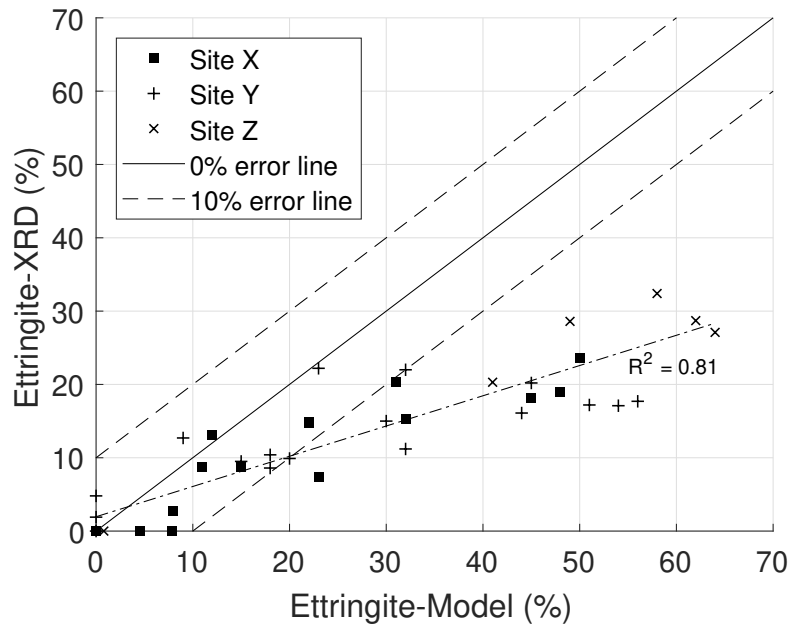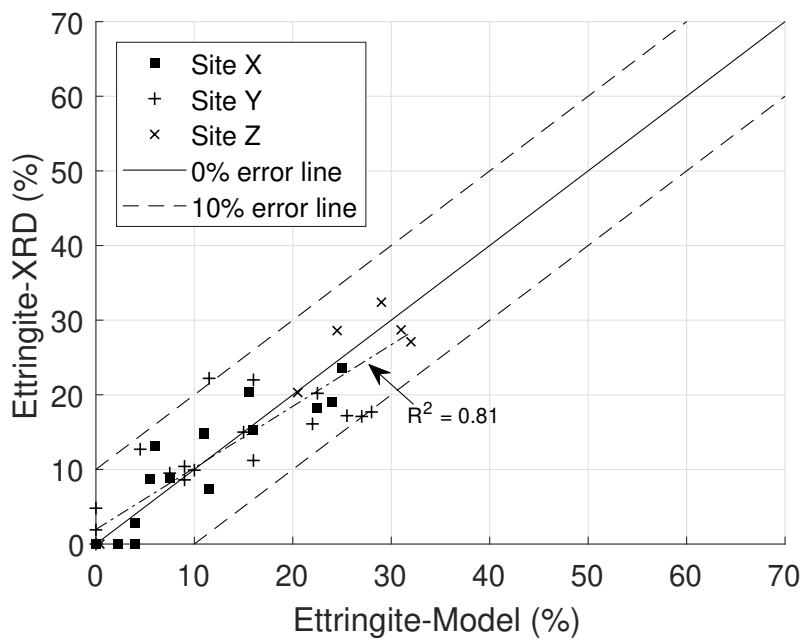
Figure 5.6: Quantitative comparison of ettringite: Experimental (XRD) vs. Thermodynamic Model (GEMS) (a) Site X,Y and Z before calibration (b) Site X,Y and Z after calibration. "Reprinted with permission from Elsevier".

5.5.4 Significance of calibration

The results of the thermodynamic model were calibrated to account for the assumptions in the model. GEMS-Selektor calculates phases at thermodynamic equilibrium. The samples tested using XRD may not have reached equilibrium at the time of testing. This is consistent with the modeling results as most of the data points show excess ettringite. This indicates that the tested samples have the potential for further ettringite precipitation. The input data for the thermodynamic model were based on the oxide content from XRF and stoichiometrically calculated content of gypsum. The oxide content of Al_2O_3 and CaO used in the model plays a critical role in quantifying ettringite. For example Al_2O_3 was used as the source of alumina in the model but there can be difference sources of alumina in the soil-ash mixture such as gibbsite $(Al(OH)_3)$ and kaolinite $(Al_2Si_2O_5(OH)_4)$. The thermodynamic parameter, solubility constant $logK_{sp}$ and kinetics of dissolution is different for minerals and their difference will affect the availability of alumina for ettringite formation. For example, If Al_2O_3 is present in an amorphous form, it can readily react with CaO, $SO_4{}^{2-}$ ions and water to form ettringite as compared to gibbsite and kaolinite.

The trend-line in Figure 5.6(a) shows a stable trend. This indicates that the assumption used in the thermodynamic model produces a consistent bias. For example the model calculates 20%, 40% and 60% ettringite for samples with 10%, 20% and 30% ettringite-XRD, respectively. The calibrated results in Figure 5.6(b) show that the data points fall within the 10% error line and are consistent with the experimental results. The mean deviation reduced from 10% to 0.1%.

5.5.5 Influence of CaO, SO$_3$, Al$_2$O$_3$, and SiO$_2$

The relationship between CaO content and ettringite formation is seen in Figure 5.7. Ettringite increased with increase in Ca (Figure 5.7(a), Figure 5.7(b). A similar trend is seen with the calibrated model. The trendline of the ettringite-model and the ettringite-XRD looks similar with the model slightly over calculating ettringite for CaO range 15-25%.
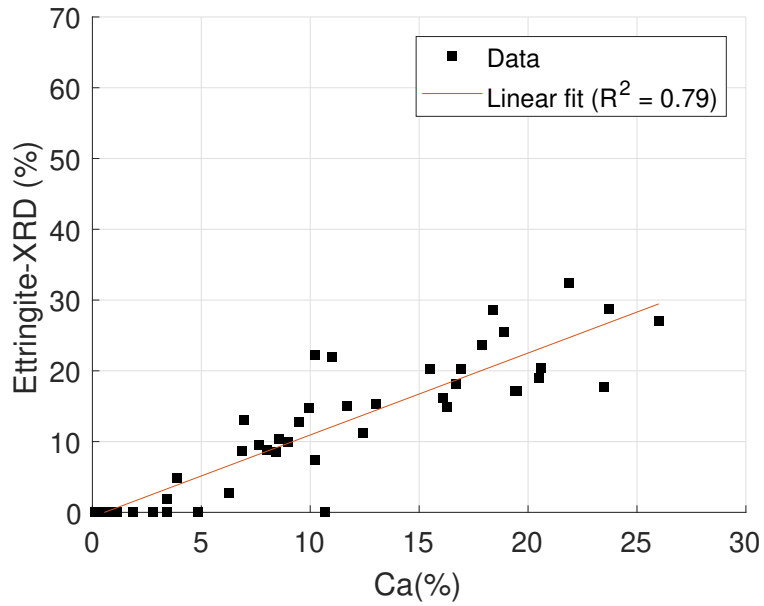
(a)
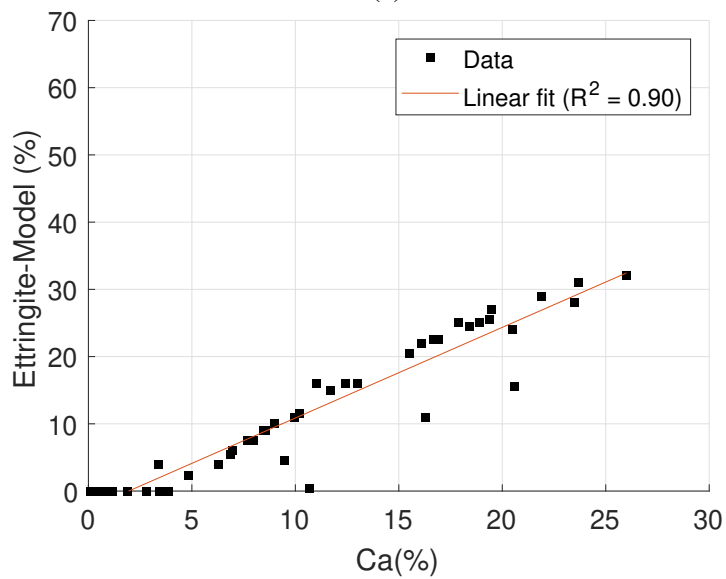
(b)

Figure 5.7: Effect of CaO in fly ash on ettringite formation (a) Experimental(XRD) Vs.CaO(%) (b) Ettringite(Model) Vs. CaO(%). "Reprinted with permission from Elsevier".
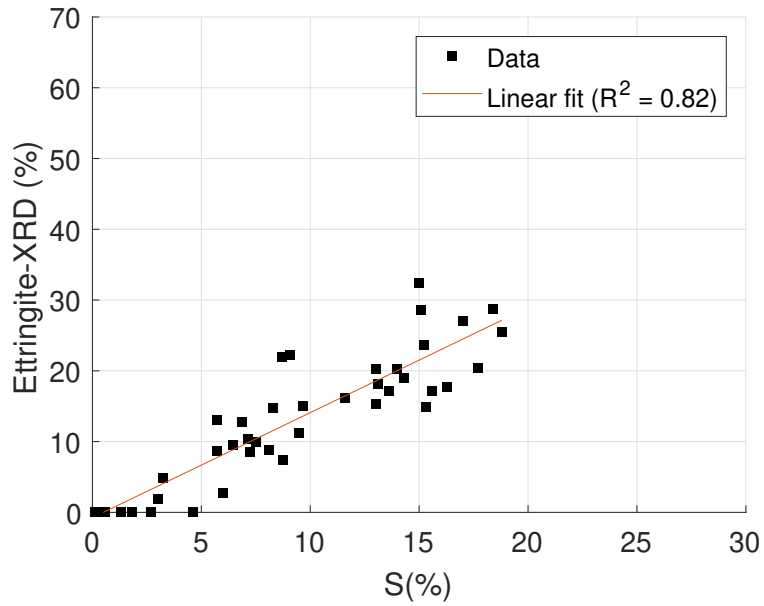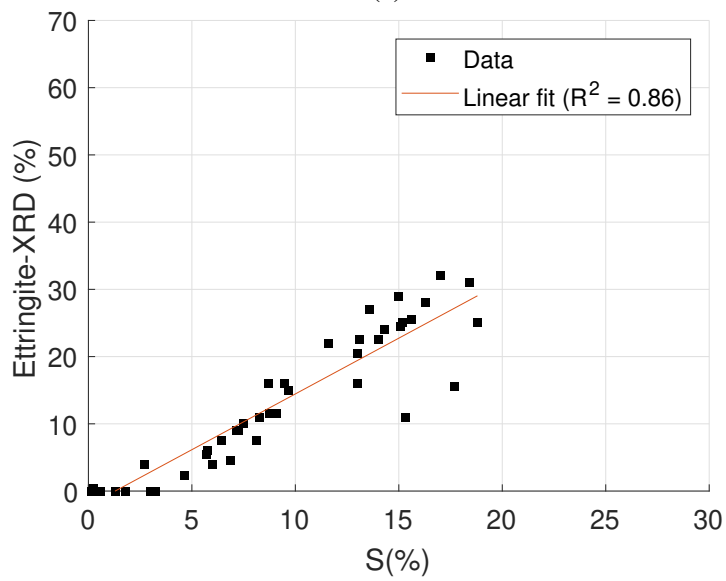
Figure 5.8: Effect of SO_3 in fly ash on ettringite formation (a) Experimental(XRD) Vs. $SO_3(\%)$ (b) Ettringite(Model) Vs. $SO_3(\%)$. "Reprinted with permission from Elsevier".
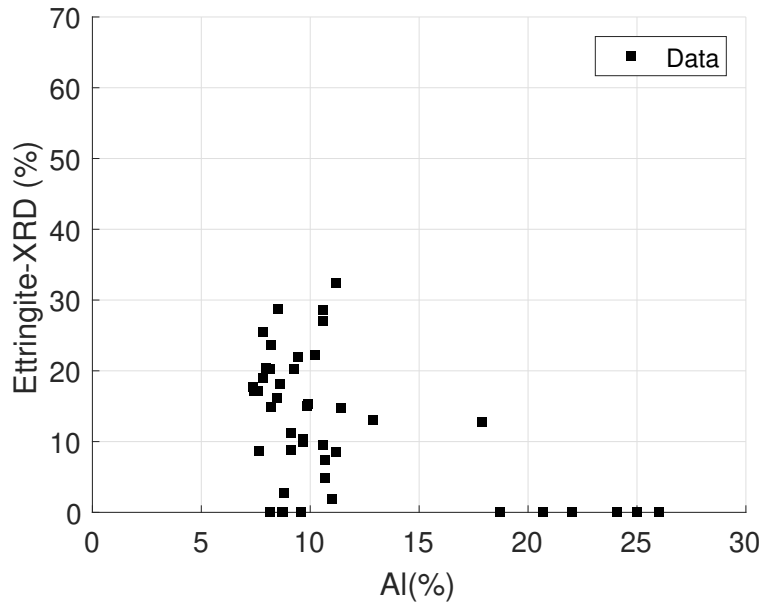
(a)
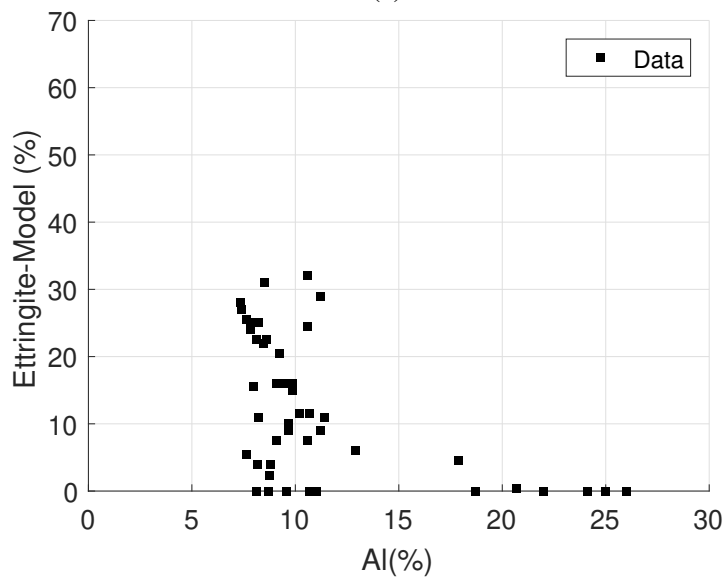
(b)

Figure 5.9: Effect of Al_2O_3 in fly ash on ettringite formation (a) Experimental(XRD) Vs.Al_2O_3(%)
(b) Ettringite(Model) Vs. Al_2O_3 (%). "Reprinted with permission from Elsevier".
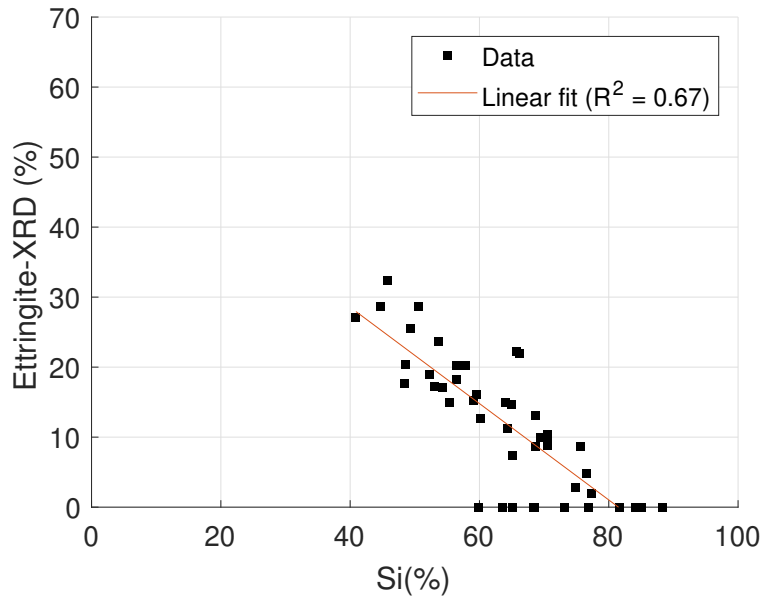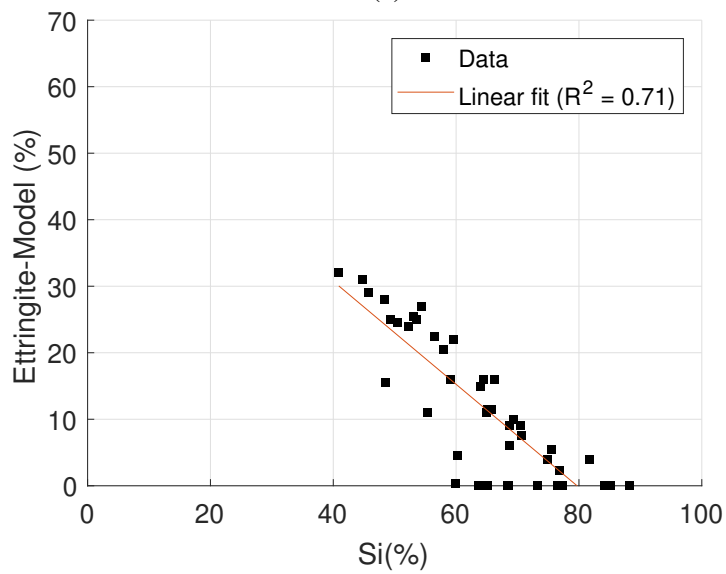
Figure 5.10: Effect of SiO_2 in fly ash on ettringite formation (a) Experimental(XRD) Vs. SiO_2 (%) (b) Ettringite(Model) Vs SiO_2 (%). "Reprinted with permission from Elsevier".

A similar trend is seen with increase in SO_3 as shown in Figure 5.8. The effect of CaO and SO_3 is analogous as gypsum contains both calcium and sulfate ions. This combined trend of increase in ettringite with increase in CaO and SO_3 further validates gypsum as the source of sulfate.

The relationship between Al_2O_3 and ettringite is shown in Figure 5.9(a) and Figure 5.9(b) does not follow an increasing or decreasing trend but most of the data points for ettringite are in the 5-15% range. When Al_2O_3 content was in the range 20% to 25%, the model and XRD did detect ettringite. In addition, The data points had low CaO and SO_3 contents. This shows that the content of CaO and SO_3 played a more critical role in the formation of ettringite compared to Al_2O_3. The CaO and SO_3 content from fly ash varied greater than Al_2O_3. If a significant source of alumina was present in the ash, the distribution of the data points would be similar to Ca (Figure 5.7) and S (Figure 5.8). As discussed earlier, the ash contained significant amount of CaO and SO_3. The nonhomogenous mixing of the ash with the soil resulted in a blended material composed of a wide range of CaO and SO_3 content. If the ash contained significant amount of Al_2O_3, the data points for Al_2O_3 would also exhibit a similar range. The accumulation of Al_2O_3 data points in a narrow range (Figure 5.9) suggests that the source of Al_2O_3 is from the soil and not from the added fly ash. The ettringite calculated with the model and XRD are in the range 0% to 35% (Figure 5.9(b)). The data points that show higher ettringite formation have high SO_3 and CaO contents, which theoretically favors more ettringite formation.

The relationship between increase in silica (SiO_2) and ettringite is shown in Figure 5.10 (a)-(b). An increase in SiO_2 results in a reduction in ettringite formation in both the model and experiment. This is because samples with high SiO_2 (greater than 70%) have a mean pH of 8.7 when compared with samples with less than 70% SiO_2, which had a mean pH of 10.4. Precipitation of hydration products such as calcium-silicate-hydrate and other silicious amorphous products would have reduced the concentration of Ca^{2+} and OH^- ions (reduced pH) needed for ettringite formation. This causes a reduction in pH and therefore samples with high SiO_2 showed a reduced pH. Also, Little et. al. [144] showed that pH 10-12 is favorable for ettringite formation. Hence, the coupled experimental and thermodynamic approach shows the applicability of the model as a forensic tool.

5.5.6 Quantitative analysis

A qualitative assessment of ettringite prediction is critical to understand the efficacy of using thermodynamic modeling. A total of 45 samples were analyzed and ettringite was experimentally detected in 37 samples. However, the model predicted ettringite in 35 of the 45 samples (Table 5.3). Therefore, comparing 35 samples predicted by the model with the 37 samples with experimental evidence of ettringite yields a reliability of 94.5%. In this analysis samples that recorded less than 1% ettringite were considered to be insignificant as it is difficult to quantify ettringite at a low percentage and its presence at this low percentage is considered of very low practical significance. The results indicate the thermodynamic models can be used to predict ettringite formation with a good reliability.

5.6 Phase stability diagram

The objective of the phase stability diagram was to study the effect of amorphous silica on ettringite formation. The stability fields of minerals and aqueous phases were based on thermodynamic properties of minerals and the net activity of ions present in the system. Experimental and GEMS results demonstrate that samples with high silica content ettringite did not form. This can be explained with a phase stability diagram by modeling the stabilization of a typical non-expansive clay soil (e.g., kaolinite) with ash high is sulfate content. Figure 5.11 shows the stability fields of ettringite, kaolinite and Afm phases C_2AH_8 and C_3AH_6, respectively. The loci of thermodynamic equilibrium point A was located based on the activity of SO_4^{2-} (obtained from GEMS) and the average pH (Table 5.2). It shows that ettringite is stable at equilibrium for the stabilized soil. Figure 5.11(b) shows the phase stability diagram of the same sample when amorphous silica (higher activity of silica) was added to it. The activity of silica increase when amorphous silica is added. In this case the stability field of ettringite is diminished and the equilibrium point B lies outside the ettringite region. Hence, when amorphous silica is added ettringite is not thermodynamically favored.

71
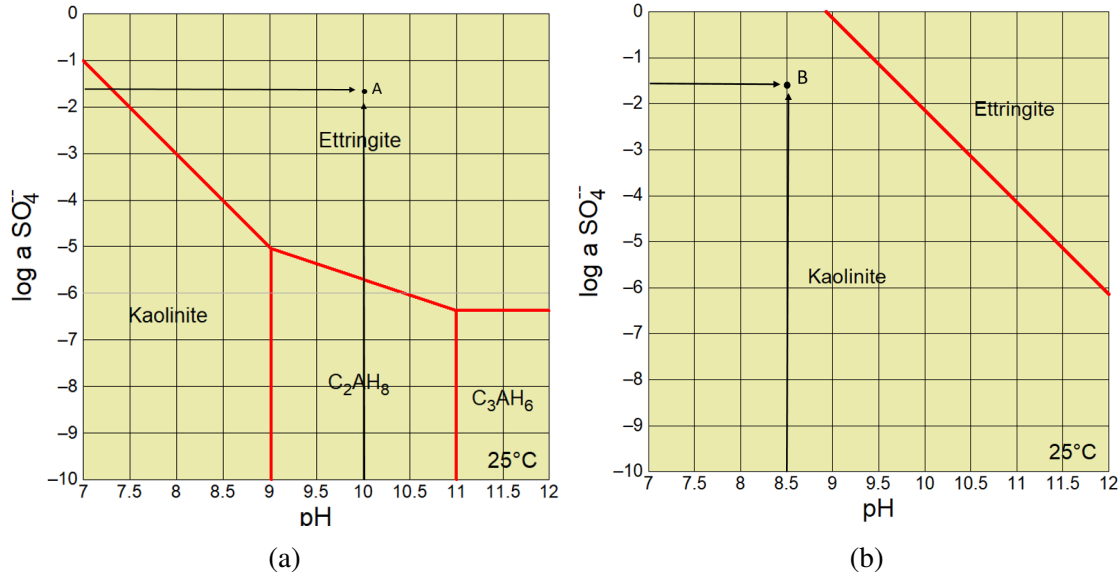
Figure 5.11: Phase stability diagram of the stabilized soil (a) with no amorphous silica (Temperature $= 25^oC$, pressure $= 1$ atm, Ca^{2+} activity $= 10^{-1.41}$, Al^{3+} activity $= 10^{-4.55}$); (b) with 10% amorphous silica (Temperature $= 25^oC$, pressure $= 1$ atm, Ca^{2+} activity $= 10^{-1.41}$, Al^{3+} activity $= 10^{-4.55}$, $H_4SiO_{4(aq)}$ activity $= 10^{-3.00}$). "Reprinted with permission from Elsevier".

5.7 Conclusion

The structural distress at various locations in this case history was due to ettringite formation in subgrade (foundation) soil stabilized with ash. High variability of CaO and SO_3 content shows poor mixing of fly ash with the in-situ soil and stoichiometric calculations indicate gypsum as the primary source of Ca^{2+} and $SO_4{}^{2-}$ ions. The amount of CaO, SO_3, Al_2O_3 and SiO_2 plays a critical role in ettringite formation. An increase in CaO and SO_3 resulted in increased ettringite formation. Samples with high SiO_2 had lower pH that further reduces the ettringite formation.

The following points support the use of thermodynamic modeling as an effective forensic tool

1. The model is based on physical chemistry and the minimization of Gibb's free energy, which is well established and widely used.

2. The model predicts an increase in the product, ettringite, consistent with an increase in the reactants and this relationship has a high degree of correlation with the empirical evidence.

3. Despite the limitations of not considering kinetics, a linear shift bring model predictions into very close agreement with empirical data (mean error 0.12% with SD 4.3%), and this linear shift is consistent with the linear relationships between model predictions and empirical data when considering each reactant individually.

4. As observed in the experimental analysis, the phase diagrams show that an increase in activity of silica deters ettringite formation.

The next logical step in the development of a more advanced forensic tool is to incorporate reaction kinetics and to better define dissolution rates of the reactants. This will be the focus of continued development of this approach.

6. MINERALOGICAL CHARACTERIZATION AND THERMODYNAMIC MODELING OF SYNTHESIZED ETTRINGITE Ca-Al-SO$_4$ SUSPENSIONS

6.1 Introduction

Ettringite (Ca$_6$Al$_2$(SO$_4$)$_3$(OH)$_{12}$ $\cdot$ 26 H$_2$O), a naturally occurring mineral can be found in hydrated cements and clayey soils stabilized using a pozzolanic material [4, 5]. It is an important hydration product contributing to early strength in low CO$_2$ calcium-sulfo-alumiate (CSA) cements [6]. Forming too much ettringite post hydration can cause substantial distress and affect the durability of the material. Excessive ettringite formation causing negative effects is refereed to as sulfate attack. Little and Puppala [7, 8] have studied the distress mechanism of sulfate attack in chemically stabilized soils. The study indicated that excessive formation of ettringite can cause significant heave. Similarly, in concrete subjected to sulfate attack, precipitation of ettringite is attributed to the damage [145, 146]. Guo et. al. [147] and Hou et. al. [148] have successfully used Mg-Al-CO$_3$ and Nono-Silica to deter the formation of ettringite and to increase resistivity to sulfate attack.

Ettringite is a needle like structure comprising hexagonal and prismatic crystals [71]. The length of the crystals can vary from few microns to about 200 μm [149, 150]. Water is critical for ettringite stability [151, 12]. Moore [71] indicated that ettringite contains 26 moles of H$_2$O and dehydration of ettringite forms metaettringite an X-Ray amorphous phase with 10 to 13 moles of H$_2$O [152].

Several methods have been proposed to synthesize ettringite in a CO$_2$ free environment [153, 154, 155]. The effect of CO$_2$ during the mixing process plays a critical effect on the equilibrium pH and available Ca^{2+} ions for ettringite formation. Ettringite formed under air exposure will provide additional insights regarding the morphological and equilibrium stability of ettringite. The length and diameter of ettringite crystals is higher at pH 9.4 than pH 12.5 when ettringite is synthesized in solutions with Cao"Al$_2$O$_3$ molar ratio of 6:1[154]. Teri et. al. [153] synthesized ettringite from

portlandite suspensions at various Ca/Al ratios. The study indicated that at 48 hours, ettringite began to form at Ca/Al = 1.5 and over.

Thermodynamic modeling to simulate the interaction of the solid and liquid phase during reaction was carried out to improve the understanding of the process and to evaluate the practical applicability of the models to predict ettringite formation. For this purpose, two thermodynamic models were used. First, a Gibb's energy minimization (GEM) based model GEMS-PSI [93, 128, 129] was used to calculate solid phases at equilibrium. Second, a law of mass action (LMA) based model, Geochemist's Workbench (GWB) software [156] was used to construct a phase stability diagram. GWB is a simple and effective model for qualitative analysis. Kulik et. al. [28] has described in detail the differences between the GEM and LMA models. Similar thermodynamic models have been used to model cement hydration [124, 157] and soil stabilization [58, 158].

The main purpose of this paper is to evaluate the applicability of thermodynamically models to predict ettringite formation in $Ca-Al-SO_4$ suspensions with different molar ratios of Ca:Al. In addition, an emphasis on the mineralogical and morphological characterization of the precipitated solid phases provided insights on the reaction path. Based on the results, a strong discussion is presented on the application of thermodynamic models to predict ettringite formation for field applications where sulfate attack is of concern.

6.2 Geochemical Reactions

The geochemical reactions when $Ca(OH)_2$ is added to a $Al_2(SO_4)_3 \cdot 18\,H_2O$ suspension can be split into two parts. First, the dissolution mechanism that the favors dissolution $Ca(OH)_2$ and $Al_2(SO_4)_3 \cdot 18\,H_2O$ when added to water. The solubilities of $Ca(OH)_2$ and $Al_2(SO_4)_3 \cdot 18\,H_2O$ at $20\,°C$ are $2.3\,g/100mL$ and $36.4\,g/100mL$, respectively.

$$Ca(OH)_2 \longrightarrow Ca^{2+} + 2\,OH^- \tag{6.1}$$

$$Al_2(SO_4)_3 \cdot 18\,H_2O \longrightarrow 2\,Al^{3+} + 2\,SO_4{}^{2-} + 18\,H_2O \tag{6.2}$$

The second part of the reaction comprises of the precipitation of solid phases of ettringite $(Ca_6Al_2(SO_4)_3(OH)_{12} \cdot 24\text{-}32\,H_2O)$, gypsum $(CaSO_4 \cdot 2\,H_2O)$, calcite $(CaCO_3)$, and amorphous gibbsite $(Al(OH)_3)$ as indicated in Equations 6.3 to 6.6.

$$6\,Ca^{2+} + 2\,Al^{3+} + 3\,SO_4{}^{2-} + 12\,OH^- + 26\,H_2O \rightleftharpoons Ca_6Al_2(SO_4)_3(OH)_{12} \cdot 26\,H_2O(ettringite)$$

$$(6.3)$$

$$Ca^{2+} + SO_4{}^{2-} + 2\,H_2O \rightleftharpoons CaSO_4 \cdot 2\,H_2O(gypsum) \qquad (6.4)$$

$$CaO + CO_2 \rightleftharpoons CaCO_3(calcite) \qquad (6.5)$$

$$Al^{3+} + 3\,OH^- \rightleftharpoons Al(OH)_3(gibbsite(am)) \qquad (6.6)$$
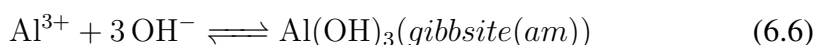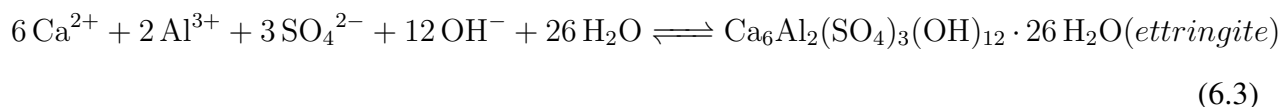
6.3 Methods

The methodology for experimental analysis and thermodynamic modeling used in this study is shown in Figure 6.1.

6.3.1 Synthesis

Reagent grade $Ca(OH)_2$ and $Al_2(SO_4)_3 \cdot 18\,H_2O$ were used as sources of Ca, Al, and, SO_4, respectively. Al-sulfate solution was prepared by diluting $Al_2(SO_4)_3 \cdot 18\,H_2O$ in $300\,mL$ of water. A solution providing Ca^{2+} ions was prepared by mixing $Ca(OH)_2$ reagent with $100\,mL$ of water. The solutions were transferred to a $400\,mL$ beaker and continuously mixed for 14 days with a magnetic stirrer. The molar quantities of $Ca(OH)_2$ were varied to develop different molar ratios of $Ca(OH_2)$ to $Al_2(SO_4)_3 \cdot 18\,H_2O$ as seen in Table 6.1. A two step approach was used for filtering the solids. First, the $Ca-Al-SO_4$ suspension was vacuum filtered with a $1.5\,\mu m$ filter paper. Second, the filtered solids were placed in isopropanol for 15 min to stop hydration and vacuum filtered [159]. The solids were then dried in a desiccator with a saturated $MgCl_2$ solution to maintain a relative humidity of approximately 30% at room temperature. Prior to characterization, the solids were heated at $30\,°C$ for $15\,min$ to remove the isopropanol.

Table 6.1: Mass and Molar quantities of $Ca(OH_2)$ and $Al_2(SO_4)_3 \cdot 18\,H_2O$ used in the synthesis

ID	$Ca(OH)_2$		$Al_2(SO_4)_3 \cdot 18\,H_2O$		Molar ratio
	g	M	g	M	
CA1	0.74	0.01	6.65	0.01	1
CA3	2.22	0.03	6.65	0.01	3
CA4	2.96	0.04	6.65	0.01	4
CA5	3.70	0.05	6.65	0.01	5
CA6	4.44	0.06	6.65	0.01	6

6.3.2 Experimental characterization

Solid characterization comprised of semi-quantitative X-Ray diffraction (QXRD), thermogravimetric analysis (TGA), scanning electron microscopy (SEM), and Fourier transformed infrared spectroscopy (FTIR). The pH and electrical conductivity of the suspensions were also measured after 14 days of mixing.
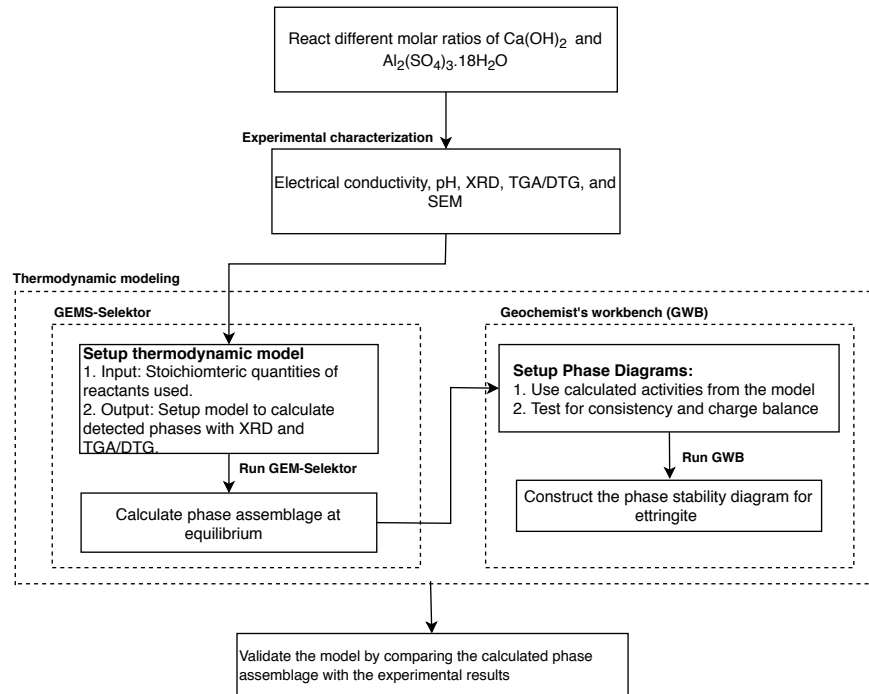
Figure 6.1: Methodology flowchart

X-Ray diffraction analysis of the synthesized soil precipitate were performed on a Bruker D8 unit using CuKα radiation at a current of $40\,\text{mA}$, 30kV. The dried solids were pulverized using an agate mortar and passed through a $63\,\mu\text{m}$ sieve. The diffractograms were recorded over the range of $5°$ to $70°$ at a scanning rate of $0.5\,°\,\text{min}^{-1}$. Reference intensity ratio method [160] in the powder diffraction program Match! [161] was used for the semi quantitative crystalline phase analysis. The experimental TGA setup consisted of a heating range from $30\,°\text{C}$ to $1000\,°\text{C}$, heating rate of $20\,°\text{C}\,\text{min}^{-1}$ with a N_2 purging gas at $30\,\text{mL}\,\text{min}^{-1}$. The FTIR spectral analysis was recorded using a Thermo Nicolet 380 FTIR spectrometer equipped with diamond tipped ATR stage over a range of $4000\,\text{cm}^{-1}$ - $650\,\text{cm}^{-1}$. Each FTIR was scanned 32 times to improve accuracy. Vibrational spectra were obtained by subtracting the recorded data from the background spectra. Microscopic examination of the solid phases were carried out using a JEOL JSM-7500F. It is known that vacuum dehydrates ettringite but we did not observe any visible decomposition.

6.3.3 Thermodynamic modeling

Thermodynamic modeling was carried out using GEMS-PSI [93, 128, 129] and Geochemist's Workbench softwares. GEMS-PSI with the thermodynamic database CEMDATA 14 [162] was used to calculate the thermodynamic equilibrium solid phase distribution. The input data comprised of the mass of $Ca(OH)_2$ and $Al_2(SO_4)_3 \cdot 18\,H_2O$. Geochemist's Workbench [156] was used to construct the phase stability diagram. It was used to determine the following: (i) The stability region of ettringite, and (ii) The thermodynamically favored phase. The calculated equilibrium activities of Ca^{2+}, Al^{3+}, and $SO_4{}^{2-}$ ions from GEMS-PSI were used as input data.

6.4 Results and Discussion

6.4.1 Electrical conductivity and pH

The pH and electrical conductivity (EC) of the suspensions were measured at 14 days after the solids in the suspension were allowed to settle. This helped to improve the accuracy of the measurement. Figure 6.2 shows the change in pH and EC for the synthesized suspensions. As expected, the pH increased with an increase in $Ca(OH)_2$. Samples CA1 and CA3 recorded pH
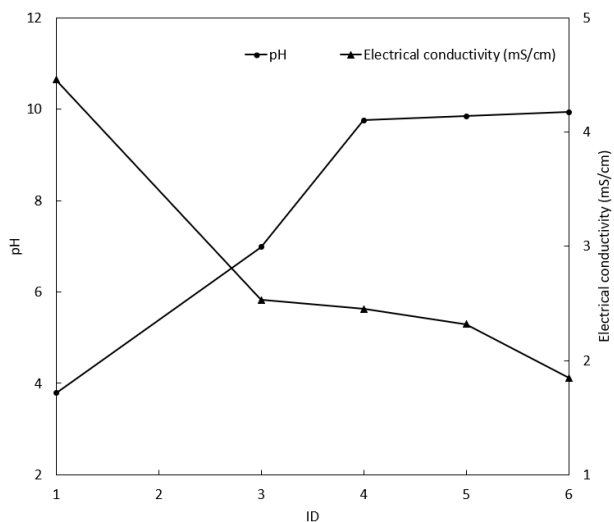
Figure 6.2: Electrical conductivity and pH of samples

values of 3.79 and 6.98, respectively. The pH of samples CA4, CA5, and CA6 were about 10. When pH is less than 7, dissolution of ettringite to microcrystalline gibbsite ($Al(OH)_3$) and gypsum ($CaSO_4 \cdot 2\,H_2O$) is favored [70]. The magnitude of the EC values corresponds to the amount of dissolved ions present in the suspension. The trend shows that EC decreases with increase in $Ca(OH)_2$ indicating a decrease in dissolved ions. The data suggests that the precipitation solids from the suspension follows the order CA6>CA5>CA4>CA3>CA1.

6.4.2 Thermogravimetric analysis (TGA/DTA)

A qualitative analysis of the precipitated solid phases was carried out using TGA/DTA. The analysis indicated mass loss over four temperature intervals (Figure 6.3(a) and 6.3(b)). The weight loss between $50\,°C$ and $110\,°C$ is due to water loss from ettringite as seen in samples CA4, CA5, and, CA6. Conversion of gypsum to anyhdrite occured in the temperature interval $110\,°C$ and $150\,°C$ (as seen in samples CA1 to CA5). Amorphous $Al(OH)_3$ also formed when ettringite formed and the dehydroxylation (removal of OH) peak of amorphous gibbsite is seen at $250\,°C$. Additional peaks due to decarboxylation (removal of CO_2) of calcite was seen at $600\,°C$ in samples CA4, CA5, and, CA6, respectively. The TGA results indicated ettringite as the major phase in CA6. In contrast, gypsum was the major phase in samples CA1 and CA3.
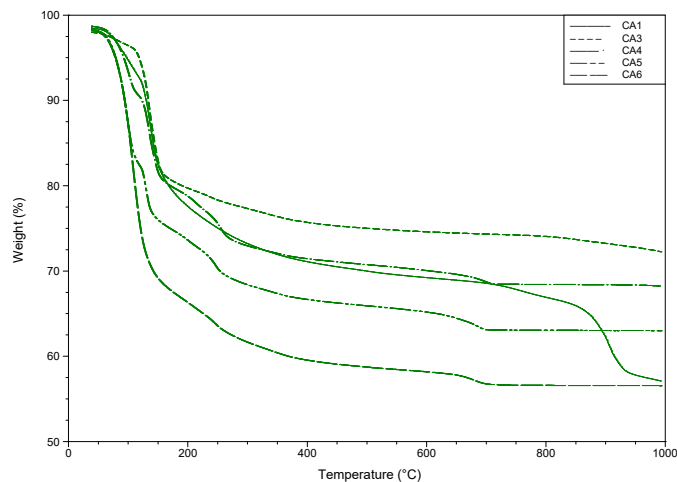
(a)
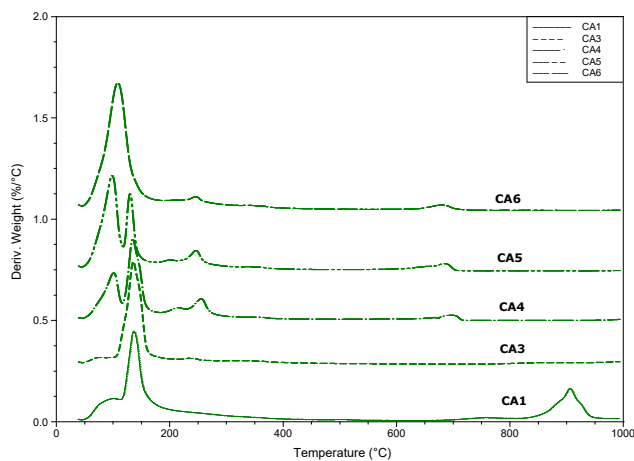
(b)

Figure 6.3: (a) Thermogravimetric analysis of samples, (b) Differential thermogravimetric analysis of samples

6.4.3 Fourier Transform Infrared Spectroscopy

FTIR was used to primarity identify changes in functional groups $Al-O-H$, SO_4 and, H_2O. Figure 6.4 shows the comparison of FTIR spectra for samples CA1, CA3, CA4, CA5, and CA6. A description of the significant spectral peaks is shown in Table 6.2. The peak at $853\,\mathrm{cm}^{-1}$ is the

Al$-$O$-$H bending vibration from amorphous gibbsite [163]. SO_4 vibrations are seen at $1108\,cm^{-1}$. The low transmittance values for CA1, CA3, and CA4 indicates a high population of SO_4 bonds from gypsum and the high transmittance values in CA5 and CA6 corresponds to SO_4 vibration from ettringite. Samples CA1 and CA3 exhibit a well defined peak at $1663\,cm^{-1}$ and $3421\,cm^{-1}$ that corresponds with the vibrational wavelength of H_2O. The peak at $1450\,cm^{-1}$ corresponds to CO_2 vibration from calcite [164].

Table 6.2: Comparison of Fourier Transform Infrared Spectroscopy spectra of samples CA1, CA3, CA4, CA5, and CA6

Peak wave numbers (cm^{-1})	comments [163]
853	Al$-$O$-$H (bending vibration)
1108	SO_4
1450	CO_3
1663, 3421	H_2O
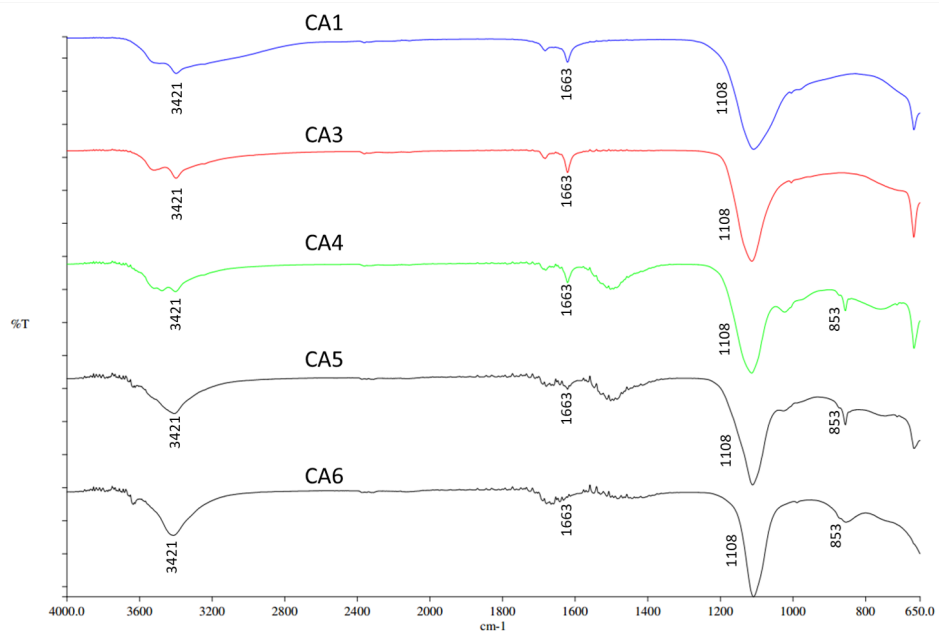
Figure 6.4: FTIR absorbance of synthetic ettringite samples CA1, CA3, CA4, CA5, and CA6

81

6.4.4 Scanning Electron Microscopy (SEM)

SEM was used to investigate the morphology of the precipitated phases gypsum (G), and portlandite (P), and ettringite (E) as shown in Figure 6.5(a) to 6.5(e).The phases showed similar morphological features across all synthesized samples. Gypsum had a tubular structure in Figure 6.5(a) to 6.5(d). Unreacted portlandite was also seen as thin plate-like structures. Ettringite exhibited the characteristic thin needle like structure as seen in Figures 6.5(d) and 6.5(e). Ettringite was the major precipitated phase in CA6 with crystal lengths ranging between $3\,\mu m$ to $5\,\mu m$. The observations from the SEM micrographs agree with the DTG/TGA and XRD analysis.

(a)   (b)   (c)

(d)   (e)
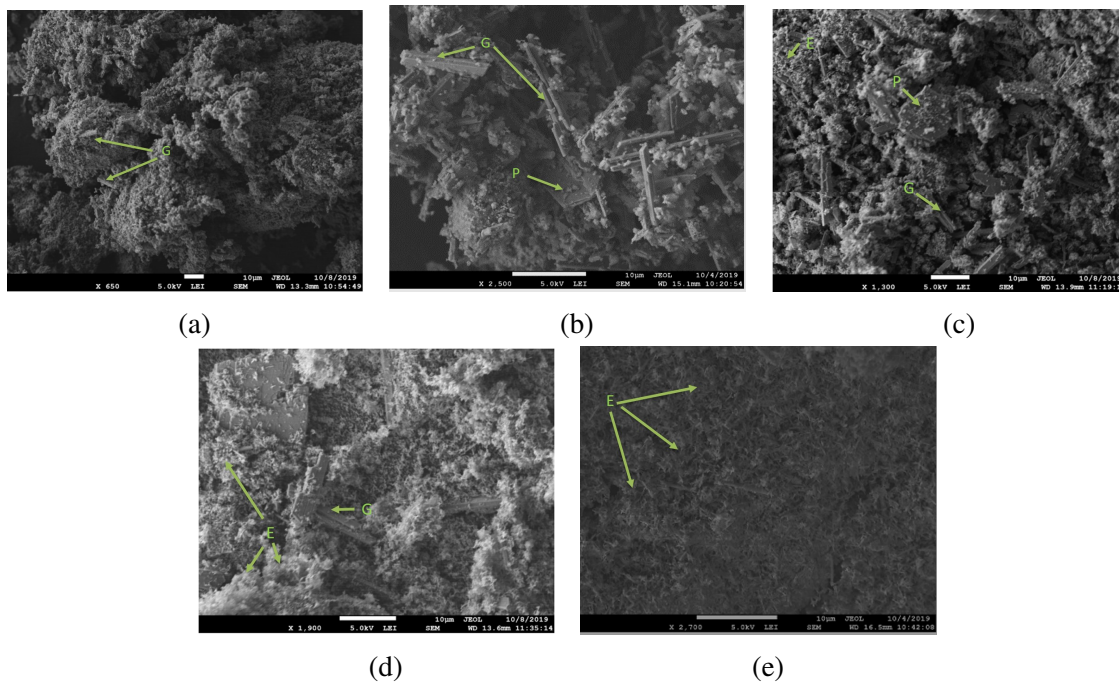
Figure 6.5: SEM micrograph of precipitated products Ettringite(E), Gypsum (G), and Portlandite (P) from synthesis samples (a) CA1 (b) CA3 (c) CA4 (d) CA5 (e) CA6

6.4.5 X-Ray diffraction

XRD was used for qualitative (Figure 6.6) and a semi-quantitative analysis (Reference Intensity Ratio method) of the formed crystalline phases. Figure 6.7 shows the result of the semi-quantitative analysis. Gypsum as the only stable crystalline phase in samples CA1 and CA3. The absence of ettringite in CA1 and CA3 must be due to the low ($<$7) pH values. Ettringite precipitated at higher $Ca(OH)_2$ concentrations (CA4, CA5, and CA6) and the quantity also increased from 50% in sample CA4 to 93% in sample CA6. Contrary to CA1 and CA3, samples CA4, CA5 and, CA6 demonstrated a pH range from 9.6 to 9.9 within the stable region of ettringite. The quantity of gypsum also decreased with the increase in $Ca(OH)_2$. Calcite was also observed in samples CA4, CA5, and CA6.
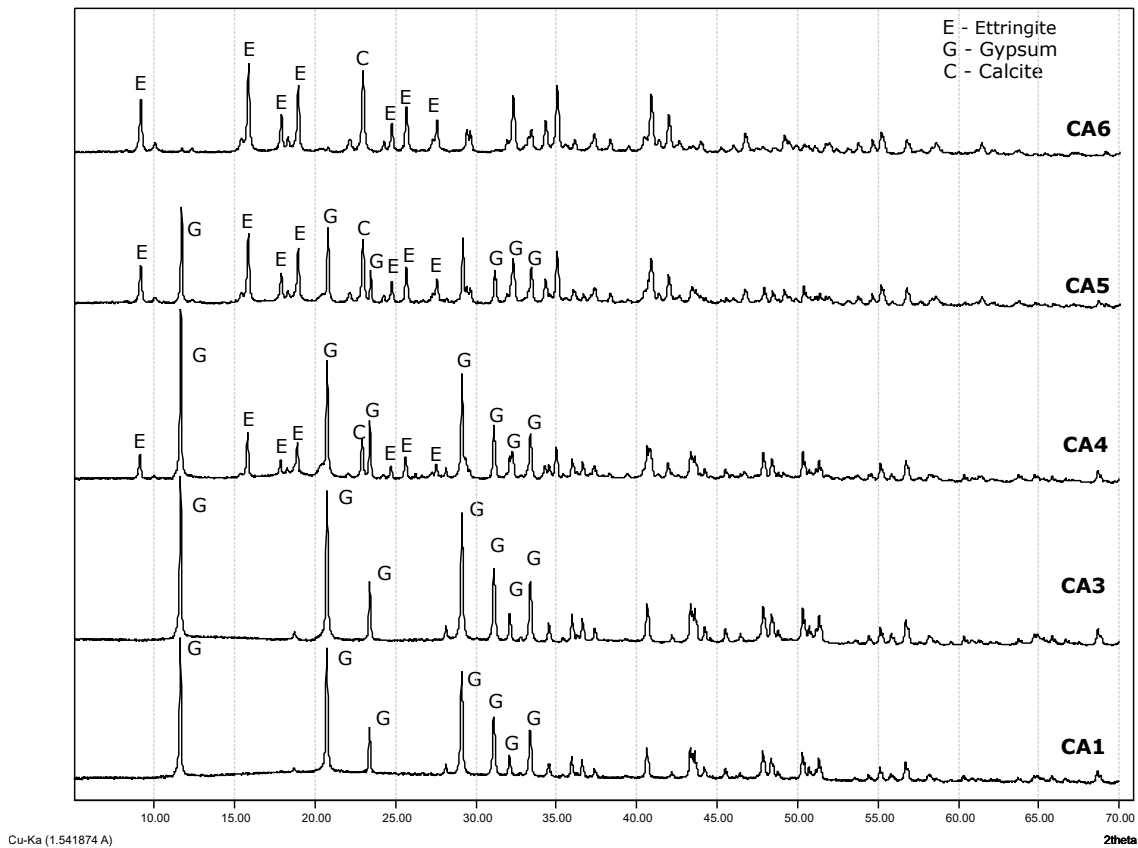
Figure 6.6: X-Ray diffractogram of samples CA1, CA3, CA4, CA5, and, CA6

6.4.6 Thermodynamic modeling

A thermodynamic model was setup to predict the reaction between $Ca(OH)_2$ and $Al_2(SO_4)_3 \cdot 18\,H_2O$. In particular, formation of crystalline phases ettringite, gypsum and, calcite were of primary interest. Figure 6.7(a) shows the solid phase assemblage calculated by the model for samples CA1 to CA6. In samples CA1 and CA3, gypsum is the only stable crystalline phase. The results agree with the observations from the X-Ray diffractogram as seen in Figure 6.7(b). Ettringite was shown to be the stable phase with increase in $Ca(OH)_2$ concentration as observed in samples CA4, CA5, and CA6. This may be due to the combined increase in pH and Ca^{2+} ion concentration consistent with higher concentrations of $Ca(OH)_2$. In addition, an increase in the quantity of ettringite and a decrease in the quantity of gypsum was seen at higher concentrations of $Ca(OH)_2$ (CA4 to CA6). The model predicted the transition from gypsum to ettringite and was able quantify ettringite formation. The model calculated 24, 64, and, 93 g/100g of ettringite in samples CA4, CA5, and CA6 respectively, which is consistent with the semi-quantitative analysis of the samples. This further supports the quantitative prediction capabilities of the model. The comparison of the modeling results with the semi-quantitative analysis substantiates the qualitative and quantitative capabilities.

6.4.7 Phase stability diagram

The calculated equilibrium activities were used to construct the phase stability diagram and to determine the thermodynamic equilibrium point for samples CA1 to CA6 as seen in Figure 6.8. When compared to ettringite, gypsum is thermodynamically more stable in samples CA1 and CA3 which is consistent with the experimental results. In samples CA4 and CA5, the equilibrium point falls on the ettringite-gypsum phase boundary, indicating the stability of both the phases. Ettringite is the only stable phase in samples CA6 as indicated the XRD analysis. The results of the phase stability diagram agree with the XRD, SEM, and TGA/DTA analysis results.
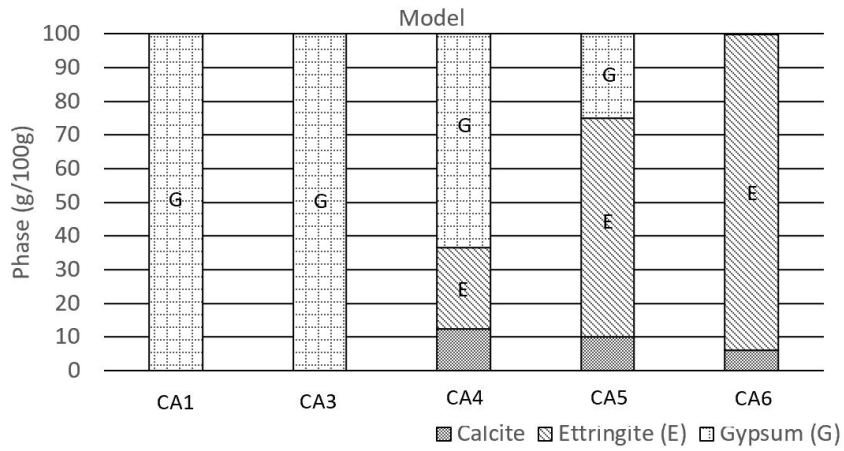
(a)
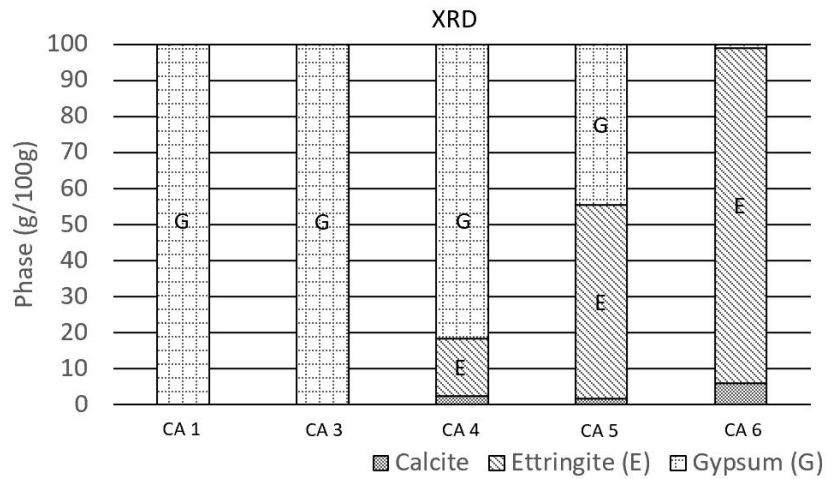
(b)

Figure 6.7: Comparison of the thermodynamic model (Figure 7(a)) results with the the semi-quantitative X-Ray diffraction analysis results (Figure 7(b))
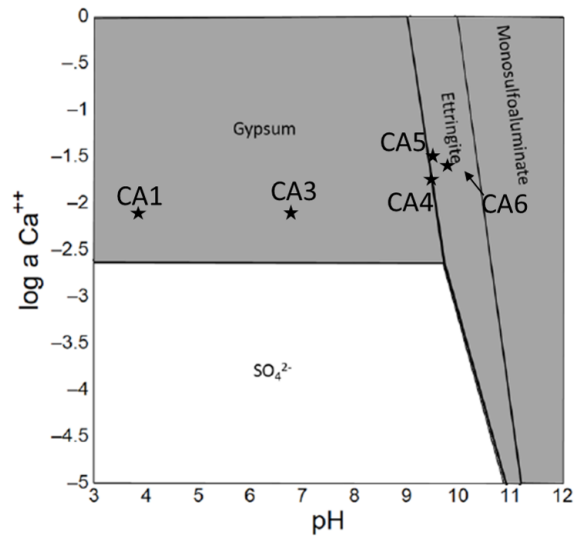
Figure 6.8: Phase stability diagram for ettringite synthesized from Ca-Al-SO$_4$ suspension drawn with the following conditions: T = $25\,^\circ$C, P = 1 atm, Al^{3+} activity $10^{-18.4}$, SO$_4$ activity $10^{-2.04}$

6.5   Conclusion

Experimental characterization and thermodynamic modeling were used to investigate ettringite formation in Ca-Al-SO$_4$ suspensions. Samples with different concentrations of Ca(OH)$_2$ were mixed with Al-SO$_4$ solution to produce Ca-Al-SO$_4$ suspensions with different molar ratios of Ca:Al. Gypsum precipitated in samples with Ca:Al molar ratios less than 3:1 (CA1 and CA3). At higher Ca:Al molar ratios (CA4, CA5, and CA6), ettringite precipitated. Amorphous Al(OH)$_3$ also precipitated as a minor phase with ettringite. An increase in ettringite content was observed with increase in Ca(OH)$_2$ both thermodynamically and experimentally. The Ca-Al-SO$_4$ suspension also reacted with atmospheric CO$_2$ to form calcite. Based on the results from this study, ettringite is stable at pH 9.7 and higher. The Ca-Al-SO$_4$ suspensions reacted differently to form different quantities of ettringite, gypsum and calcite at equilibrium. The thermodynamic model developed showed the quantitative and qualitative predictive capabilities. The phase diagram can be used together with the modeling results to effectively characterize the reaction products.

7. SUMMARY, RECOMMENDATIONS AND FUTURE RESEARCH DIRECTIONS

This dissertation investigated the application of thermodynamic modeling for chemically stabilized soils. Models based on the Gibbs' free energy minimization method (e.g., GEM-Selektor) and law of mass action method (e.g., Visual MINTEQ and Geochemist's Workbench) were successfully applied to simulate the soil stabilizer reaction. A summary of the results are as follows.

7.1 Thermodynamic evaluation of smectite treated with hydrogen ion stabilizer

1. The thermodynamic model was able to simulate the stabilization mechanism of smectite treated with a hydrogen ion stabilizer.

    (a) The model favored dissolution of smectite treated with concentrated HIS.

    (b) At lower concentrations, the model indicated release of Al^{3+} ions from the octahedral layer of smectite. In addition, partial dissolution of the octahedral layer with release of amorphous silica was shown to be thermodynamically favored.

    (c) The postulated stabilization mechanism from the modeling resulted is the adsorption of Al^{3+} ions from the octahedral layer on the net negative surface of clay reducing the shrink-swell potential. Amorphous silica acted as a shield around the clay colloids inhibiting free water movement.

2. Macroscopic evaluation: The HIS treated samples recorded less swell when compared with the untreated samples even after three wet-dry cycles. This indicated long term stability of stabilization. Mineralogical tests confirmed complete dissolution of smectite at higher HIS concentrations (undiluted HIS) as indicated by the model. XRD showed a reduced d-spacing for smectite with diluted HIS. The reduced d-spacing was attributed to the adsorption of Al^{3+} ions at the interlayer.

3. The thermodynamic model simulated the stabilization mechanism that was validated by the microscopic (XRD, FTIR) and macroscopic tests (swell test) to understand the stabilization

mechanism of the hydrogen ion stabilizer.

7.2 Coupled thermodynamic and experimental approach to evaluate ettringite formation in a soil stabilized with fluidized bed ash by-product: A case study

Severe structural distress was recored in the foundation of a shopping complex where the soil was treated with a fluidized bed ash by-product. Forensic investigation indicated ettringite as the potential cause of heave due to high soluble sulfate levels in the coal combustion product.

1. A thermodynamic model was constructed using only the XRF data of the untreated soil. calcium sulfate from a coal combustion by-product was used as the only source of sulfate in the study. The quantity of calcium sulfate was calculated from the respective CaO and SO_3 content (from the XRF analysis).

2. The results showed a consistent trend of over-predicting ettringite due to lack of sufficient mineralogical characterization. The calibrated results were in good agreement with the experimentally calculated ettringite. After calibration, the mean error for quantitatively predicting ettringite reduced from 23% to 0.4%.

3. Experimentally, samples with high SiO_2 showed reduced ettringite formation indicating the effect of silica on ettringite formation. It can be attributed to the usage of Ca^{2+} ions for forming other calcium dominated pozzolanic products such as CSH and CAH.

4. A phase diagram constructed with the activities of calculated from GEMS predicted that at increased SiO_2 concentrations, ettringite formation was not thermodynamically favored.

7.3 Mineralogical characterization and thermodynamic modeling of synthesized ettringite from Ca-Al-SO_4 suspensions

The lack of mineralogical data in the fluidized bed ash study (soil stabilized with fluidized bed ash by-product) indicated the need for calibration of the results to achieve a reliable a prediction. This study investigated the potential to use a thermodynamic model to predict ettringite formation

when sufficient characterization (mineralogical and geochemical) was available. A thermodynamic model with sufficient mineralogical data was used to simulate the reactions between $Ca(OH)_2$ and $Al_2(SO_4)_3 \cdot 18\,H_2O$.

1. Ca:Al ratios of 1:1,3:1,4:1,5:1 and 6:1 were used in this study. The samples with lower Ca:Al ratio (1:1 and 3:1) recored high electrical conductivity and low pH (< 7). The pH increased with increase in Ca ions but the electrical conductivity (EC) showed a decrease in EC with increase in Ca. The results are in agreement with the other studies that show ettringite to be stable at pH ≥ 9.

2. Mineralogical analysis using The DTA/TGA and XRD demonstrated ettringite as a stable phase at Ca:Al ratios 3:1 and greater with a linear increase in ettringite content.

3. The simulated reaction with the stoichiometric quantities of the reactants, $(Ca(OH)_2$ and $Al_2(SO_4)_3 \cdot 18\,H_2O$, indicated ettringite as the stable phase in samples with Ca:Al ratios 3:1 and greater. The mean difference in the amount of ettringite between the thermodynamically and experimentally calculated ettringite was 4%. This clearly indicates that thermodynamic model can be used to make a reliable prediction without the need for calibration.

7.4   Recommendations

This dissertation has established the use of thermodynamic models to predict formation of pozzolanic products. The recommended steps are based on the modeling experience from Chapter's 4 to 6. They are as follows:

1. **Characterization:** Material characterization serves two purpose (1) To provide input data for the thermodynamic model from mineralogical analysis and (2) To validate the model results. This can be carried out using mineralogical and engineering analysis. A flowchart on recommended characterization methods for modeling is shown in Figure 7.1

2. **Modeling:** Several models are available to simulate geochemical reactions. As discussed earlier, the algorithms are based on either GEM or LMA approach (Section 1.4.1 and 1.4.2).

Sample collection (treated and untreated)

Engineering analysis

Mineralogical analysis

Method	Objective
Unconfined compressive strenght	Determine strength
pH	Measure alkalinity of the material
Plasticity Index	Measure expansion potential of the material
Swell test	Measure swell potential

Method	Objective
X-Ray diffraction (XRD)	Determine crystalline phases
Quantitative-XRD (Internal standard)	Quantify crystalline and amorphous phases
Thermogravimteric analysis	Supplement QXRD data by identifying pozzolanic products like CSH, CAH, and, ettringite
X-Ray fluorescence	Elemental composition

Figure 7.1: Recommended methods for material characterization

A simple flowchart to determine the appropriate thermodynamic model is shown in Figure 7.2.

Selecting the appropriate model depends on the objective. For example, to predict and quantify hydration products at equilibrium, GEM-Selektor coupled with the CEMDATA thermodynamic database is efficient and reliable. If the objective is to predict whether a certain hydration product will form in stabilized soil, qualitative models such as Geochemist's Workbench are more suitable. Therefore, the selection of model is dependent on the quantitative and qualitative prediction capabilities. Availability of thermodynamic data like Gibbs' energy minimization, solubility product, etc., may also dictate the choice of the selected model. In such cases, thermodynamic data from two or more databases can be combined. For example, The thermodynamic data for soil minerals and hydration products can be adopted MINES [165] and CEMDATA 7/4/18 [162], respectively. The data from the two databases can be combined to assemble a new database that can be used to model the reactions between a chemical stabilizer and soil mineral(s).
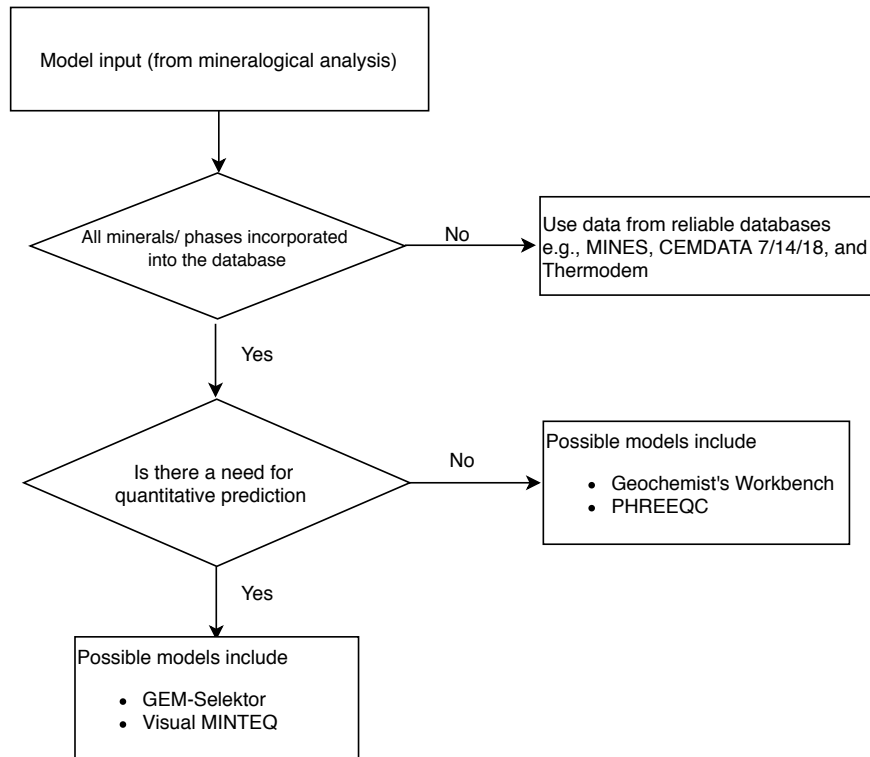
Figure 7.2: Recommended models for reaction simulation

3. **Validation:** It is important to evaluate the reliability of a model. Since the primary output of a thermodynamic model is to determine the stability of a mineral/ phase, mineralogical analysis can be used to validate the model. For example, a model developed to predict ettringite in sulfate rich soil treated with lime can be validated using TGA/DTA and XRD analysis.

7.5 Future research directions

This dissertation has established the efficacy of using thermodynamic models to predict favorable and deleterious reactions in chemically stabilized soils. However, there are several improvements that can be made to improve the reliability and applicability of the model. Some ideas and techniques are presented in the following paragraphs.

7.5.1 Soil reactivity

The reactivity of soil minerals is a key component in determining the reliability of a model. In this dissertation, the reactivity of soil minerals was studied qualitatively before and after reaction. For example, in Chapter 3, X-ray diffraction was used to study the dissolution of smectite treated with different concentrations of HIS. In addition, quantitative methods such as quantitative X-ray diffraction can be used to monitor the change in quantity of each soil mineral after chemical treatment. Experimentally calculated amounts of reacted soil minerals can be used as an model input to simulate the reaction between a chemical stabilizer and the soil mineral(s). For example, in a soil containing smectite, kaolinite and quartz, if we could experimentally calculate the amount of each soil mineral that has reacted after lime treatment, the reacted quantities of each mineral can be used as an input to the thermodynamic model to quantity pozzolanic products such as calcium-silicate-hydrate, calcium-aluminate-hydrate, ettringite, etc., at equilibrium.

Experimental data on reaction kinetics will also play a critical role in predicting sulfate induced. Chapter's 4 and 5 used thermodynamic models to predict ettringite at equilibrium which is a long term prediction. To simulate kinetics, mineralogical and pore solution data measured at different time periods is required. This can be determined experimentally by simulating the stabilization reaction in a reactor that monitors and records the time dependent dissolution of each soil mineral treated with the chemical stabilizer. The recorded data can then be used in the model to predict the short term reaction products.

7.5.2 Multimodel approach

The limitation of a thermodynamic model is its inability to relate geochemical changes to a engineering properties. A multimodel link connecting microscopic mineralogical changes with engineering properties like strength will be of significant use to civil engineers. For example, in chemically stabilized soils where sulfate attack is of concern, a multimodel approach will be useful in relating the percentage of predicted ettringite with the expected volumetric change. To achieve this, measurements of ettringite content and volumetric change must be recorded simultaneously. The recorded measurements can then be used to develop an empirical relations between the predicted ettringite content and volume change. Therefore, a multimodel approach will be useful in relating the predicted the predicted geochemical changes with the expected engineering behavior.

REFERENCES

[1] J. K. Jeyapalan, G. T. Rice, and R. L. Lytton, *State-of-the-art Review of Expansive Soil Treatment Methods*. Texas A & M University, 1981.

[2] F. H. Chen, *Foundations on expansive soils*, vol. 12. Elsevier, 2012.

[3] L. Ge, C.-C. Wang, C.-W. Hung, W.-C. Liao, and H. Zhao, "Assessment of strength development of slag cement stabilized kaolinite," *Construction and Building Materials*, vol. 184, pp. 492–501, 2018.

[4] X. Wang, Z. Pan, X. Shen, and W. Liu, "Stability and decomposition mechanism of ettringite in presence of ammonium sulfate solution," *Construction and Building Materials*, vol. 124, pp. 786–793, 2016.

[5] D. Little, B. Herbert, and S. Kunagalli, "Ettringite formation in lime-treated soils: Establishing thermodynamic foundations for engineering practice," *Transportation Research Record: Journal of the Transportation Research Board*, no. 1936, pp. 51–59, 2005.

[6] F. Winnefeld and B. Lothenbach, "Hydration of calcium sulfoaluminate cements-experimental findings and thermodynamic modelling," *Cement and Concrete Research*, vol. 40, no. 8, pp. 1239–1247, 2010.

[7] T. M. Petry and D. N. Little, "Update on sulfate-induced heave in treated clays; problematic sulfate levels," *Transportation research record*, pp. 51–51, 1992.

[8] A. J. Puppala, S. Hanchanloet, M. Jadeja, and B. Burkart, "Evaluation of sulfate induced heave by mineralogical and swell tests," in *Proc., 9th Pan-American Conf. on Soil Mechanics and Geotechnical Engineering*, 1999.

[9] P. Harris, J. Holdt, S. Sebesta, and T. Scullion, *Recommendations for stabilization of high-sulfate soils in Texas*. The Institute, 2005.

[10] J. K. Mitchell and D. Dermatas, "Clay soil heave caused by lime-sulfate reactions," in *Innovations and uses for lime*, ASTM International, 1992.

[11] A. J. Puppala, N. Intharasombat, and R. K. Vempati, "Experimental studies on ettringite-induced heaving in soils," *Journal of Geotechnical and Geoenvironmental Engineering*, vol. 131, no. 3, pp. 325–337, 2005.

[12] S. Nair and D. Little, "Water as the key to expansion of ettringite in cementitious materials," *Transportation Research Record: Journal of the Transportation Research Board*, no. 2104, pp. 55–62, 2009.

[13] A. Soive, E. Roziere, and A. Loukili, "Parametrical study of the cementitious materials degradation under external sulfate attack through numerical modeling," *Construction and Building Materials*, vol. 112, pp. 267–275, 2016.

[14] Q. Nie, C. Zhou, H. Li, X. Shu, H. Gong, and B. Huang, "Numerical simulation of fly ash concrete under sulfate attack," *Construction and Building Materials*, vol. 84, pp. 261–268, 2015.

[15] Q. Ding, J. Yang, D. Hou, and G. Zhang, "Insight on the mechanism of sulfate attacking on the cement paste with granulated blast furnace slag: An experimental and molecular dynamics study," *Construction and Building Materials*, vol. 169, pp. 601–611, 2018.

[16] W. R. Cannon, B. M. Pettitt, and J. A. McCammon, "Sulfate anion in water: model structural, thermodynamic, and dynamic properties," *The Journal of Physical Chemistry*, vol. 98, no. 24, pp. 6225–6230, 1994.

[17] G. Kidder, *Swelling characteristics of hydroxy-aluminum interlayered clays*. PhD thesis, Oklahoma State University, 1969.

[18] C. Pesquera, F. González, I. Benito, C. Blanco, S. Mendioroz, and J. Pajares, "Passivation of a montmorillonite by the silica created in acid activation," *Journal of Materials Chemistry*, vol. 2, no. 9, pp. 907–911, 1992.

[19] W. Xiang, D. Cui, Q. Liu, X. Lu, and L. Cao, "Theory and practice of ionic soil stabilizer reinforcing special clay," *Journal of Earth Science*, vol. 21, no. 6, pp. 882–887, 2010.

[20] Y.-m. Wang and X.-l. Liu, "Tests of ionic soil stabilizer reinforcing expansive soil," in *2011 Second International Conference on Mechanic Automation and Control Engineering*, pp. 2663–2666, IEEE, 2011.

[21] H. M. Alhassan and L. F. Olaniyi, "Effect of Ionic Soil Stabilizer 2500 on the properties of black cotton soil," *British Journal of Applied Science & Technology*, vol. 3, no. 3, p. 406, 2013.

[22] A. Soltani, A. Deng, A. Taheri, and M. Mirzababaei, "A sulphonated oil for stabilisation of expansive soils," *International Journal of Pavement Engineering*, vol. 20, no. 11, pp. 1285–1298, 2019.

[23] S. He, X. Yu, S. Gautam, and L. R. Hoyos, "Influence of ionic soil stabilizer (ISS) dosage on the stabilization effectiveness of expansive soils," in *IFCEE 2018*, pp. 103–112, 2018.

[24] S. He *et al.*, *Chemical Stabilization of Expansive Soils Using Liquid Ionic Soil Stabilizers (LISS)*. PhD thesis, 2019.

[25] R. Garrels and M. Thompson, "A chemical model for sea water at $25^{o}C$ and one atmosphere total pressure," *American Journal of Science*, vol. 260, no. 1, pp. 57–66, 1962.

[26] H. C. Helgeson, "Evaluation of irreversible reactions in geochemical processes involving minerals and aqueous solutions," *Geochimica et Cosmochimica Acta*, vol. 32, no. 8, pp. 853–877, 1968.

[27] C. M. Bethke, *Geochemical and biogeochemical reaction modeling*. Cambridge University Press, 2007.

[28] D. Kulik, U. Berner, and E. Curti, "Modelling chemical equilibrium partitioning with the gems-psi code," tech. rep., 2004.

[29] D. G. Schulze, "An introduction to soil mineralogy," *Soil mineralogy with environmental applications*, pp. 1–35, 2002.

[30] M. Khalid, R. Walvekar, M. R. Ketabchi, H. Siddiqui, and M. E. Hoque, "Rubber/nanoclay composites: Towards advanced functional materials," in *Nanoclay Reinforced Polymer Composites*, pp. 209–224, Springer, 2016.

[31] M. E. Essington, *Soil and water chemistry: an integrative approach*. CRC press, 2015.

[32] J. K. Mitchell, K. Soga, *et al.*, *Fundamentals of soil behavior*, vol. 3. John Wiley & Sons Hoboken, NJ, 2005.

[33] M. W. Witczak, "Relationships between physiographic units and highway design factors," *NCHRP Report*, no. 132, 1972.

[34] I. Barshad, "The effect of the interlayer cations on the expansion of the mica type of crystal lattice," *American Mineralogist: Journal of Earth and Planetary Materials*, vol. 35, no. 3-4, pp. 225–238, 1950.

[35] F. Allison, M. Kefauver, and E. Roller, "Ammonium fixation in soils," *Soil Science Society of America Journal*, vol. 17, no. 2, pp. 107–110, 1953.

[36] N. Hariharan, D. N. Little, J. R. Menendez, and H. Sahin, "Effect of hydrogen ion exchange chemical treatment on engineering properties of expansive subgrades in texas," Tech. Rep. 18-06501, 2018.

[37] R. Malek, "Effect of EcSS-3000^{TM} soil stabilizer on the strength of montmorillonite," pp. 17–18, 2008.

[38] D. K. Marquart, "Chemical stabilization of three texas vertisols with sulfonated naphthalene," Master's thesis, Texas A&M University, 1995.

[39] S. L. Sarkar, B. E. Herbert, and R. J. Scharlin, "Injection stabilization of expansive clays using a hydrogen ion exchange chemical," in *Advances in Unsaturated Geotechnics*, pp. 487–516, ASCE, 2000.

[40] S. A. Shaw and M. J. Hendry, "Geochemical and mineralogical impacts of H_2SO_4 on clays between pH 5.0 and -3.0," *Applied Geochemistry*, vol. 24, no. 2, pp. 333–345, 2009.

[41] S. A. Bagshaw and R. P. Cooney, "FTIR analysis of pillared clay pore structure via adsorbed bipyridine surface probe species," *Applied spectroscopy*, vol. 50, no. 10, pp. 1319–1324, 1996.

[42] A. Buswell, K. Krebs, and W. Rodebush, "Infrared studies.III. Absorption bands of hydrogels between 2.5 and 3.5 μ," *Journal of the American Chemical Society*, vol. 59, no. 12, pp. 2603–2605, 1937.

[43] H. Zhao, L. Ge, T. M. Petry, and Y.-Z. Sun, "Effects of chemical stabilizers on an expansive clay," *KSCE Journal of Civil Engineering*, vol. 18, pp. 1009–1017, May 2014.

[44] N. Shewring, T. Jones, G. Maitland, and J. Yarwood, "Fourier transform infrared spectroscopic techniques to investigate surface hydration processes on bentonite," *Journal of colloid and interface science*, vol. 176, no. 2, pp. 308–317, 1995.

[45] J. R. Sohn and J. T. Kim, "Infrared study of alkyl ketones adsorbed on the interlamellar surface of montmorillonite," *Langmuir*, vol. 16, no. 12, pp. 5430–5434, 2000.

[46] J. R. Sohn and S. I. Lee, "Adsorption study of acetylacetone on cation-exchanged montmorillonite by infrared spectroscopy," *Langmuir*, vol. 16, no. 11, pp. 5024–5028, 2000.

[47] D. N. Little, F. Yusuf, *et al.*, "An example problem illustrating the application of the national lime association mixture design and testing protocol (MDTP) to ascertain engineering properties of lime-treated subgrades for mechanistic pavement design/analysis.," tech. rep., Texas Transportation Institute, 2001.

[48] T. M. Petry and D. N. Little, "Review of stabilization of clays and expansive soils in pavements and lightly loaded structures—history, practice, and future," *Journal of materials in civil engineering*, vol. 14, no. 6, pp. 447–460, 2002.

[49] D. N. Little, *Evaluation of structural properties of lime stabilized soils and aggregates*. National Lime Association, 1998.

[50] D. N. Little, *Stabilization of pavement subgrades and base courses with lime*. 1995.

[51] Y. Jiang, B. Killingsworth, M. Darter, H. Von Quintus, and E. Owusu-Antwi, "Systems for design of highway pavements: Catalog of current state pavement design features, final report for NCHRP Project 1-32," tech. rep., 1997.

[52] ACPA, "Database of state DOT Concrete Pavement Practices."

[53] L. E. Katz, A. F. Rauch, H. M. Liljestrand, J. S. Harmon, K. S. Shaw, and H. Albers, "Mechanisms of soil stabilization with liquid ionic stabilizer," *Transportation Research Record*, vol. 1757, no. 1, pp. 50–57, 2001.

[54] D. Cui, W. Xiang, and Q. Chen, "Experimental study on ionic soil stabilizer keeping the hole diameter of clay stratum in HDD," in *ICPTT 2011: Sustainable Solutions For Water, Sewer, Gas, And Oil Pipelines*, pp. 725–732, 2011.

[55] S. D.E, "Non-standard stabilizers," 1992.

[56] J. S. Tingle, J. K. Newman, S. L. Larson, C. A. Weiss, and J. F. Rushing, "Stabilization mechanisms of nontraditional additives," *Transportation research record*, vol. 1989, no. 1, pp. 59–67, 2007.

[57] A. F. Rauch, J. S. Harmon, L. E. Katz, and H. M. Liljestrand, "Measured effects of liquid soil stabilizers on engineering properties of clay," *Transportation Research Record*, vol. 1787, no. 1, pp. 33–41, 2002.

[58] P. Akula and D. N. Little, "Thermodynamic stability of smectite treated with chemical stabilizer," in *Advances in Materials and Pavement Prediction*, pp. 507–510, CRC Press, 2018.

[59] J. K. Mitchell, "Practical problems from surprising soil behaviour," *J. of Geotech. Engrg.*, vol. 112, no. 3, pp. 259–289, 1986.

[60] D. Hunter, "Lime-induced heave in sulfate-bearing clay soils," *Journal of geotechnical engineering*, vol. 114, no. 2, pp. 150–167, 1988.

[61] D. Little and D. N. Little, "Update on sulfate-induced heave in treated clays; problematic sulfate levels," *Transportation Research Record*, no. 1362, 1992.

[62] T. M. Petry, "Investigation, analyses and recommendation for resolution of sulfate induced heave on SH-161 in Irving, Texas," *Texas Transportation Institute Research Study*, pp. 7– 1994, 1994.

[63] D. Little, "Evaluation of mechanisms of pavement distress on us highway 287 by-pass, berthoud, colorado," *Report prepared for Colorado Department of Transportation*, 2005.

[64] Tx-DOT, "Guidelines for treatment of sulfate-rich soils and bases in pavement structures," tech. rep., 2005.

[65] TxDOT, "TEX-145-E: Determining sulfate content in soils — colorimteric method," tech. rep., 2005.

[66] "Standard method of test for determining water-soluble sulfate ion content in soil," standard, AASHTO, 1995.

[67] A. J. Puppala, C. Viyanant, A. P. Kruzic, and L. Perrin, "Evaluation of a modified soluble sulfate determination method for fine-grained cohesive soils," *Geotechnical Testing Journal*, vol. 25, no. 1, pp. 85–94, 2002.

[68] C. Warren and E. Reardon, "The solubility of ettringite at 25 c," *Cement and Concrete Research*, vol. 24, no. 8, pp. 1515–1524, 1994.

[69] R. B. Perkins and C. D. Palmer, "Solubility of ettringite $Ca_6[Al(OH)_5]_2(SO_4)_3 \cdot 26\,H_2O$ at 5-75 ^oC," *Geochimica et Cosmochimica Acta*, vol. 63, no. 13-14, pp. 1969–1980, 1999.

[70] S. C. Myneni, S. J. Traina, and T. J. Logan, "Ettringite solubility and geochemistry of the $Ca(OH)_2$-$Al_2(SO_4)_3 \cdot H_2O$ system at 1 atm pressure and 298 K," *Chemical Geology*, vol. 148, no. 1-2, pp. 1–19, 1998.

[71] A. Moore and H. Taylor, "Crystal structure of ettringite," *Acta Crystallographica Section B*, vol. 26, no. 4, pp. 386–393, 1970.

[72] "Geochemistry of trace elements in alkaline systems." `http://https://geoweb.princeton.edu/research/geochemistry/research/surfaces-ettringite.html`. Accessed: 2020-01-07.

[73] A. Cody, H. Lee, R. Cody, and P. Spry, "The effects of chemical environment on the nucleation, growth, and stability of ettringite $[Ca_3Al(OH)_6]_2(SO_4)_3 \cdot 26\,H_2O$," *Cement and Concrete Research*, vol. 34, no. 5, pp. 869–881, 2004.

[74] S. K. K. S. Nair, *Sulfate induced heave: Addressing ettringite behavior in lime treated soils and in cementitious materials*. Texas A&M University, 2010.

[75] T. Matschei, B. Lothenbach, and F. P. Glasser, "Thermodynamic properties of portland cement hydrates in the system cao–al2o3–sio2–caso4–caco3–h2o," *Cement and Concrete Research*, vol. 37, no. 10, pp. 1379–1410, 2007.

[76] K. De Weerdt, M. B. Haha, G. Le Saout, K. O. Kjellsen, H. Justnes, and B. Lothenbach, "Hydration mechanisms of ternary portland cements containing limestone powder and fly ash," *Cement and Concrete Research*, vol. 41, no. 3, pp. 279–291, 2011.

[77] P. Akula and D. N. Little, "Coupled thermodynamic and experimental approach to evaluate ettringite formation in a soil stabilized with fluidized bed ash by-product: A case study," *Transportation Geotechnics*, p. 100352, 2020.

[78] L. J. Parrott, M. Geiker, W. A. Gutteridge, and D. Killoh, "Monitoring portland cement hydration: comparison of methods," *Cement and concrete research*, vol. 20, no. 6, pp. 919–926, 1990.

[79] K. N. Sachin, *An integrated approach to predict ettringite formation in sulfate soils and identifying sulfate damage along SH 130*. PhD thesis, Texas A&M University, 2005.

[80] R. Dudal and H. Eswaran, "Distribution, properties and classification of vertisols," *Vertisols: Their distribution, properties, classification and management*, pp. 1–22, 1988.

[81] D. Texas, "Guidelines for modification and stabilization of soils and base for the use in pavement structure," *TxDOT Construction Department*, 2005.

[82] A. Pavan and T. Tamilmani, "Numerical analysis on the effect of jet grout piles on an excavation located in an urban area," *Int. J. of GEOMATE*, vol. 8, no. 1, pp. 1167–1171, 2015.

[83] T. Petry and B. Das, "Evaluation of chemical modifiers and stabilizers for chemically active soils—clays," *Transportation Research Record: Journal of the Transportation Research Board*, no. 1757, pp. 43–49, 2001.

[84] F. Bergaya and G. Lagaly, "Surface modification of clay minerals," *Applied clay science*, vol. 1, no. 19, pp. 1–3, 2001.

[85] K. A. Carrado and P. Komadel, "Acid activation of bentonites and polymer-clay nanocomposites," *Elements*, vol. 5, no. 2, pp. 111–116, 2009.

[86] A. Amari, M. Chlendi, A. Gannouni, and A. Bellagi, "Optimised activation of bentonite for toluene adsorption," *Applied Clay Science*, vol. 47, no. 3-4, pp. 457–461, 2010.

[87] Z. P. Tomić, S. B. Antić-Mladenović, B. M. Babić, V. A. Poharc-Logar, A. R. Đorđević, and S. B. Cupać, "Modification of smectite structure by sulfuric acid and characteristics of the modified smectite," *Journal of Agricultural Sciences*, vol. 56, no. 1, pp. 25–35, 2011.

[88] S. Morodome and K. Kawamura, "Swelling behavior of Na-and Ca-montmorillonite up to $150^{o}C$ by in situ X-ray diffraction experiments," *Clays and Clay Minerals*, vol. 57, no. 2, pp. 150–160, 2009.

[89] P. M. Amarasinghe, K. S. Katti, and D. R. Katti, "Nature of organic fluid–montmorillonite interactions: An FTIR spectroscopic study," *Journal of Colloid and Interface Science*, vol. 337, no. 1, pp. 97–105, 2009.

[90] J. Gustafsson, "Visual minteq ver.3.0." http://www2.lwr.kth.se/English/OurSoftware/vminteq/index.html, 2010.

[91] C. Bethke, *The geochemist's workbench release 4.0: a user's guide to Rxn, Act2, Tact, React, and Gtplot*, vol. 224. 2002.

[92] C. M. Bethke, *Geochemical and biogeochemical reaction modeling*. Cambridge University Press, 2007.

[93] D. A. Kulik, T. Wagner, S. V. Dmytrieva, G. Kosakowski, F. F. Hingerl, K. V. Chudnenko, and U. R. Berner, "GEM-Selektor geochemical modeling package: revised algorithm and GEMS3K numerical kernel for coupled simulation codes," *Computational Geosciences*, vol. 17, no. 1, pp. 1–24, 2013.

[94] W. B. White, S. M. Johnson, and G. B. Dantzig, "Chemical equilibrium in complex mixtures," *The Journal of Chemical Physics*, vol. 28, no. 5, pp. 751–755, 1958.

[95] MTI Bio-Ag, 2870 Forbs Avenue Hoffman Es tates, IL 60192, *Technical Data Sheet: Volcay90*, Jan 2013.

[96] A. ASTM E104-02, "E104-02 (2012),"," *Standard Practice for Maintaining Constant Relative Humidity by Means of Aqueous Solutions*, pp. 1417–1421.

[97] ASTM-D698, *Standard Test Methods for Laboratory Compaction Characteristics of Soil Using Standard Effort (12400 ft-lbf/ft^3 (600 KN-m/m^3))*. ASTM international, 2007.

[98] Z. P. Tomić, V. P. Logar, B. M. Babic, J. R. Rogan, and P. Makreski, "Comparison of structural, textural and thermal characteristics of pure and acid treated bentonites from aleksinac and petrovac (Serbia)," *Spectrochimica Acta Part A: Molecular and Biomolecular Spectroscopy*, vol. 82, no. 1, pp. 389–395, 2011.

[99] A. De Cristofaro and A. Violante, "Effect of hydroxy-aluminium species on the sorption and interlayering of albumin onto montmorillonite," *Applied Clay Science*, vol. 19, no. 1-6, pp. 59–67, 2001.

[100] A. Steudel, L. Batenburg, H. Fischer, P. Weidler, and K. Emmerich, "Alteration of swelling clay minerals by acid activation," *Applied Clay Science*, vol. 44, no. 1-2, pp. 105–115, 2009.

[101] S. Gražulis, D. Chateigner, R. T. Downs, A. Yokochi, M. Quirós, L. Lutterotti, E. Manakova, J. Butkus, P. Moeck, and A. Le Bail, "Crystallography open database–an open-access collec-

tion of crystal structures," *Journal of Applied Crystallography*, vol. 42, no. 4, pp. 726–729, 2009.

[102] A. Clearfield, J. H. Reibenspies, and N. Bhuvanesh, *Principles and applications of powder diffraction*. John Wiley and Sons, Ltd., 2008.

[103] P. Komadel, "Acid activated clays: Materials in continuous demand," *Applied Clay Science*, vol. 131, pp. 84–99, 2016.

[104] K. Bukka, J. Miller, and J. Shabtai, "FTIR study of deuterated montmorillonites: Structural features relevant to pillared clay stability," *Clays and Clay Minerals*, vol. 40, no. 1, pp. 92–102, 1992.

[105] H. W. Van der Marel, H. Beutelspacher, *et al.*, *Atlas of infrared spectroscopy of clay minerals and their admixtures*. Elsevier Publishing Company., 1976.

[106] H. Bahadori, A. Hasheminezhad, and F. Taghizadeh, "Experimental study on marl soil stabilization using natural pozzolans," *Journal of Materials in Civil Engineering*, vol. 31, no. 2, p. 04018363, 2018.

[107] D. Wang, J. Zhu, and F. He, "CO_2 carbonation-induced improvement in strength and microstructure of reactive MgO-CaO-fly ash solidified soils," *Construction and Building Materials*, vol. 229, p. 116914, 2019.

[108] Y. Kim, T. Q. Tran, G. Kang, and T. M. Do, "Stabilization of a residual granitic soil using various new green binders," *Construction and Building Materials*, vol. 223, pp. 724–735, 2019.

[109] P. Sudla, J. Donrak, M. Hoy, S. Horpibulsuk, A. Arulrajah, A. S. A. Rashid, R. Nazir, and W. Samingthong, "Laboratory investigation of cement-stabilized marginal lateritic soil by crushed slag–fly ash replacement for pavement applications," *Journal of Materials in Civil Engineering*, vol. 32, no. 2, p. 04019353, 2019.

[110] P. Sukmak, P. De Silva, S. Horpibulsuk, and P. Chindaprasirt, "Sulfate resistance of clay-portland cement and clay high-calcium fly ash geopolymer," *Journal of Materials in Civil Engineering*, vol. 27, no. 5, p. 04014158, 2014.

[111] A. Arulrajah, T. Kua, C. Phetchuay, S. Horpibulsuk, F. Mahghoolpilehrood, and M. M. Disfani, "Spent coffee grounds–fly ash geopolymer used as an embankment structural fill material," *Journal of Materials in Civil Engineering*, vol. 28, no. 5, p. 04015197, 2015.

[112] A. Mohammadinia, A. Arulrajah, J. Sanjayan, M. M. Disfani, M. W. Bo, and S. Darmawan, "Strength development and microfabric structure of construction and demolition aggregates stabilized with fly ash–based geopolymers," *Journal of Materials in Civil Engineering*, vol. 28, no. 11, p. 04016141, 2016.

[113] K. Gu and B. Chen, "Loess stabilization using cement, waste phosphogypsum, fly ash and quicklime for self-compacting rammed earth construction," *Construction and Building Materials*, vol. 231, p. 117195, 2020.

[114] Y. Liu, C. Chang, A. Namdar, Y. She, C.-H. Lin, X. Yuan, and Q. Yang, "Stabilization of expansive soil using cementing material from rice husk ash and calcium carbide residue," *Construction and Building Materials*, vol. 221, pp. 1–11, 2019.

[115] R. Fernández, A. I. Ruiz, and J. Cuevas, "Formation of CASH phases from the interaction between concrete or cement and bentonite," *Clay Minerals*, vol. 51, no. 2, pp. 223–235, 2016.

[116] M. Ahmaruzzaman, "A review on the utilization of fly ash," *Progress in energy and combustion science*, vol. 36, no. 3, pp. 327–363, 2010.

[117] R. Siddique and M. I. Khan, *Supplementary cementing materials*. Springer Science & Business Media, 2011.

[118] T. M. Petry, *Studies of factors causing and influencing localized heave of lime treated clay soils (sulfate induced heave)*. University of Texas at Arlington, Civil Engineering Department, 1994.

[119] P. Harris, T. Scullion, S. Sebesta, and G. Claras, "Measuring sulfate in subgrade soil: Difficulties and triumphs," *Transportation Research Record: Journal of the Transportation Research Board*, no. 1837, pp. 3–11, 2003.

[120] A. J. Puppala and A. Cerato, "Heave distress problems in chemically-treated sulfate-laden materials," *Geo-Strata—Geo Institute of ASCE*, vol. 10, no. 2, p. 28, 2009.

[121] A. J. Puppala, N. Talluri, S. S. C. Congress, and A. Gaily, "Ettringite induced heaving in stabilized high sulfate soils," *Innovative Infrastructure Solutions*, vol. 3, no. 1, p. 72, 2018.

[122] M. Collepardi, "Thaumasite formation and deterioration in historic buildings," *Cement and Concrete Composites*, vol. 21, no. 2, pp. 147–154, 1999.

[123] A. Schöler, B. Lothenbach, F. Winnefeld, and M. Zajac, "Hydration of quaternary portland cement blends containing blast-furnace slag, siliceous fly ash and limestone powder," *Cement and Concrete Composites*, vol. 55, pp. 374–382, 2015.

[124] B. Lothenbach and F. Winnefeld, "Thermodynamic modelling of the hydration of portland cement," *Cement and Concrete Research*, vol. 36, no. 2, pp. 209–226, 2006.

[125] Y. Elakneswaran, E. Owaki, S. Miyahara, M. Ogino, T. Maruya, and T. Nawa, "Hydration study of slag-blended cement based on thermodynamic considerations," *Construction and Building Materials*, vol. 124, pp. 615–625, 2016.

[126] B. Lothenbach, B. Bary, P. Le Bescop, T. Schmidt, and N. Leterrier, "Sulfate ingress in portland cement," *Cement and Concrete Research*, vol. 40, no. 8, pp. 1211–1225, 2010.

[127] B. Lothenbach, T. Matschei, G. Möschner, and F. P. Glasser, "Thermodynamic modelling of the effect of temperature on the hydration and porosity of portland cement," *Cement and Concrete Research*, vol. 38, no. 1, pp. 1–18, 2008.

[128] T. Wagner, D. A. Kulik, F. F. Hingerl, and S. V. Dmytrieva, "GEM-Selektor geochemical modeling package: TSolMod library and data interface for multicomponent phase models," *The Canadian Mineralogist*, vol. 50, no. 5, pp. 1173–1195, 2012.

[129] available at `http://gems.web.psi.ch`.

[130] D. K. KT. Thoenen, "Nagra/PSI chemical thermodynamic database 01/01 for GEMS-Selektor (V.2-PSI) geochemical modelling code," *PSI Villingen*, 2003.

[131] W. Hummel, U. Berner, E. Curti, F. Pearson, and T. Thoenen, "Nagra technical report NTB 02-16," *Nagra, Wettingen, Switzerland and Universal Publishers/uPublish. com, Parkland, Florida*, 2002.

[132] B. Lothenbach, L. Pelletier-Chaignat, and F. Winnefeld, "Stability in the system CaO-Al_2O_3-H_2O," *Cement and concrete research*, vol. 42, no. 12, pp. 1621–1634, 2012.

[133] C. A. J. Appelo and D. Postma, *Geochemistry, groundwater and pollution*. CRC press, 2004.

[134] ASTM-D, "1452-09. Standard practice for soil investigation and sampling by auger borings,," *Annual Book of ASTM Standards, Part*, vol. 4.

[135] ASTM-D, "1883-14. "Standard test method for California Bearing Ratio (CBR) of laboratory-compacted soils"," 2014.

[136] ASTM-D, "4318-10. "Standard test methods for liquid limit, plastic limit, and plasticity index of soils".," *Annual book of ASTM standards, ASTM international, Philadelphia*, 2012.

[137] ASTM-D, "698-00a,(2002). "Standard test methods for laboratory compaction characteristics of soil using standard effort"," *Annual book of ASTM Standards*, vol. 4, pp. 78–88.

[138] ASTM-D, "6913-04, 2009. "Standard test methods for particle-size distribution (gradation) of soils using sieve analysis"," *American society for testing and materials*.

[139] A. Karathanasis and B. Hajek, "Elemental analysis by X-ray fluorescence spectroscopy," *Methods of Soil Analysis Part 3—Chemical Methods*, no. methodsofsoilan3, pp. 161–223, 1996.

[140] L. Whittig, W. Allardice, *et al.*, "X-ray diffraction techniques.," *Methods of soil analysis. Part 1. Physical and mineralogical methods*, pp. 331–362, 1986.

[141] W. Holtz, "Volume change in expansive clay soils and control by lime treatment," in *Proc., 2nd Int. Research and Engineering Conf. on Expansive Clay Soils*, pp. 157–174, Texas A&M University Press, 1969.

[142] J. Mallela, H. V. Quintus, and K. L. Smith, "Consideration of lime-stabilized layers in mechanistic-empirical pavement design," *The National Lime Association*, vol. 200, 2004.

[143] M.-H. Zhang and J. Islam, "Use of nano-silica to reduce setting time and increase early strength of concretes with high volumes of fly ash or slag," *Construction and Building Materials*, vol. 29, pp. 573–580, 2012.

[144] D. Little and R. Graves, "Guidelines for use of lime in sulfate bearing soils," *Unpublished report*, 1995.

[145] L. Wei, J. Xiao-Guang, and Z. Zhong-Ya, "Triaxial test on concrete material containing accelerators under physical sulphate attack," *Construction and Building Materials*, vol. 206, pp. 641–654, 2019.

[146] H. Min, L. Sui, F. Xing, H. Tian, and Y. Zhou, "An effective transport model of sulfate attack in concrete," *Construction and Building Materials*, vol. 216, pp. 365–378, 2019.

[147] L. Guo, Y. Wu, P. Duan, and Z. Zhang, "Improving sulfate attack resistance of concrete by using calcined Mg-Al-CO$_3$ LDH's: Adsorption behavior and mechanism," *Construction and Building Materials*, vol. 232, p. 117256, 2020.

[148] P. Hou, Z. Guo, Q. Li, X. Zhang, J. Liu, S. Yang, X. Cheng, R. Kumar, B. Srinivasaraonaik, and L. Singh, "Comparison study on the sulfate attack resistivity of cement-based materials modified with nanoSiO$_2$ and normal SCMs: Pore structure and phase composition," *Construction and Building Materials*, vol. 228, p. 116764, 2019.

[149] D. Dermatas, "Ettringite-induced swelling in soils: State-of-the-art," 1995.

[150] D. H. Moon, D. Dermatas, M. Wazne, A. M. Sanchez, M. Chrysochoou, and D. G. Grubb, "Swelling related to ettringite crystal formation in chromite ore processing residue," *Environmental geochemistry and health*, vol. 29, no. 4, pp. 289–294, 2007.

[151] L. G. Baquerizo, T. Matschei, and K. L. Scrivener, "Impact of water activity on the stability of ettringite," *Cement and Concrete Research*, vol. 79, pp. 31–44, 2016.

[152] Q. Zhou and F. P. Glasser, "Thermal stability and decomposition mechanisms of ettringite at < 120°C," *Cement and Concrete Research*, vol. 31, no. 9, pp. 1333–1339, 2001.

[153] T. Terai, A. Mikuni, Y. Nakamura, and K. Ikeda, "Synthesis of ettringite from portlandite suspensions at various ca/al ratios," *Inorganic Materials*, vol. 43, no. 7, pp. 786–792, 2007.

[154] F. Goetz-Neunhoeffer, J. Neubauer, and P. Schwesig, "Mineralogical characteristics of ettringites synthesized from solutions and suspensions," *Cement and concrete research*, vol. 36, no. 1, pp. 65–70, 2006.

[155] Q. Zhang and F. Saito, "Sonochemical synthesis of ettringite from a powder mixture suspended in water," *Powder technology*, vol. 107, no. 1-2, pp. 43–47, 2000.

[156] C. Bethke, *The Geochemist's Workbench: A Users Guide to Rxn, Act2, Tact, React, and Gtplot*. C. Bethke, 1992.

[157] B. Lothenbach and E. Wieland, "A thermodynamic approach to the hydration of sulphate-resisting portland cement," *Waste Management*, vol. 26, no. 7, pp. 706–719, 2006.

[158] P. Akula, D. Little, and P. Schwab, "Thermodynamic evaluation of smectite treated with hydrogen ion stabilizer," *Journal of Materials in Civil Engineering*, vol. 32, no. 5, p. 04020098, 2020.

[159] K. Scrivener, R. Snellings, and B. Lothenbach, *A practical guide to microstructural analysis of cementitious materials*. Crc Press, 2018.

[160] C. R. Hubbard, E. Evans, and D. Smith, "The reference intensity ratio, i/ic, for computer simulated powder patterns," *Journal of Applied Crystallography*, vol. 9, no. 2, pp. 169–174, 1976.

[161] Putz and Brandenburg, "Match! - phase identification from powder diffraction, crystal impact." `https://www.crystalimpact.de/match/`, 2019.

[162] "Cemdata 14: Empa (2014)." available at `http://www.empa.ch/cemdata`.

[163] J. Bensted and S. P. Varma, "Studies of ettringite and its derivatives," *Cement Technology*, vol. 2, no. 3, pp. 73–76, 1971.

[164] R. B. Myneni, F. G. Hall, P. J. Sellers, and A. L. Marshak, "The interpretation of spectral vegetation indexes," *IEEE Transactions on Geoscience and Remote Sensing*, vol. 33, no. 2, pp. 481–486, 1995.

[165] A. Gysi, "The mines thermodynamic database for simulating the chemistry of complex crustal fluid-rock systems," in *Goldschmidt Conference*, 2017.